Springer Theses
Recognizing Outstanding Ph.D. Research

Kazuma Nagao

Fluctuations and Non-Equilibrium Phenomena in Strongly-Correlated Ultracold Atoms

Springer

Springer Theses

Recognizing Outstanding Ph.D. Research

Aims and Scope

The series "Springer Theses" brings together a selection of the very best Ph.D. theses from around the world and across the physical sciences. Nominated and endorsed by two recognized specialists, each published volume has been selected for its scientific excellence and the high impact of its contents for the pertinent field of research. For greater accessibility to non-specialists, the published versions include an extended introduction, as well as a foreword by the student's supervisor explaining the special relevance of the work for the field. As a whole, the series will provide a valuable resource both for newcomers to the research fields described, and for other scientists seeking detailed background information on special questions. Finally, it provides an accredited documentation of the valuable contributions made by today's younger generation of scientists.

Theses are accepted into the series by invited nomination only and must fulfill all of the following criteria

- They must be written in good English.
- The topic should fall within the confines of Chemistry, Physics, Earth Sciences, Engineering and related interdisciplinary fields such as Materials, Nanoscience, Chemical Engineering, Complex Systems and Biophysics.
- The work reported in the thesis must represent a significant scientific advance.
- If the thesis includes previously published material, permission to reproduce this must be gained from the respective copyright holder.
- They must have been examined and passed during the 12 months prior to nomination.
- Each thesis should include a foreword by the supervisor outlining the significance of its content.
- The theses should have a clearly defined structure including an introduction accessible to scientists not expert in that particular field.

More information about this series at http://www.springer.com/series/8790

Kazuma Nagao

Fluctuations and Non-Equilibrium Phenomena in Strongly-Correlated Ultracold Atoms

Doctoral Thesis accepted by
Kyoto University, Sakyo-ku, Kyoto

Springer

Author
Dr. Kazuma Nagao
Institute for Laser Physics and Center for Optical Quantum Technologies
University of Hamburg
Hamburg, Germany

Supervisors
Prof. Keisuke Totsuka
Yukawa Institute for Theoretical Physics
Kyoto University
Sakyo-ku, Kyoto, Japan

Prof. Ippei Danshita
Department of Physics
Kindai University
Osaka, Japan

ISSN 2190-5053 ISSN 2190-5061 (electronic)
Springer Theses
ISBN 978-981-15-7170-1 ISBN 978-981-15-7171-8 (eBook)
https://doi.org/10.1007/978-981-15-7171-8

This Springer imprint is published by the registered company Springer Nature Singapore Pte Ltd.
The registered company address is: 152 Beach Road, #21-01/04 Gateway East, Singapore 189721, Singapore

To my parents.

Supervisor's Foreword I

High controllability and cleanness of ultracold gases pave a way to experimentally observing many interesting condensed-matter phenomena which are hard to observe in other (say, solid-state) settings. One possible application, whose original idea may be traced back to the Feynman's proposal in 1982, is to take this advantage of cold-gas systems to simulate quantum many-body systems with well-controlled experimental systems instead of using classical computers which are suffering from various problems. Armed with state-of-the-art read-out techniques such as quantum-gas microscope, this idea of using cold gases as "quantum simulators" for strongly-correlated many-body systems, which are hard to tackle with traditional theoretical approaches, has been successfully applied to various equilibrium phenomena, e.g., superfluid-insulator transitions in correlated Bose systems, antiferromagnetism in the two-dimensional Hubbard model, etc. On the other hand, quantum simulation of out-of-equilibrium problems is far less developed mainly due to the lack of precise and reliable theoretical results to compare with experiments. In this Thesis, Dr. Kazuma Nagao tries to fill the gap between theory and experiments in quantum simulation of quantum dynamics.

Among many challenging problems in this research area, Kazuma addresses two important questions in his Thesis. The first is related to table-top simulation of the Higgs (amplitude) mode with ultra-cold bosons in an optical lattice. Recent theoretical studies showed that quantum/thermal fluctuations and the existence of non-uniform trap potentials obscure the Higgs mode in two dimensions, thereby hindering the observation of the sharp peak in experiments. To explore the possibility of observing clear experimental signatures of the Higgs mode in higher dimensions, Kazuma investigates in Chap. 4 a particular response function of a three-dimensional Bose system to obtain positive answers that the Higgs mode survives fluctuations and can be seen in experiments even in the presence of inhomogeneity as far as we carefully perturb the system. I believe that these observations will motivate further "Higgs hunting" experiments in higher-dimensional Bose systems in the near future.

The second project is to develop a reliable theoretical tool that can be used to simulate non-equilibrium phenomena in higher-dimensional correlated many-body systems. Except for one-dimensional systems in which the time-dependent density-matrix renormalization group method is applicable, there are only a limited number of numerical tools available to reliably simulate far-from-equilibrium dynamics, such as quantum quenches, of quantum many-body systems to the extent that we can directly compare the data with experiments. To tackle this problem, Kazuma chose the semi-classical phase-space method called the Truncated Wigner Approximation (TWA). The essence of the TWA, roughly speaking, is to replace the complicated quantum-mechanical average of operators with that over classical trajectories in the phase space. He spent some time in learning this relatively new method from the scratch and visited the laboratory of professor Polkovnikov several times to polish his skills and extend the method to fermions in the strongly-correlated regime (unfortunately, the outcome of this interesting project is not included in this Thesis). His effort results in a concise but very pedagogical introduction to the method given in Chap. 3, which, together with a quick summary of ultra-cold Bose gases in Chap. 2, is definitely very useful to those who are interested in non-equilibrium phenomena in cold gases. The crowning Chap. 5 is the highlight of this Thesis, in which Kazuma tries to demonstrate the utility of the TWA approach in far-from-equilibrium dynamics. Specifically, he extends the TWA to investigate various dynamical phenomena subsequent to a quantum quench in two- and three-dimensional Bose-Hubbard systems, and finds a good agreement with the experimental data. Although we need further benchmark tests in order to establish the TWA method as the standard tool, his results, I believe, strongly suggest that the TWA is a promising method in far-from-equilibrium problems and will contribute significantly to the development of quantum simulation of non-equilibrium phenomena.

Kyoto, Japan
March 2020

Prof. Keisuke Totsuka

Supervisor's Foreword II

Recent years have witnessed a rapid growth in studies of quantum many-body physics thanks to technological advances in building and utilizing synthetic quantum platforms, such as superconducting circuits, quantum dots, trapped ions, Rydberg atoms trapped in an optical tweezer array, and ultracold gases in optical lattices. Among those platforms, a system of an optical lattice loaded with an ultracold gas especially has a long successful history in the application for analog quantum simulations. Since the first observation of the superfluid-to-Mott insulator transition of a Bose gas in an optical lattice in 2002, optical-lattice quantum simulators have been applied for studying various kinds of quantum many-body physics so that they now attract much attention from a broad range of subfields of physics, including not only atomic, molecular, and optical physics, and condensed matter physics, but also nuclear and high-energy physics.

A drawback of such a rapidly growing topic with a long history is that hurdles for novice researchers are now rather high because the accumulated knowledge and the available toolbox are diverse, and the state-of-the art research has become more and more complicated. This thesis written by Dr. Kazuma Nagao certainly serves as a useful textbook for such novices to learn basics of quantum many-body physics of the optical-lattice systems. The high readability of this thesis can be attributed partly to the fact that it focuses on a single-component Bose gas in an optical lattice, which serves as a quantum simulator of the single-component Bose-Hubbard model and is one of the simplest settings in various quantum simulators realizable with optical lattices. A remarkable advantage of the Bose-Hubbard model is that many of its important features in and near equilibrium, such as quantum phase transitions, thermodynamics, and elementary excitations, can be captured through analytical calculations at least qualitatively. In Chap. 2, Dr. Nagao carefully reviews those analytical calculations with several different approaches so that the readers can acquire deep insights into the system and proficiency in field-theoretical methods. In Chap. 4, he further develops the analytical approaches by combining the local density approximation with three standard field theoretical techniques, namely the Schwinger boson representation, the Holstein-Primakov expansion, and the finite-temperature Green's function techniques. He predicts that the Higgs

amplitude mode of Bose gases in a three-dimensional optical lattice can be detected as a resonance peak at accessible finite temperatures in the presence of a trapping potential, demonstrating that the basics of the quantum many-body theory presented in Chap. 2 are still very useful in the front-line research topic.

Another unique feature of this thesis is that Chap. 5 constitutes an exemplary case of how theoretical researchers can use optical-lattice quantum simulators. During his Ph.D. student period, Dr. Nagao engaged as a theoretical research assistant in a project regarding development of optical-lattice quantum simulators built by the Quantum Optics Group at Kyoto University. In a specific theme of the project, the experimental group performed a quantum simulation of non-equilibrium dynamics of the three-dimensional Bose-Hubbard model after a sudden quench of the optical-lattice depth starting with a Mott insulating state to a deep superfluid region. They measured the time evolution of the kinetic and interaction energies. Since this high-dimensional system consisted roughly of ten thousand particles, it was obviously infeasible for classical computers to simulate the system in a numerically exact manner. Nevertheless, the accuracy of outputs from the quantum simulator was ensured via thorough comparisons with exact numerical computations in 1D. Hence, Dr. Nagao decided to utilize the quantum simulation results as a quantitative reference for examining the performance of some approximate numerical methods. In Chap. 5, he specifically chose the truncated Wigner approximation based on the Gross-Pitaevskii equation, whose pedagogical review is presented in Chap. 3, in order to substantiate its quantitative validity on the quench dynamics. He further applied the method with "a stamp of approval" by the quantum simulator to the problem of spatial spreading of a two-point correlation function and presented discussions from a viewpoint of quasi-particle propagations. This type of usage of optical-lattice quantum simulators is rather natural for and highly demanded by theoretical researchers, for whom the contents in Chap. 5 will be a simple textbook example.

Higashi-Osaka, Japan
May 2020

Prof. Ippei Danshita

Preface

This Thesis studies fluctuation effects on non-equilibrium quantum many-body phenomena in ultracold atoms trapped by an optical lattice. The remarkable controllability and cleanness of the optical-lattice system have allowed us to regard it as an *analog quantum simulator* to experimentally simulate quantum many-body systems encountered in condensed-matter physics both in and out of equilibrium. One of the most prominent advances in the research field is the quantum-gas microscope approach to hunting the Higgs mode in a strongly-correlated superfluid gas trapped by an optical lattice. The experimental technologies including this cutting-edge microscopy have opened an intriguing way to elucidate low-energy physics effectively emerging in strongly-correlated superfluid systems, and at the same time, posed many fundamental questions. Recent quantum-simulation studies in exploring far-from-equilibrium dynamics of quantum many-body systems have also posed many challenging issues to the research field of theoretical and computational physics. Among them, it is important to address the issue about how to accurately and efficiently simulate the experimentally observed non-equilibrium many-body dynamics with classical computers. The first main part of this Thesis is devoted to studying the experimental detectability of the Higgs amplitude mode as a sharp resonance peak in a strongly-correlated Bose gas trapped by an optical lattice. There, field-theoretical calculations are performed, which elucidate quantum and thermal fluctuation effects on the stability of the Higgs mode in an actual experimental situation. The second part of this Thesis is devoted to presenting a truncated-Wigner phase-space approach to far-from-equilibrium quantum quench dynamics simulated by an optical-lattice quantum simulator. A direct comparison with the actual experimental data shows a remarkable agreement with no specific free parameter: it implies a potential ability of such a semiclassical approach in simulating many-body dynamics in real experiments. Some review parts instructively explain theoretical approaches used in this Thesis, including the phase space approach to quantum dynamics and the Schwinger boson techniques for strongly-correlated systems.

Hamburg, Germany — Kazuma Nagao

Parts of this Thesis have been published in the following journal articles:

1. *Semiclassical quench dynamics of Bose gases in optical lattices*, **Kazuma Nagao**, Masaya Kunimi, Yosuke Takasu, Yoshiro Takahashi, and Ippei Danshita, https://journals.aps.org/pra/abstract/10.1103/PhysRevA.99.023622, Physical Review A **99**, 023622 (2019). Copyright 2019 by the American Physical Society.
2. *Response of the Higgs amplitude mode of superfluid Bose gases in a three-dimensional optical lattice*, **Kazuma Nagao**, Yoshiro Takahashi, and Ippei Danshita, https://journals.aps.org/pra/abstract/10.1103/PhysRevA.97.043628, Physical Review A **97**, 043628 (2018). Copyright 2018 by the American Physical Society.

Acknowledgements

First of all, I would like to express my appreciation to my research advisor, Prof. Ippei Danshita for supervising my research activities, suggesting many ideas and projects, encouraging me, and offering many opportunities to go abroad during my five-year graduate course in Yukawa Institute for Theoretical Physics (YITP). I also wish to express my gratitude to Prof. Keisuke Totsuka for supervising my graduate student life at YITP for five years and giving a lot of advice on writing this Thesis. Without their supports and advice, this Thesis would not have been finished.

I would like to thank Prof. Yoshiro Takahashi for collaborating with several projects, offering a research assistant position and financial supports, and fruitful discussions about experiments of cold atoms. I would also like to thank Prof. Anatoli Polkovnikov for giving opportunities to visit his group at Boston University, suggesting joint projects associated with the truncated-Wigner approximation, encouraging me, and many helpful discussions and comments on my studies. Furthermore, I am grateful to my collaborators of various research projects in Japan, especially, Prof. Yosuke Takasu, Dr. Masaya Kunimi, Dr. Shimpei Goto, Prof. Kenichi Kasamatsu, and Mr. Yusuke Ozaki for the collaborations, sharing unpublished data, and making fruitful discussions. These great experiences were really helpful to improve my research skills and complete this Thesis.

I would like to thank Prof. Shunji Tsuchiya, Prof. Muneto Nitta, Prof. Tetsuro Nikuni, Prof. Carlos Sá de Melo, Prof. Ludwig Mathey, Prof. Shuta Nakajima, Prof. Daisuke Yamamoto, Dr. Kazuya Fujimoto, Dr. Adam Sajna, Dr. Shainen Davidson, Dr. Dries Sels, and Mr. Jonathan Wortz for fruitful discussions and useful comments on my studies. I would also like to thank Prof. Masatoshi Sato, Prof. Ken Shiozaki, and postdoctoral members of the Condensed-Matter-Physics Group at YITP for asking useful questions and comments in my talks at the weekly seminar. I also thank current and past YITP members, especially, Dr. Koudai Sugimoto, Dr. Kiyoshi Kanazawa, Dr. Kazuya Shinjo, Dr. Tomohiko Sano, Dr. Satoshi Takada, Dr. Takumi Ohta, Dr. Hidekazu Tsukiji, Mr. Kazuhiko Tanimoto, Mr. Yukihisa Imamura, Dr. Yuki Kamiya, and Mr. Takumi Bessho for making my student life enjoyable. Finally, I am grateful to my parents and my little brother.

Contents

Chapter 1
Introduction

Abstract We review recent studies on the analog quantum simulation of Hubbard-type models implemented by means of ultracold gases trapped by an optical lattice potential. The topics include the quantum-gas microscope experiment to detect the Higgs amplitude mode of strongly-interacting superfluid bosons on a lattice and quantum-simulation studies on real-time dynamics of the Bose–Hubbard systems far from equilibrium. We show the motivation of our studies treated in this Thesis and the outline.

1.1 Backgrounds

A system of ultracold atoms in an optical lattice has offered a promising analog quantum simulator for studying quantum many-body systems encountered in condensed matter physics [1–7]. Loading degenerate Bose or Fermi atoms into optical-lattice potentials with a sufficient depth, a large variety of clean Hubbard-type models is successfully realized within the tight-binding approximation. For instance, degenerate ^{87}Rb atoms tightly trapped by a cubic optical lattice are described by the three-dimensional (3D) Bose–Hubbard model [1, 2]. One of the most important properties of such an artificial system is the high controllability of microscopic parameters, which characterize correlations among trapped particles. Indeed, the local interatomic interactions divided by the tunneling amplitude between adjacent sites can be widely controlled from weakly to strongly interacting regimes by simply changing the laser intensity of lattice [1, 2] or utilizing Feshbach resonance techniques [8]. The performance of the ultracold-gas quantum simulator has been validated through direct comparisons with quasi-exact numerical simulations on classical computers [9–14] and has attracted a lot of attention from both theoretical and experimental research areas.

As well as the advantageous feature of the system itself, there are various measurement techniques in order to detect quantum many-body states taken by an ensemble of ultracold atoms. The experimental techniques include the time-of-flight (TOF)

K. Nagao, *Fluctuations and Non-Equilibrium Phenomena in Strongly-Correlated Ultracold Atoms*, Springer Theses, https://doi.org/10.1007/978-981-15-7171-8_1

imaging technique, which takes snapshots of momentum or velocity distribution of atomic ensembles after released from a trap [2, 4], and the single-site resolved imaging technique for counting occupied sites of atoms by means of the quantum-gas microscope (QGM) [6, 7, 15]. These imaging techniques have been combined with several spectroscopic methods to identify low-energy excitations and spectral functions of a given system near equilibrium. Indeed, the TOF technique has been used to characterize excitation spectra of ultracold gases, combining with the radio-frequency spectroscopy [16], lattice shaking technique [17, 18], and standard Bragg spectroscopy [19]. More recently, the QGM imaging has been applied to estimate energy absorption after a lattice-amplitude shaking for strongly-interacting bosons on a 2D lattice [20]. This technique allows one to detect temperature increases, which are caused by the lattice modulations and estimated through counting the number of particle-hole excitations in the atomic limit, with high sensitivity. Thanks to this advantage, in the experimental work [20], Endres and his coworkers were able to achieve a linear-response regime, in which the modulation amplitude is much smaller compared with the previous studies [17, 18], so that only low-lying excitations are kicked out. They have utilized this QGM spectroscopy for *hunting* the Higgs amplitude mode, which is a fundamental excitation mode emerging in the strongly-interacting superfluid state close to the quantum phase transition, and obtained prominent results capturing the low-energy spectral properties of the strongly-correlated superfluid.

The optical-lattice system is a suitable experimental system for studying real-time dynamics of quantum systems because it is decoupled from the external environment and has a relatively long relaxation time compared with solid state systems [21]. It implies that this system has a lot of potential to gain access to far-from-equilibrium quantum many-body dynamics under a highly controlled way [22, 23]. For macroscopic many-body systems, it is generally hard to accurately simulate their real-time dynamics with currently available numerical methods on classical computers. The difficulty in *classically* simulating quantum many-body dynamics is related to the fact that, if exact numerical simulations, e.g., the exact diagonalization approaches, are carried out on computers, one encounters the exponential growth of the Hilbert-space dimension with system size. Moreover, quantitative simulations using the so-called non-equilibrium dynamical-mean-field theory (DMFT) typically employ the continuous-time quantum Monte-Carlo (CTQMC) algorithm as its impurity solver,[1] but the intrinsic minus-sign problem limits timescales, during which the real-time dynamics is accurately simulatable [24, 25]. One of the important results associated with quantum simulations of non-equilibrium real-time dynamics is the direct comparison with quasi-exact numerical simulations as done in Ref. [11]. There, numerical simulations of several quantum-quench dynamics (see also below) were carried out by means of the time-dependent density matrix renormalization group (t-DMRG), which is an established computational method formulated on the basis of the concepts of matrix-product states (MPS), and basically applicable to low-entangled systems in

[1] We note that one can also utilize other options for impurity solvers as well as the CTQMC. See also Refs. [24, 25].

1D. Trotzky and coworkers have demonstrated that the analog quantum simulator for the 1D Bose–Hubbard model can provide accurate data of quench dynamics even in a long-time region, where the t-DMRG description fails. Quantum-simulation studies [11–13], whose experimental results were compared with t-DMRG simulations, have stimulated the research field of computational physics. Considerable effort has been paid so far to explore computational approaches for quantitatively accessing long-time quantum thermalization dynamics of 1D systems beyond the limitation of t-DMRG. The most recent developments include the density-matrix truncation (DMT) theory [26] and the time-dependent variational principle (TDVP) with MPS [27–30].

Among diverse quantum many-body dynamics, particular attention has been devoted to quantum quench dynamics, which arise after a sudden and substantial change of parameters in the Hamiltonian [11, 12, 22, 23, 31–38]. In Ref. [11], Trotzky and coworkers have investigated relaxation dynamics of Bose gases in a 1D optical lattice after sudden quantum quenches from a simple density pattern over the lattice, and detected that the local density relaxes into a steady value within experimental timescales. In Ref. [12], Cheneau and coworkers have observed effective light-cone dynamics of an equal-time correlation function in a 1D optical lattice, and they demonstrated that in the strongly interacting region the propagation speed is bounded by the maximum group velocity of particle-hole excitations. In recent years, some experimental groups have explored far-from-equilibrium dynamics of high-dimensional Bose–Hubbard systems quenched from typical quantum states [13, 39, 40]. The Max-Planck institute group has explored the Kibble–Zurek dynamics after a finite-time quench across the quantum phase transition from the Mott-insulator (disorder) to superfluid (order) phases in the Bose–Hubbard models in all spatial dimensions, i.e., $d = 1, 2, 3$ [13, 39]. More recently, an experimental group at Kyoto University has observed redistribution dynamics of kinetic and onsite-interaction energies of Bose gases in a cubic optical lattice after a rapid quench of the lattice depth from a strongly-interacting Mott insulator state into a weakly-interacting parameter region [40].

1.2 Motivation

Motivated by these experimental developments and prominent results, in this Thesis, we present the results of theoretical analyses of near- and far-from-equilibrium dynamics of ultracold Bose gases in optical lattices. In the first part of this Thesis, motivated by the experiment [20] in the Max-Planck institute, we examine the stability and detectability (or *visibility*) of the Higgs mode in the ultracold-gas systems. Theoretical calculations [41–49] stimulated by the same experiment have argued that the Higgs mode strongly attenuates in two dimensions due to the combined effects of the quantum and thermal fluctuations with the spatial inhomogeneity of the trapping potential. Indeed, in Ref. [20], the measured response, which is a function of the modulation frequency of the lattice depth, exhibits a broad continuum above a

threshold frequency rather than a sharp peak although the frequency coincides well with the Higgs gap, which is calculated theoretically. In this sense, the existence of a stable Higgs mode in the cold-atomic systems remains to be an open issue. This Thesis presents the following way toward catching a stable Higgs mode: if we consider a 3D optical lattice instead of 2D one and perturb the condensate only partially around the center of the trap, at which the density is tuned to unity as in Ref. [20], we can observe a sufficiently-stable Higgs mode in the corresponding response function even at typical temperatures of experiments. Our theoretical approach, which is a generalization of the finite-temperature Green's function theory developed by the current author and Danshita previously [50], incorporates both quantum and thermal fluctuation effects within the leading 1-loop order. Combining this field-theoretical method and the local density approximation, we elucidate non-uniform confinement effects on the *uniform* response functions, which are calculated with assumptions of no confinement trap. Furthermore, to discuss the responses of the Higgs mode, we formulate linear-response functions to two external perturbations, i.e., the modulation in the lattice amplitude and in the on-site interacting strength, respectively. In particular, the latter scheme is first considered by our work in the context of exploring the Higgs mode.

In the second part, motivated by the experiment [40] at Kyoto University, we investigate far-from-equilibrium quantum-quench dynamics of Bose gases in higher-dimensional optical lattices than 1D. Takasu and coworkers reported that the kinetic and interaction energies quickly evolved into (transient) steady values after the lattice depth was abruptly decreased from the values corresponding to Mott-insulating states. Moreover, the experimental results have remarkably shown that the sum of these energies is conserved at early times reflecting the isolation of the atomic ensemble. An immediate use of such fundamental results is to examine or develop numerical methods for computing quantum many-body dynamics by taking them as accurate references. Nevertheless, any quantitative approach that can recover the experimental results in three dimensions has not been established thus far. In this Thesis, aiming to simulate the energy-redistribution dynamics quantitatively, we adopt a semiclassical approximation formulated by a phase-space representation of quantum systems, namely, the truncated-Wigner approximation (TWA), which systematically provides a leading-order correction of fluctuations to the mean-field or saddle-point dynamics [51–53]. This method is formulated on the basis of a quantum-to-classical mapping in which computing the quantum average of an operator is replaced with a classical problem of solving Gross–Pitaevskii-type equations for classical Bose fields obeying *random* initial conditions sampled from an initial Wigner function (some advantages of this method will be explained in a later chapter). In this Thesis, generalizing the previous TWA techniques [33, 54, 55] developed for quantum quenches starting from a Mott-insulator state at high densities, we numerically simulate the redistribution dynamics of the kinetic and interaction energies in the 3D system starting from the opposite limit, i.e., a Mott insulator at unit filling. Comparing the semiclassical and experimental results directly, it is demonstrated that numerical results simulated by the TWA agree well with the experimental data with no fitting parameter.

As a further application of the TWA, we also study how the density-density correlation function between two distant points spreads and grows after a sudden quench in Bose gases trapped by a 2D optical lattice. This application is motivated by experimental and theoretical works in ultracold neutral atoms, trapped ions, and interacting spin systems [12, 56–63]. Thus far, the correlation spreading and its relationship with the Lieb–Robinson bound [64], which gives an upper bound of information propagation over space, have been studied mostly in 1D systems. Theoretically, this is due to the limitation of currently-available tools to simulate dynamics of non-local correlations. More recently, spreading of spatial correlations in two dimensions has been explored by some works [40, 65–67], whereas their quantitative properties are, however, less understood compared with the 1D case. In this Thesis, we focus on the semiclassical regime of the 2D Bose–Hubbard model, and analyze the time evolution of the equal-time density-density correlation function for different initial states. We find that when the system is initially prepared in a coherent state that describes the ground state in the non-interacting limit, a mean propagation velocity of a wave packet observed in the density-density correlation function strongly depends on the final interaction. In contrast, when the system is initially in a Mott-insulator state, the wave packet in the density-density correlation function propagates with a nearly constant velocity with respect to the final interaction.

1.3 Outline of This Thesis

This Thesis is organized as follows: In Chap. 2, we review ultracold Bose gases trapped by optical lattice potentials. There, we first derive the single-band Bose–Hubbard model within the tight-binding approximation, and then, we summarize the ground state properties of the Bose–Hubbard model focusing on the superfluid-Mott-insulator quantum phase transitions. In addition, we discuss the collective excitations of the strongly-correlated superfluid near the transition. In the final part of this chapter, we introduce an effective pseudospin-1 Hamiltonian of the Bose–Hubbard model allowing us to investigate low-energy properties in the strongly-correlated regime. This approach will be used in Chap. 4 to analyze the response functions in combination with the field-theoretical linear-response theory and the local-density approximation.

In Chap. 3, we review the phase-space method for expressing quantum systems by means of c-number functions defined in a phase space. There, we especially focus on the coherent-state Wigner representation of Bose fields. The fundamental ingredients constructing the Wigner representation, i.e., the Wigner function and the Weyl symbol, are introduced to rewrite the quantum average of an arbitrary operator into an entirely classical form. The coherent-state phase-space representation of dynamics of Bose fields is formulated in terms of the time-dependent Wigner function. From this representation, we derive the TWA as a semiclassical approximation for the time evolution of the Wigner function. There, we also illustrate the schematic picture and advantages of the TWA. Furthermore, we review an instructive approach

to derive the semiclassical approximation starting from a phase-space path-integral representation of quantum dynamics.

In Chap. 4, which is based on Ref. [68], we study the responses of the Higgs modes to the temporal modulations of the lattice amplitude and the onsite-interaction strength in the cubic optical lattice. We analyze the linear-response functions by the perturbative calculation of the finite-temperature Green's function for the effective pseudospin-1 model at high and unit fillings. It is shown that when the density of the system is assumed to be uniform, we can observe a well-defined Higgs-type resonance peak in the response functions even at the typical temperature scale in the current experiments. Furthermore, we calculate the effects of a non-uniform trap on the response functions within the local density approximation, and discuss the robustness of the resonance peak against the non-uniformity. There, we argue that if we perturb a part of the condensate, which is distributed over a subregion around the trap center, the resonance peak still survives at typical temperatures.

In Chap. 5, which describes the results obtained in Ref. [69], we investigate far-from-equilibrium dynamics of Bose gases in optical lattices after sudden quantum quenches. Using the TWA, we numerically simulate the redistribution dynamics of the kinetic and onsite-interaction energies after a sudden quench from a Mott insulating state in a 3D optical lattice. Our results reveal that the results obtained by the TWA agree well with the experimental data without any fitting parameter. Furthermore, we analyze correlation spreading dynamics after a sudden quench in a 2D optical lattice. We focus especially on the initial state dependence of the behavior of the correlation spreading.

In Chap. 6, we conclude this Thesis and present outlooks to future subjects. Finally, Appendices A and B offer supplemental information for the main part.

References

1. D. Jaksch, C. Bruder, J.I. Cirac, C.W. Gardiner, P. Zoller, Phys. Rev. Lett. **81**, 3108 (1998)
2. M. Greiner, O. Mandel, T. Esslinger, T.W. Hänsch, I. Bloch, Nature **415**, 39 (2002)
3. D. Jaksch, P. Zoller, Ann. Phys. **315**, 52 (2005)
4. I. Bloch, J. Dalibard, W. Zwerger, Rev. Mod. Phys. **80**, 885 (2008)
5. M. Lewenstein, A. Sanpera, V. Ahufinger, *Ultracold Atoms in Optical Lattices: Simulating Quantum Many-Body Systems* (Oxford University Press, Oxford, 2012)
6. C. Gross, I. Bloch, Science **357**, 995 (2017)
7. W. Hofstetter, T. Qin, J. Phys. B: At. Mol. Opt. Phys. **51**, 082001 (2018)
8. C. Chin, R. Grimm, P. Julienne, E. Tiesinga, Rev. Mod. Phys. **82**, 1225 (2010)
9. S. Trotzky, L. Pollet, F. Gerbier, U. Schnorrberger, I. Bloch, N.V. Prokof'ev, B. Svistunov, M. Troyer, Nat. Phys. **6**, 998 (2010)
10. M. Endres, M. Cheneau, T. Fukuhara, C. Weitenberg, P. Schauß, C. Gross, L. Mazza, M.C. Baũls, I. Bloch, S. Kuhr, Science **334**, 200 (2011)
11. S. Trotzky, Y.-A. Chen, A. Flesch, I.P. McCulloch, U. Schollwöck, J. Eisert, I. Bloch, Nat. Phys. **8**, 325 (2012)
12. M. Cheneau, P. Barmettler, D. Poletti, M. Endres, P. Schauß, T. Fukuhara, C. Gross, I. Bloch, C. Kollath, S. Kuhr, Nature **481**, 484 (2012)

13. S. Braun, M. Friesdorf, S.S. Hodgman, M. Schreiber, J.P. Ronzheimer, A. Riera, M. del Rey, I. Bloch, J. Eisert, U. Schneider, PNAS **112**, 3641 (2015)
14. A. Mazurenko, C.S. Chiu, G. Ji, M.F. Parsons, M. Kanász-Nagy, R. Schmidt, F. Grusdt, E. Demler, D. Greif, M. Greiner, Nature **545**, 462 (2017)
15. D. Greif, M.F. Parsons, A. Mazurenko, C.S. Chiu, S. Blatt, F. Huber, G. Ji, M. Greiner, Science **351**, 953 (2016)
16. J.T. Stewart, J.P. Gaebler, D.S. Jin, Nature **454**, 744 (2008)
17. T. Stöferle, H. Moritz, C. Schori, M. Köhl, T. Esslinger, Phys. Rev. Lett. **92**, 130403 (2004)
18. C. Schori, T. Stöferle, H. Moritz, M. Köhl, T. Esslinger, Phys. Rev. Lett. **93**, 240402 (2004)
19. U. Bissbort, S. Götze, Y. Li, J. Heinze, J.S. Krauser, M. Weinberg, C. Becker, K. Sengstock, W. Hofstetter, Phys. Rev. Lett. **106**, 205303 (2011)
20. M. Endres, T. Fukuhara, D. Pekker, M. Cheneau, P. Schauβ, C. Gross, E. Demler, S. Kuhrm, I. Bloch, Nature **487**, 454 (2012)
21. E. Altman, arXiv:1512.0870 [cond-mat.quant-gas]
22. A. Polkovnikov, K. Sengupta, A. Silva, M. Vengalattore, Rev. Mod. Phys. **83**, 863 (2011)
23. J. Eisert, M. Friesdorf, C. Gogolin, Nat. Phys. **11**, 124 (2015)
24. H. Aoki, N. Tsuji, M. Eckstein, M. Kollar, T. Oka, P. Werner, Rev. Mod. Phys. **86**, 779 (2014)
25. H.U.R. Strand, M. Eckstein, P. Werner, Phys. Rev. X **5**, 011038 (2015)
26. C.D. White, M. Zaletel, R.S.K. Mong, G. Refael, Phys. Rev. B **97**, 035127 (2018)
27. J. Haegeman, J.I. Cirac, T.J. Osborne, I. Pižorn, H. Verschelde, F. Verstraete, Phys. Rev. Lett. **107**, 070601 (2011)
28. J. Haegeman, T.J. Osborne, F. Verstraete, Phys. Rev. B **88**, 075133 (2013)
29. J. Haegeman, C. Lubich, I. Oseledets, B. Vandereycken, F. Verstraete, Phys. Rev. B **94**, 165116 (2016)
30. S. Goto, I. Danshita, Phys. Rev. B **99**, 054307 (2019)
31. M. Greiner, O. Mandel, T.W. Hänsch, I. Bloch, Nature **419**, 51 (2002)
32. E. Altman, A. Auerbach, Phys. Rev. Lett. **89**, 250404 (2002)
33. A.K. Tuchman, C. Orzel, A. Polkovnikov, M.A. Kasevich, Phys. Rev. A **74**, 051601(R) (2006)
34. R. Schützhold, M. Uhlmann, Y. Xu, U.R. Fischer, Phys. Rev. Lett. **97**, 200601 (2006)
35. C. Kollath, A.M. Läuchli, E. Altman, Phys. Rev. Lett. **98**, 180601 (2007)
36. U.R. Fischer, R. Schützhold, M. Uhlmann, Phys. Rev. A **77**, 043615 (2008)
37. J. Dziarmaga, M. Tylutki, W.H. Zurek, Phys. Rev. B **86**, 144521 (2012)
38. F. Meinert, M.J. Mark, E. Kirilov, K. Lauber, P. Weinmann, A.J. Daley, H.-C. Nägerl, Phys. Rev. Lett. **111**, 053003 (2013)
39. S. Braun, Negative temperature and the dynamics of quantum phase transitions. Ph.D. thesis, Ludwig-Maximilians-Universität München (2014)
40. Y. Takasu, T. Yagami, H. Asaka, Y. Fukushima, K. Nagao, S. Goto, I. Danshita, Y. Takahashi, arXiv:2002.12025 [cond-mat.quant-gas]
41. D. Podolsky, A. Auerbach, D.P. Arovas, Phys. Rev. B **84**, 174522 (2011)
42. D. Podolsky, S. Sachdev, Phys. Rev. B **86**, 054508 (2012)
43. S. Gazit, D. Podolsky, A. Auerbach, Phys. Rev. Lett. **110**, 140401 (2013); Phys. Rev. B **88**, 235108 (2013)
44. A. Rançon, N. Dupuis, Phys. Rev. B **89**, 180501(R) (2014)
45. Y.T. Katan, D. Podolsky, Phys. Rev. B **91**, 075132 (2015)
46. F. Rose, F. Léonard, N. Dupuis, Phys. Rev. B **91**, 224501 (2015)
47. L. Pollet, N. Prokof'ev, Phys. Rev. Lett. **109**, 010401 (2012)
48. L. Liu, K. Chen, Y. Deng, M. Endres, L. Pollet, N. Prokof'ev, Phys. Rev. B **92**, 174521 (2015)
49. K. Chen, L. Liu, Y. Deng, L. Pollet, N. Prokof'ev, Phys. Rev. Lett. **110**, 170403 (2013)
50. K. Nagao, I. Danshita, Prog. Theor. Exp. Phys. **2016**, 063I01 (2016)
51. D. Walls, G. Milburn, *Quantum Optics* (Springer, Berlin, 1994)
52. P.B. Blakie, A.S. Bradley, M.J. Davis, R.J. Ballagh, C.W. Gardiner, Adv. Phys. **57**, 363 (2008)
53. A. Polkovnikov, Ann. Phys. **325**, 1790 (2010)
54. A. Polkovnikov, S. Sachdev, S.M. Girvin, Phys. Rev. A **66**, 053607 (2002)
55. A. Polkovnikov, Phys. Rev. A **68**, 033609 (2003)

56. J. Jünemann, A. Cadarso, D. Pérez-García, A. Bermudez, J.J. García-Ripoll, Phys. Rev. Lett. **111**, 230404 (2013)
57. P. Hauke, L. Tagliacozzo, Phys. Rev. Lett. **111**, 207202 (2013)
58. J. Schachenmayer, B.P. Lanyon, C.F. Roos, A.J. Daley, Phys. Rev. X **3**, 031015 (2013)
59. P. Richerme, Z.-X. Gong, A. Lee, C. Senko, J. Smith, M. Foss-Feig, S. Michalakis, A.V. Gorshkov, C. Monroe, Nature **511**, 198 (2014)
60. P. Jurcevic, B.P. Lanyon, P. Hauke, C. Hempel, P. Zoller, R. Blatt, C.F. Roos, Nature **511**, 202 (2014)
61. L. Bonnes, F.H.L. Essler, A.M. Läuchli, Phys. Rev. Lett. **113**, 187203 (2014)
62. A.M. Läuchli, C. Kollath, J. Stat. Mech. P05018 (2008)
63. P. Barmettler, D. Poletti, M. Cheneau, C. Kollath, Phys. Rev. A **85**, 053625 (2012)
64. E.H. Lieb, D.W. Robinson, Commun. Math. Phys. **28**, 251 (1972)
65. G. Carleo, F. Becca, L. Sanchez-Palencia, S. Sorella, M. Fabrizio, Phys. Rev. A **89**, 031602(R) (2014)
66. K.V. Krutitsky, P. Navez, F. Queisser, R. Schützhold, EPJ Quantum Technol. **1**, 1 (2014)
67. J. Schachenmayer, A. Pikovski, A.M. Rey, New J. Phys. **17**, 065009 (2015)
68. K. Nagao, Y. Takahashi, I. Danshita, Phys. Rev. A **97**, 043628 (2018)
69. K. Nagao, M. Kunimi, Y. Takasu, Y. Takahashi, I. Danshita, Phys. Rev. A **99**, 023622 (2019)

Chapter 2
Ultracold Bose Gases in Optical Lattices

Abstract In this chapter, we review the basic properties of ultracold Bose gases tightly trapped by optical lattice potentials. In Sect. 2.1, we briefly describe the optical-dipole potentials for trapping neutral atoms and show how one generates optical lattice potentials in laboratories. In Sect. 2.2, we derive the single-band Bose–Hubbard model within the tight-binding approximation. In Sect. 2.3, we review the superfluid-Mott-insulator quantum phase transition of the ground state of the Bose–Hubbard model. In Sect. 2.4, we discuss collective excitation modes in the superfluid phase near the Mott-insulator transition. In Sect. 2.5, we formulate an effective-model description for the strongly-correlated regime by using Hilbert-space truncation techniques. This description will be used in Chap. 4 in order to analyze dynamical properties of strongly-correlated bosons in the vicinity of the superfluid-Mott-insulator transition.

2.1 Optical-Lattice Potentials

The spatially-periodic optical-lattice potential is a key ingredient to realize various Hubbard-type models in ultracold-gas experiments. Optical lattices are generated by standing-wave lasers far detuned from an atomic resonance in order to confine neutral atoms inside a lattice geometry of interest without optical dissipations [1]. When an atom is put in the presence of an oscillating (off-resonant) laser field $\boldsymbol{E}(\mathbf{r}, t)$ with an angular frequency ω_L, and the frequency is detuned sufficiently far from the atomic resonance, then, a conservative force effectively acts on the atom, which is described by a laser-induced dipole potential [2–4]:

$$V_{\mathrm{ind}}(\mathbf{r}) = -\frac{1}{2}\mathrm{Re}\left[\alpha(\omega_L)\right]\overline{|\boldsymbol{E}(\mathbf{r}, t)|^2}, \tag{2.1}$$

where $\alpha(\omega_L)$ is referred to as the complex AC polarizability and the overline indicates a time average. The induced potential can be regarded as an effective shift of atomic

K. Nagao, *Fluctuations and Non-Equilibrium Phenomena in Strongly-Correlated Ultracold Atoms*, Springer Theses, https://doi.org/10.1007/978-981-15-7171-8_2

levels due to laser-induced virtual transitions between unperturbed atomic states, i.e., the AC Stark effect [2, 3]. The strength and sign of Eq. (2.1) depend on the laser intensity and frequency ω_L.

To visualize optical lattices concretely, let us consider a superimposing pair of two counter-propagating lasers with the same wavelength $\lambda_{\rm lat}$ along x-direction

$$\boldsymbol{E}(x,t) = \hat{\boldsymbol{e}} E_0 \cos(k_{\rm lat} x) \left[e^{-i\omega_L t} + \text{c.c.} \right]. \tag{2.2}$$

Here, $k_{\rm lat} = 2\pi/\lambda_{\rm lat}$ is the wave number and $\hat{\boldsymbol{e}}$ denotes a unit vector oriented to the polarized direction. The consequence of Eq. (2.1) is that, in the presence of this oscillating laser field, atoms are trapped around periodic wells of a one-dimensional lattice potential, which is denoted by

$$V_{\rm lat}^{\rm 1D}(x) = V_0 \cos^2(k_{\rm lat} x). \tag{2.3}$$

The lattice depth V_0 can be controlled by tuning the laser intensity $I \sim E_0^2$. The lattice spacing between two potential minima, $d_{\rm lat}$, is determined from the wavelength such that $d_{\rm lat} = \lambda_{\rm lat}/2$. It is convenient to measure the lattice depth V_0 with units of the recoil energy $E_{\rm R}$, which is given by

$$E_{\rm R} = \frac{\hbar^2 k_{\rm lat}^2}{2m} = \frac{\hbar^2 \pi^2}{2m d_{\rm lat}^2}. \tag{2.4}$$

In the context of cold atoms, the optical lattice potentials are conventionally written as

$$V_{\rm lat}^{\rm 1D}(x) = s E_{\rm R} \cos^2(k_{\rm lat} x), \tag{2.5}$$

where $s = V_0/E_{\rm R}$. The recoil energy implies an acquired energy of an atom after absorbing or emitting a photon with momentum $\hbar k_{\rm lat}$ from the laser field.

Inserting additional laser beams from different directions, one can also realize a two-dimensional square or three-dimensional cubic optical lattice:

$$V_{\rm lat}^{\rm 2D}(x,y) = s E_{\rm R} \left[\cos^2(k_{\rm lat} x) + \cos^2(k_{\rm lat} y) \right], \tag{2.6}$$

$$V_{\rm lat}^{\rm 3D}(x,y,z) = s E_{\rm R} \left[\cos^2(k_{\rm lat} x) + \cos^2(k_{\rm lat} y) + \cos^2(k_{\rm lat} z) \right]. \tag{2.7}$$

Furthermore, it is possible to engineer various types of optical-lattice potential with non-trivial geometries in ultracold-gas experiments. The examples established thus far include the double-well superlattice [5], checkerboard geometry [6], honeycomb (or hexagonal) lattice [7], triangular lattice [8, 9], Kagome lattice [10], and Lieb lattice [11]. For reviews, see Refs. [12–14].

2.2 Bose–Hubbard Models

Let us consider an ultracold gas of spinless Bose atoms with an atomic mass m in the presence of a cubic optical lattice

$$V_{\rm lat}(\mathbf{r}) = s E_{\rm R}\left[\sin^2(k_{\rm lat}x) + \sin^2(k_{\rm lat}y) + \sin^2(k_{\rm lat}z)\right]. \tag{2.8}$$

This system is described by the following second-quantized Hamiltonian [1]:

$$\hat{H}_{\rm b} = \int d\mathbf{r}\ \hat{\psi}^\dagger(\mathbf{r})\left[-\frac{\hbar^2\nabla^2}{2m} + V_{\rm lat}(\mathbf{r})\right]\hat{\psi}(\mathbf{r}) + \frac{g}{2}\int d\mathbf{r}\ \hat{\psi}^\dagger(\mathbf{r})\hat{\psi}^\dagger(\mathbf{r})\hat{\psi}(\mathbf{r})\hat{\psi}(\mathbf{r}), \tag{2.9}$$

where $g = 4\pi\hbar^2 a_{\rm s}/m$ and $a_{\rm s}$ are the coupling constant and s-wave scattering length, respectively. The boson annihilation and creation operators $\hat{\psi}(\mathbf{r})$ and $\hat{\psi}^\dagger(\mathbf{r})$ satisfy the canonical commutation relations:

$$[\hat{\psi}(\mathbf{r}), \hat{\psi}^\dagger(\mathbf{r}')] = \delta(\mathbf{r}-\mathbf{r}'), \quad [\hat{\psi}(\mathbf{r}), \hat{\psi}(\mathbf{r}')] = [\hat{\psi}^\dagger(\mathbf{r}), \hat{\psi}^\dagger(\mathbf{r}')] = 0. \tag{2.10}$$

When the lattice potential is sufficiently deep, the lowest-lying first band is most dominant and the higher-band contributions are negligible because the energy gap of the first and second bands is much larger than the thermal and mean-field interaction energies per atom [15]. Therefore, it is allowed to expand the Bose field operator with respect to the lowest-band Wannier basis:

$$\hat{\psi}(\mathbf{r}) = \sum_i \hat{a}_i w_0(\mathbf{r}-\mathbf{R}_i), \quad \hat{\psi}^\dagger(\mathbf{r}) = \sum_i \hat{a}_i^\dagger w_0^*(\mathbf{r}-\mathbf{R}_i), \tag{2.11}$$

where $i = (i_x, i_y, i_z)$ is an integer-valued vector and $\mathbf{R}_i = d_{\rm lat}(i_x, i_y, i_z)$ indicates the lattice minima. The function $w_0(\mathbf{r}-\mathbf{R}_i)$ is the lowest-band Wannier function, which is supposed to be localized around $\mathbf{r} = \mathbf{R}_i$. The new canonical operators $\hat{a}_i$ and $\hat{a}_i^\dagger$ are introduced so that

$$[\hat{a}_i, \hat{a}_j^\dagger] = \delta_{i,j}, \quad [\hat{a}_i, \hat{a}_j] = [\hat{a}_i^\dagger, \hat{a}_j^\dagger] = 0. \tag{2.12}$$

The lattice operator $\hat{a}_i$ annihilates a boson localized around ith site.

Substituting Eq. (2.11) into Eq. (2.9) and making the tight-binding approximation, we obtain the single-band Bose–Hubbard model [1, 16],

$$\hat{H}_{\rm b} \approx \hat{H}_{\rm BH} = -J\sum_{\langle i,j\rangle}(\hat{a}_i^\dagger\hat{a}_j + {\rm h.c.}) + \frac{U}{2}\sum_i \hat{a}_i^\dagger\hat{a}_i^\dagger\hat{a}_i\hat{a}_i, \tag{2.13}$$

where the bracket symbol $\langle i, j\rangle$ implies a nearest neighbor pair. In this representation, the first term means the kinetic energy associated with hopping of atoms from site

to site. The second term gives the energy increase when multiple atoms occupy a site at the same time. These energies are characterized by the hopping amplitude J and the onsite-interaction strength U. They are described by the localized Wannier functions such that

$$J = -\int d\mathbf{r}\, w_0^*(\mathbf{r}-\mathbf{R}_i)\left[-\frac{\hbar^2\nabla^2}{2m} + V_{\rm lat}(\mathbf{r})\right] w_0(\mathbf{r}-\mathbf{R}_j), \tag{2.14}$$

$$U = g\int d\mathbf{r}\, |w_0(\mathbf{r})|^4, \tag{2.15}$$

where $|i-j|=1$. No offset term per each site is assumed to arise from Eq. (2.14) at $i=j$. In experiments, the dimensionless ratio J/U is tunable through changing the optical-lattice depth or using the Feshbach resonance [1, 12, 17, 18].

To illustrate the dependence of J and U on the lattice depth, here we extract approximate results of them from Ref. [12]. In three dimensions and for a deep-lattice limit $s \gg 1$, they approximately behave like

$$J \sim \frac{4}{\sqrt{\pi}} s^{3/4} \exp\left(-2\sqrt{s}\right) E_{\rm R}, \tag{2.16}$$

$$U \sim \frac{8}{\pi}\frac{a_{\rm s}}{d_{\rm lat}} A_I^3 s^{3B_I} E_{\rm R}, \tag{2.17}$$

where $(A_I, B_I) = (\sqrt{\pi/2}, 1/4)$. As s increases, the hopping amplitude decreases exponentially because it characterizes a tunneling property between adjacent sites. In contrast, the interaction strength algebraically grows with s.

In typical setups of cold-atomic experiments, there is also a non-uniform external potential to confine the atoms. If effects of the confinement cannot be neglected, we have to insert an additional term into Eq. (2.13). Indeed, in the existence of a non-uniform trapping potential $V_{\rm trap}(\mathbf{r})$, which varies slowly over space, the Bose–Hubbard model acquires a local offset energy [1]:

$$\hat{H}_{\rm trap} = \sum_i \epsilon_i \hat{a}_i^\dagger \hat{a}_i, \tag{2.18}$$

where the one-body offset ϵ_i is given by

$$\epsilon_i = \int d\mathbf{r}\, V_{\rm trap}(\mathbf{r})|w_0(\mathbf{r}-\mathbf{R}_i)|^2 \approx V_{\rm trap}(\mathbf{R}_i). \tag{2.19}$$

Trapping effects will be important when we discuss the stability of the Higgs mode corresponding to experimental systems. The details will be presented in Chap. 4.

Here it is convenient to introduce the grand canonical representation of the Bose–Hubbard model:

$$\hat{\mathcal{H}}_{\mathrm{BH}} = -J \sum_{\langle i,j \rangle} (\hat{a}_i^\dagger \hat{a}_j + \mathrm{H.c.}) + \frac{U}{2} \sum_i \hat{a}_i^\dagger \hat{a}_i^\dagger \hat{a}_i \hat{a}_i - \mu \sum_i \hat{a}_i^\dagger \hat{a}_i. \tag{2.20}$$

For the cold-atomic systems, the chemical potential μ is generally dependent on the site due to the trapping potential. Such a non-uniform effect is given by the offset energy ϵ_i.

2.3 Superfluid-Mott-Insulator Quantum Phase Transitions

The Bose–Hubbard model has two different ground states (so called *quantum phases*) depending on the dimensionless local interaction U/J and the mean occupation per site [16]. When the density is incommensurate, the bosons can form a superfluid phase at zero temperature for any local and positive interactions. In contrast, when the density is commensurate and the interaction becomes greater than a threshold value, the ground state undergoes a phase transition into a Mott-insulator phase at zero temperature. Such a zero-temperature transition, which is essentially driven by quantum fluctuations stemming from competition between two non-commutative parts in $\hat{H}_{\mathrm{BH}}$, i.e., the kinetic and interaction energies, is called *quantum phase transitions* [19]. The quantum phase transition should be contrasted with conventional classical phase transitions, which are induced by thermal fluctuations.

When the spatial dimension is greater than one ($d > 1$), the superfluid state exhibits a long-range order while the insulator state is disordered [16]. Then, the transition is regarded as a second-order transition [16, 19–22]. The phases are distinguished by a local complex number (order parameter) associated with spontaneous breaking of U(1) symmetry. On the other hand, in one dimension ($d = 1$), there is no phase transition with continuous-symmetry breaking even at zero temperature (the Mermin–Wagner–Coleman theorem [23, 24]) because long-range orders are melted by strong quantum fluctuations. Nevertheless, the one-dimensional ground state can exhibit a *topological* phase transition without symmetry breaking, which is referred to as the Berezinskii–Kosterlitz–Thouless transition [25–29].

The Mott-insulator state is incompressible and has two gapped elementary excitations, i.e., the particle and hole excitations [16]. Both of these energy gaps vanish at the phase transition point. On the other hand, the superfluid state is compressible and has a gapless excitation. For $d > 1$ this excitation is nothing else but the Nambu–Goldstone (NG) mode. In contrast, at $d = 1$, the gapless excitation, which is related with the existence of the quasi-long range order with a power law decay, is universally described by the Tomonaga–Luttinger liquid theory [29].

The superfluid-Mott-insulator transition is characterized by the behaviors of the energy gap Δ and correlation length ξ [19]. Approaching the transition point, the energy gap vanishes and the correlation length diverges as

$$\Delta \sim J|w - w_c|^{\nu z_{\mathrm{dyn}}}, \quad \xi^{-1} \sim d_{\mathrm{lat}}^{-1} |w - w_c|^{\nu}, \tag{2.21}$$

where w is a dimensionless parameter and w_c indicates the transition point. The so called critical exponents ν and $z_{\rm dyn}$ are usually independent of the microscopic detail of the lattice system [19]. In the vicinity of the transition point, associated with the divergence of the time and length scales, some important physical quantities, e.g., correlation functions of the ground state, obtain a scaling form described by a set of such *universal* critical exponents. The superfluid-Mott-insulator transition belongs to the universality class of the critical phenomena of the $(d+1)$-dimensional classical XY model [16]. In particular, the dynamical exponent $z_{\rm dyn}$ is predicted as $z_{\rm dyn}=1$. We can also induce a similar superfluid-insulator transition by varying the mean occupancy or chemical potential [16]. Then, the transition is described by the universality class of the dilute Bose-gas transition, and the dynamical exponent is not unity, but $z_{\rm dyn}=2$ [19].

The superfluid-Mott-insulator transition of the Bose–Hubbard model has been observed experimentally in ultracold ^{87}Rb atoms in a 3D optical lattice [17]. In the experiment, interference patterns of expanding gases released from external potentials were imaged by using the time-of-flight technique at different optical-lattice depths. The experimental results clearly detected a characteristic onset of the quantum phase transition, i.e., losing or restoring of phase coherence in the interference patterns.

2.3.1 Mean-Field Theory of the Superfluid-Mott-Insulator Transition

Mean-field calculations are helpful in roughly imagining the ground state properties of the Bose–Hubbard model. The superfluid-Mott-insulator transition can be described within several mean-field treatments such as the site-decoupling mean-field approach [20] and Gutzwiller's variational ansatz [30–33]. It should be stressed that the phase transition into the Mott-insulator state cannot be captured within the standard Bogoliubov approximation [20].

According to Ref. [20], let us determine the phase boundary using the site-decoupling mean-field approximation. In this scheme, we need to approximate the (non-local) kinetic-energy operator in the Bose–Hubbard model into a local operator such that

$$\hat{a}_i^\dagger \hat{a}_j = \psi(\hat{a}_i^\dagger + \hat{a}_j) - \psi^2, \tag{2.22}$$

where ψ is a mean field, $\psi = \langle \hat{a}_i \rangle$, and it is assumed to be real. Performing this approximation, computing the ground state energy, and making the Ginzburg–Landau expansion, we obtain the value of the chemical potential at the phase boundary, which is a function of zJ/U and the filling factor n_0 of the Mott-insulator phase:

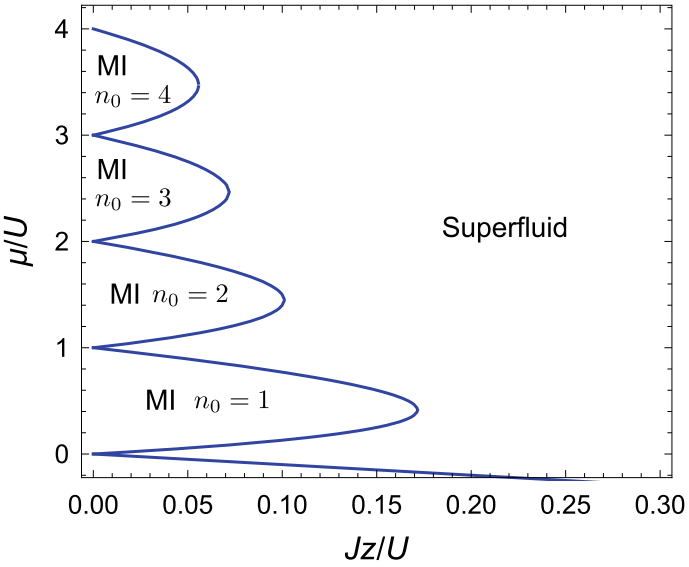

Fig. 2.1 Mean-field phase diagram of the Bose–Hubbard model at zero temperature. The vertical axis is the chemical potential and the horizontal axis is the tunneling amplitude. The blue-solid line indicates the phase boundary derived from the site-decoupling mean-field approximation (see also Ref. [20]). Each "lobe" corresponds to a Mott-insulator regime with occupation n_0

$$\mu_{\pm} = \frac{1}{2}(2n_0 - 1 - Jz/U) \pm \frac{1}{2}\sqrt{1 - 2(Jz/U)(2n_0 + 1) + (Jz/U)^2}, \quad (2.23)$$

where $z = 2d$ is the coordination number. The subscript $\pm$ indicates the upper and lower lines of the Mott-insulator regimes. In Fig. 2.1, we draw Eq. (2.23) in the zJ-μ plane. The phase boundary has a lobe-like shape, which surrounds the regimes of the Mott-insulator phase. It should be noted that each tip of the Mott lobes corresponds to a commensurate density. Equating μ_+ and μ_-, we obtain the critical value of the commensurate phase transition at the tips:

$$\left(\frac{U}{zJ}\right)_c = 2n_0 + 1 + \sqrt{(2n_0 + 1)^2 - 1} = (\sqrt{n_0 + 1} + \sqrt{n_0})^2. \quad (2.24)$$

As we will see in Sect. 2.5.4, the entirely same result can be derived from the Gutzwiller approach.

For getting precise results beyond the qualitative mean-field approximation, it is necessary to deal with quantum fluctuation effects by employing complicated non-perturbative methods. For the unit-filling case, the precise phase boundary has been computed by some quasi-exact numerical techniques, e.g., the quantum Monte-Carlo (QMC) approaches for $d = 2$ [21] and $d = 3$ [22], and the density matrix

renormalization group (DMRG) approach for $d = 1$ [34]. For the cases of large filling rates, one can also quantitatively evaluate the ground-state phase boundary by using the techniques of the strong-coupling expansion [35].

2.3.2 Field-Theoretical Description for the Quantum Phase Transition

In Sect. 2.4, we will review the Higgs mode of superfluid Bose gases near the quantum phase transition. For the purpose, let us here introduce a field-theoretical description for the transition [19, 36]. Our starting point is a grand-canonical partition function of the Bose–Hubbard model (2.20), which is written as a coherent-state path-integral form [19, 36]:

$$\Xi = \int \mathcal{D}a^* \mathcal{D}a \; e^{-S_{\rm BH}[a^*,a]}. \tag{2.25}$$

The weight function of the path integral is characterized by the Euclidean action for the Bose–Hubbard model,

$$\begin{aligned} S_{\rm BH}[a^*,a] = &\int_{-\beta/2}^{\beta/2} d\tau \sum_i \left\{ a_i^*(\tau) \left(\frac{\partial}{\partial \tau} - \mu \right) a_i(\tau) + \frac{U}{2} a_i^*(\tau) a_i^*(\tau) a_i(\tau) a_i(\tau) \right\} \\ &- J \int_{-\beta/2}^{\beta/2} d\tau \sum_{\langle i,j \rangle} \left\{ a_i^*(\tau) a_j(\tau) + a_j^*(\tau) a_i(\tau) \right\}. \end{aligned} \tag{2.26}$$

The complex field $a_i(\tau)$ depends on the imaginary time $\tau \in [-\beta/2, \beta/2]$ and represents the fluctuations of the lattice Bose field. Moreover, $\beta = (k_{\rm B}T)^{-1}$ denotes the inverse temperature. Throughout this subsection, we set $\hbar = 1$ for simplicity.

Suppose that the system is in a superfluid phase near the Mott-insulator transition. Let us derive an effective action characterizing the low-energy collective behaviors of the superfluid phase (for details, see Ref. [36]). As a first step, we take a Hubbard–Stratonovich transformation with a complex axillary field Ψ_i, which corresponds to the superfluid order parameter. Then, we integrate out the original Bose fields and define the action for the remaining axillary fields:

$$\begin{aligned} \Xi &= \int \mathcal{D}a^* \mathcal{D}a \mathcal{D}\Psi^* \mathcal{D}\Psi \; e^{-S_{\rm BH}[a^*,a,\Psi^*,\Psi^*]} \\ &= \int \mathcal{D}\Psi^* \mathcal{D}\Psi \; e^{-\tilde{S}[\Psi^*,\Psi^*]}, \end{aligned} \tag{2.27}$$

where $\tilde{S}[\Psi^*, \Psi^*]$ is in general a complicated functional of its arguments. Performing the expansion of $\tilde{S}[\Psi^*, \Psi^*]$ with respect to Ψ_i up to the forth order and taking a continuous limit, we obtain

$$\Xi \approx \int \mathcal{D}\psi^* \mathcal{D}\psi e^{-S_{\text{eff}}[\psi^*, \psi]}, \tag{2.28}$$

where $\psi(\tau, \mathbf{x})$ is a rescaled field introduced as $\psi = \Psi(d_{\text{lat}}^{d/2} z J)^{-1}$ [36]. The effective action $S_{\text{eff}}[\psi^*, \psi]$ describing the superfluid order parameter is given as follows:

$$S_{\text{eff}} = \beta F_0 + \int d\tau \int d^d x \left\{ K_1 \psi^* \frac{\partial}{\partial \tau} \psi + K_2 \left| \frac{\partial}{\partial \tau} \psi \right|^2 + \frac{1}{2m_*} |\nabla \psi|^2 + r|\psi|^2 + \frac{u}{2} |\psi|^4 \right\}, \tag{2.29}$$

where F_0 is the thermodynamic free-energy density in the imaginary-time axis. The coefficients K_1, K_2, m_*, r, and u are functions of the microscopic parameters of the Bose–Hubbard model. The explicit forms are found in Ref. [36].

The static part of the total effective action, which has no dynamical terms with K_1 and K_2, characterizes the ground state configuration of the order parameter within the saddle-point approximation. When the system is supposed to take a spatially uniform ground state, the following configuration of the order parameter amplitude is found to minimize the static part of the effective action for $r < 0$ or $r > 0$:

$$|\psi| = \begin{cases} \sqrt{-\frac{r}{u}} & (r < 0) \\ 0 & (r > 0) \end{cases}. \tag{2.30}$$

Thus, $r < 0$ ($r > 0$) corresponds to the order (disorder) phase at zero temperature, and the value $r = 0$ gives the phase boundary separating different phases.

It is important to emphasize that K_1 and K_2 should satisfy the following relations [19, 36]:

$$K_1 = -\frac{\partial r}{\partial \mu}, \quad K_2 = \frac{1}{2} \frac{\partial K_1}{\partial \mu}. \tag{2.31}$$

These follow from the invariance of the effective action with respect to the U(1) gauge transformation such that $\psi \to \psi e^{i\phi}$ and $\mu \to \mu + i \frac{\partial \phi}{\partial \tau}$. In particular, the former one implies that K_1 vanishes at the tip of the Mott lobe, at which the atomic density is commensurate. There, the effective action acquires an effective Lorentz invariance: it is invariant with respect to the complex-conjugated pair replacement of the field $\psi \to \psi^*$. This is nothing else but the origin of the dynamical critical exponent $z_{\text{dyn}} = 1$ near the Mott-insulator transition at commensurate densities. Due to such a characteristic property, the superfluid near the Mott-insulator transition can exhibit emergent-relativistic dynamics of the order parameter, such as the Higgs mode (see the next section) [32].

2.4 Higgs and Nambu–Goldstone Modes

Let us consider real-time dynamics of the commensurate superfluid near the Mott-insulator transition. Our starting point is the analytically-continued effective action of Eq. (2.29) at $K_1 = 0$ [37], which is given by

$$\mathcal{S}_{\rm eff} = \int dt \int d^d x \left\{ -K_2 \left| \frac{\partial}{\partial t}\psi \right|^2 + \frac{1}{2m_*}|\nabla\psi|^2 + r|\psi|^2 + \frac{u}{2}|\psi|^4 \right\}, \tag{2.32}$$

where t represents the real-time axis. Setting $\delta\mathcal{S}_{\rm eff}/\delta\psi^* = \delta\mathcal{S}_{\rm eff}/\delta\psi = 0$, we obtain the relativistic non-linear Klein–Gordon equation describing the saddle-point dynamics of the order parameter:

$$K_2\ddot{\psi} - \frac{1}{2m_*}\nabla^2\psi + r\psi + u\psi|\psi|^2 = 0. \tag{2.33}$$

Unlike the non-relativistic Gross–Pitaevskii equation, this equation has the second-order time-derivative term reflecting the relativistic nature of the effective action.

To describe low-energy collective fluctuations of the order parameter, let us linearize the Klein–Gordon equation with respect to a small fluctuation around the equilibrium configuration $\psi = \psi_{\rm eq} = \sqrt{-r/u}$ [cf. Eq. (2.30)]:

$$\psi(t) = \psi_{\rm eq} + \mathcal{U}e^{i\mathbf{p}\cdot\mathbf{r}-i\omega t} - \mathcal{V}e^{-i\mathbf{p}\cdot\mathbf{r}+i\omega t}, \tag{2.34}$$

where $\mathcal{U}$ and $\mathcal{V}$ are small amplitudes, and $\mathbf{p}$ and ω are the momentum and frequency of the fluctuation, respectively. Notice that $\mathcal{U}-\mathcal{V}$ corresponds to an amplitude fluctuation of the order parameter while $\mathcal{U}+\mathcal{V}$ does to a phase fluctuation of that. Substituting this into Eq. (2.33) and neglecting the high-order contributions, we find that there are two orthogonal eigenmodes corresponding to the amplitude and phase oscillations. The corresponding eigenfrequencies are calculated as follows:

$$\omega_{\rm higgs} = \sqrt{\Delta_{\rm higgs}^2 + c^2|\mathbf{p}|^2}, \quad \omega_{\rm ng} = c|\mathbf{p}|, \tag{2.35}$$

where $c^2 = (2m_*K_2)^{-1}$. The former dispersion $\omega_{\rm higgs}$ describes the amplitude fluctuation mode and opens an energy gap $\Delta_{\rm higgs} = \sqrt{-2r/K_2}$ if $r < 0$. This mode is referred to as the Higgs or amplitude mode [37]. On the other hand, the latter gapless dispersion $\omega_{\rm ng}$ characterizes the phase fluctuation mode of the order parameter. This is known as the Nambu–Goldstone (NG) or phase mode associated with restoring the U(1) symmetry [37]. The schematic picture of these modes is depicted in Fig. 2.2.

Such separation and orthogonality of the amplitude and phase fluctuations stem from the fact that they are no longer canonical conjugate with each other when the effective action has the relativistic Lorentz invariance. In other words, each component of fluctuations can have a certain momentum as a conjugate partner, inde-

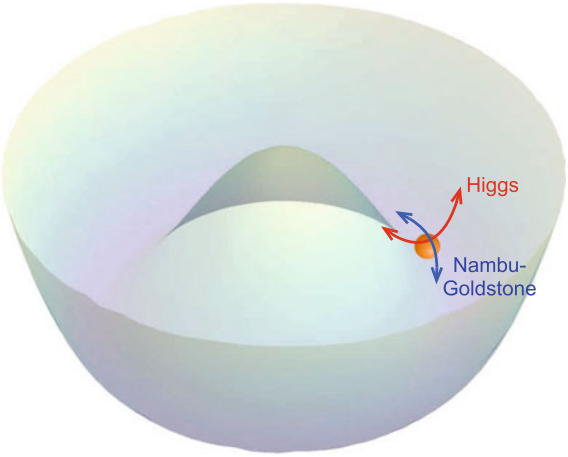

Fig. 2.2 Schematic picture of the Higgs and NG modes. The Higgs mode corresponds to an amplitude oscillation of the order parameter along the radial direction of the mexican-hat potential. On the other hand, the NG mode corresponds to a phase oscillating motion of that on the bottom of the potential along the azimuthal direction

pendently. The amplitude fluctuation and its conjugate momentum (not the phase fluctuation) form one collective mode, i.e., the gapped Higgs amplitude mode, which is independent of the phase fluctuation. In a similar way, the phase fluctuation and its conjugate momentum also form the gapless NG phase mode independently. This is in contrast to the non-relativistic Gross–Pitaevskii case, where the phase fluctuation is canonical conjugate with the amplitude one. In this case, these degrees of freedom form only one collective mode, namely the gapless Bogoliubov mode.

The Higgs mode can ubiquitously emerge in general thermodynamic phases with a particle-hole symmetry and spontaneous breaking of a continuous symmetry [37, 38]. This feature has attracted particular attention from many experimental research fields of condensed matter and ultracold gases [37]. The examples of quantum many-body systems, which can show the Higgs mode, include superconductors $NbSe_2$ [39–43] and $Nb_{1-x}Ti_xN$ [44–47], quantum antiferromagnets $TlCuCl_3$ [48, 49] and $KCuCl_3$ [50], charge density wave materials $K_{0.3}MoO_3$ [51, 52] and $TbTe_3$ [53, 54], superfluid ^{3}He B-phase [55, 56], two-component Fermi gases across the BCS-BEC crossover [57], and superfluid Bose gases in optical lattices [58, 59]. Moreover, the Higgs mode can be regarded as a counterpart of the Higgs boson in the standard theory of high energy physics [60].

Within the linear approximation, the Higgs and NG modes can be defined as decoupled eigenmodes of the order parameter dynamics. However, in more realistic situations, these modes can attain intrinsic damping rates because there are non-negligible interactions between them due to the non-linearity of the original model. Indeed, the Higgs mode can attenuate into two NG modes, and the damping property affects its visibility in experimental probes [32, 61, 62]. The damping rate of the Higgs mode arises from a virtual transition mediated by such Higgs-NG interactions. In a perturbative picture of the field-theoretical language, it can be interpreted as a loop correction to the eigenenergy of the Higgs mode, which shows up due to quantum and thermal fluctuations [61, 62].

2.5 Hilbert-Space Truncation and Effective Pseudospin-1 Models

In this section, we focus on an effective and microscopic description of the strongly-interacting regime of the Bose–Hubbard model for $U/J \gg 1$. For the purpose, it is convenient to modify our notation of the Bose–Hubbard model (2.20) as follows:

$$\hat{\mathcal{H}}_{\mathrm{BH}} = -J \sum_{\langle ij \rangle} \hat{a}_i^\dagger \hat{a}_j + \frac{U}{2} \sum_i (\hat{n}_i - n_0)^2 - \sum_i \mu(\hat{n}_i - n_0),$$

where $n_i = \hat{a}_i^\dagger \hat{a}_i$ is the density operator at site i and n_0 is the commensurate filling factor. The difference from the previous definition is the origin of measuring the chemical potential.

This section is organized as follows: In Sect. 2.5.1, we introduce a reduced local Hilbert space to define a strongly-correlated effective model and a pseudospin representation of physical operators in the projected space based on the Schwinger-boson theory. In Sect. 2.5.2, we derive an effective model for a large-filling limit and discuss its intrinsic property, i.e., an effective particle-hole symmetry. In Sect. 2.5.3, we generalize the large-filling effective model into low-filling cases, which correspond to typical setups in ultracold-gas experiments. In Sect. 2.5.4, we discuss the ground state property of the effective model within a Gutzwiller mean-field ansatz. Finally, in Sect. 2.5.5, especially at a high-filling limit, we derive mean-field dispersion relations of elementary excitations inside the superfluid and Mott-insulator phases, respectively.

2.5.1 Reduced Hilbert Space in Strongly-Correlated Regimes

Let us assume that the system contains an integer number of particles with $\langle \hat{n}_i \rangle = n_0$. At a sufficiently large interaction compared with the hopping amplitude, local fluctuations of $\hat{n}_i$ from the mean density are strongly suppressed. Therefore, low-energy properties of the system can be described by an effective model

$$\hat{\mathcal{H}}_{\mathrm{eff}}^{n_0} = \mathcal{P}_{n_0} \hat{\mathcal{H}}_{\mathrm{BH}} \mathcal{P}_{n_0}^{-1}, \tag{2.36}$$

where $\mathcal{P}_{n_0}$ is a projection operator eliminating high-energy Fock states $|n_0 + \alpha\rangle$ for $|\alpha| > 1$ from the complete Hilbert space. The remaining states, which effectively describe the low-energy phenomena, can be represented by three Schwinger bosons [32, 33, 62, 63],

$$|n_0 + 1\rangle_j \equiv \hat{t}_{1,j}^\dagger |\mathrm{vac}\rangle, \quad |n_0\rangle_j \equiv \hat{t}_{0,j}^\dagger |\mathrm{vac}\rangle, \quad |n_0 - 1\rangle_j \equiv \hat{t}_{-1,j}^\dagger |\mathrm{vac}\rangle, \tag{2.37}$$

where $|\mathrm{vac}\rangle$ is the vacuum of new bosons. The new bosons fulfill the commutation relations

$$[\hat{t}_{\alpha,i}, \hat{t}^{\dagger}_{\alpha',j}] = \delta_{\alpha,\alpha'}\delta_{i,j}, \quad [\hat{t}_{\alpha,i}, \hat{t}_{\alpha',j}] = [\hat{t}^{\dagger}_{\alpha,i}, \hat{t}^{\dagger}_{\alpha',j}] = 0. \tag{2.38}$$

In order to eliminate the unphysical states such as $\hat{t}^{\dagger}_{1,i}\hat{t}^{\dagger}_{0,i}|\mathrm{vac}\rangle$, we assume that these operators obey a local holonomic constraint

$$\sum_{\alpha=-1}^{1} \hat{t}^{\dagger}_{\alpha,i}\hat{t}_{\alpha,i} = \hat{1}, \tag{2.39}$$

where $\hat{1}$ on the righthand side is the identity operator in the reduced Hilbert subspace.

In the projected Hilbert space, each of local operator that constitutes the model Hamiltonian, $\hat{a}_i$, $\hat{a}^{\dagger}_i$, and $\delta\hat{n}_i = \hat{n}_i - n_0$, reduces to a simple form represented by the constrained Schwinger bosons $\hat{t}_{\alpha}$, $\hat{t}^{\dagger}_{\alpha}$ ($\alpha = -1, 0, 1$). In terms of the bosons, the operators read

$$\begin{aligned}
\mathcal{P}_{n_0}\hat{a}^{\dagger}_i\mathcal{P}^{-1}_{n_0} &= \sqrt{n_0+1}\hat{t}^{\dagger}_{1,i}\hat{t}_{0,i} + \sqrt{n_0}\hat{t}^{\dagger}_{0,i}\hat{t}_{-1,i}, \\
\mathcal{P}_{n_0}\hat{a}_i\mathcal{P}^{-1}_{n_0} &= \sqrt{n_0+1}\hat{t}^{\dagger}_{0,i}\hat{t}_{1,i} + \sqrt{n_0}\hat{t}^{\dagger}_{-1,i}\hat{t}_{0,i}, \\
\mathcal{P}_{n_0}\delta\hat{n}_i\mathcal{P}^{-1}_{n_0} &= \hat{t}^{\dagger}_{1,i}\hat{t}_{1,i} - \hat{t}^{\dagger}_{-1,i}\hat{t}_{-1,i}.
\end{aligned}$$

Here, let us introduce pseudospin-1 operators of the Schwinger bosons, which are defined by

$$\hat{S}^{+}_i = \sqrt{2}(\hat{t}^{\dagger}_{1,i}\hat{t}_{0,i} + \hat{t}^{\dagger}_{0,i}\hat{t}_{-1,i}), \quad \hat{S}^{-}_i = \sqrt{2}(\hat{t}^{\dagger}_{0,i}\hat{t}_{1,i} + \hat{t}^{\dagger}_{-1,i}\hat{t}_{0,i}), \quad \hat{S}^{z}_i = \hat{t}^{\dagger}_{1,i}\hat{t}_{1,i} - \hat{t}^{\dagger}_{-1,i}\hat{t}_{-1,i}. \tag{2.40}$$

It is easy to see that these operators satisfy the standard SU(2) commutation relations such that

$$[\hat{S}^{+}_i, \hat{S}^{-}_j] = 2\hat{S}^{z}_i\delta_{i,j}, \quad [\hat{S}^{z}_i, \hat{S}^{\pm}_j] = \pm\hat{S}^{\pm}_i\delta_{i,j}. \tag{2.41}$$

In addition, there exists a conserved Casimir operator, which commutes all of the ingredients of the algebra, such that $\sum_{\alpha=x,y,z}(\hat{S}^{\alpha}_j)^2 = 2 \equiv S(S+1)$, where $\hat{S}^{\pm}_j = \hat{S}^{x}_j \pm i\hat{S}^{y}_j$. Using the pseudospin representation, we obtain

$$\begin{aligned}
\mathcal{P}_{n_0}\hat{a}^{\dagger}_i\mathcal{P}^{-1}_{n_0} &= \sqrt{\frac{n_0}{2}}(1 + \delta\nu\hat{S}^{z}_i)\hat{S}^{+}_i, \\
\mathcal{P}_{n_0}\hat{a}_i\mathcal{P}^{-1}_{n_0} &= \sqrt{\frac{n_0}{2}}\hat{S}^{-}_i(1 + \delta\nu\hat{S}^{z}_i), \\
\mathcal{P}_{n_0}\delta\hat{n}_i\mathcal{P}^{-1}_{n_0} &= \hat{S}^{z}_i,
\end{aligned} \tag{2.42}$$

where $\delta\nu = \sqrt{1+1/n_0} - 1$. The results of the first and second equations have an explicit dependence on the projection center n_0. On the other hand, the righthand side of the final equation does not depend on n_0, so that it has the same form for any n_0.

2.5.2 *Effective Pseudospin-1 Model at a High-Filling Limit*

Applying the mapping formula (2.42), let us derive an explicit form of the strongly-interacting effective model at a large-occupation limit [32]. At $n_0 \gg 1$, the difference between $\sqrt{n_0+1}$ and $\sqrt{n_0}$ vanishes and $\delta\nu$ approaches to zero. In this limit, the creation and annihilation operators of the original bosons are effectively written in the form

$$\mathcal{P}_{n_0}\hat{a}_i^\dagger\mathcal{P}_{n_0}^{-1} \approx \sqrt{\frac{n_0}{2}}\hat{S}_i^+, \quad \mathcal{P}_{n_0}\hat{a}_i\mathcal{P}_{n_0}^{-1} \approx \sqrt{\frac{n_0}{2}}\hat{S}_i^-. \tag{2.43}$$

Substituting these results into Eq. (2.36), we obtain an effective pseudospin-1 model [32],

$$\hat{\mathcal{H}}_{\rm eff}^{n_0\gg 1} = -\frac{Jn_0}{2}\sum_{\langle ij\rangle}\hat{S}_i^+\hat{S}_j^- + \frac{U}{2}\sum_i(\hat{S}_i^z)^2 - B\sum_i\hat{S}_i^z, \tag{2.44}$$

where $B = \mu$ is the uniform *magnetic field* coupling with the z-component of the pseudospins. The XY spin exchange, on-site single-ion anisotropy, and magnetic coupling terms correspond to the hopping, onsite-interaction, and chemical potential terms in the original Bose–Hubbard model, respectively.

The effective model (2.44) was first obtained by Altman and Auerbach in 2002 [32]. They used this model to investigate dynamical properties of superfluid Bose gases with a large occupation, especially, oscillations of the superfluid order parameter in the vicinity of the Mott-insulator transition [32]. Furthermore, this model has been utilized for examining universal aspects of adiabatic-limit dynamics near a quantum phase transition [64], estimating damping rates of the Higgs and NG modes at finite temperatures and in three dimensions [62], and discussing the applicability of the SU(3) truncated-Wigner approximation to ultracold gas systems [65].

An important feature of Eq. (2.44) is its explicit particle-hole symmetry at commensurate filling, which corresponds to $B = \mu = 0$. In the Schwinger-boson language, this symmetry can be viewed as an invariance associated with an exchange between $\hat{t}_1$ (particle) and $\hat{t}_{-1}$ (hole). In Sect. 2.5.5, we will derive an energy dispersion of elementary excitations around a mean-field ground state using a Holstein–Primakoff expansion of the Schwinger bosons. There, we will see that the Higgs and NG branches are completely decoupled at a quadratic level due to the

particle-hole symmetry. Furthermore, such an explicit symmetry forbids interactions associated with an odd number of the NG mode. It is worth noting that the relativistic Klein–Gordon-type effective action can be derived through the spin-coherent-state path-integral representation of the effective pseudospin-1 model at $B = 0$ [32].

2.5.3 *Effective Pseudospin-1 Model at Low-Filling Rates*

The high-filling model (2.44) does not correspond to typical experimental situations, in which the filling factor is tuned to unity (see, e.g., Ref. [59]). For lower commensurate filling rates ($n_0 \sim 1$), we need to modify the spin exchange term [33] such that

$$\mathcal{H}_{\rm eff}^{n_0} = -\frac{Jn_0}{2}\sum_{\langle ij\rangle}(1+\delta\nu S_i^z)S_i^+S_j^-(1+\delta\nu S_j^z) + \frac{U}{2}\sum_i (S_i^z)^2 - B\sum_i S_i^z. \quad (2.45)$$

The modified model (2.45) has no longer the explicit particle-hole symmetry seen in the high-filling model even at commensurate filling rates. Note that $\delta\nu$ measures the deviation from the particle-hole symmetric point. In fact, when we make a limit $\delta\nu \to 0$, the modified effective model results in the particle-hole symmetric model (2.44). The correction terms at low-filling rates were first discussed by Huber et al. [33].

In Chap. 4, we use the low-filling effective model (2.45) to analyze some response functions in the 3D Bose–Hubbard model at unit filling. Despite the absence of the particle-hole symmetry at the microscopic level, Eq. (2.45) is able to exhibit two independent collective excitations, i.e., the Higgs and NG modes, within the quadratic approximation of the Holstein–Primakoff expansion. This can be interpreted as that the system attains an emergent particle-hole symmetry near the Mott-insulator transition.

2.5.4 *Gutzwiller's Variational Ansatz in the Reduced Hilbert Space*

Let us discuss the ground state of the projected effective model (2.45) within mean-field approximation. To do that, we use Gutzwiller's variational ansatz according to Refs. [32, 33]. Our starting point is to define a variational wave function spanned in the reduced Hilbert space [32, 33]:

$$|\Omega(\theta,\eta,\varphi,\chi)\rangle = \prod_i \left\{ \cos\left(\frac{\theta}{2}\right)\hat{t}^\dagger_{0,i} + e^{i\eta}\sin\left(\frac{\theta}{2}\right)\left[e^{i\varphi}\sin\left(\frac{\chi}{2}\right)\hat{t}^\dagger_{1,i} + e^{-i\varphi}\cos\left(\frac{\chi}{2}\right)\hat{t}^\dagger_{-1,i}\right]\right\}|\mathrm{vac}\rangle, \tag{2.46}$$

where $\theta \in [0,\pi]$, $\eta \in [-\pi/2,\pi/2]$, $\varphi \in [0,2\pi]$, and $\chi \in [0,\pi]$ are the variational parameters. We note that this wave function at $\theta = 0$ describes the Mott-insulating state of n_0 filling factor with no fluctuation, i.e. $\prod_i \hat{t}^\dagger_{0,i}|\mathrm{vac}\rangle$. In the superfluid phase, $\theta \neq 0$ mixes the mean filling state $\hat{t}^\dagger_{0,i}$ with the particle and hole fluctuations $\hat{t}^\dagger_{1,i}$ and $\hat{t}^\dagger_{-1,i}$. Hence, it plays a role of the order parameter strength.

In the superfluid phase ($\theta \neq 0$), the variational parameters are determined from minimizing the mean energy density $E^{\mathrm{MF}} = \langle\Omega|\mathcal{H}^{n_0}_{\mathrm{eff}}|\Omega\rangle/M$ with respect to the variational parameters. Here, M is the total number of the lattice point. The explicit form can be computed as

$$E^{\mathrm{MF}} = \left[\frac{1}{2} + \mu\cos\chi\right]\sin^2\left(\frac{\theta}{2}\right) - \frac{Jz}{4}\sin^2\theta\left[n_0 + \sin^2\left(\frac{\chi}{2}\right) + \sqrt{n_0(1+n_0)}\sin\chi\cos 2\eta\right]. \tag{2.47}$$

After effecting the variation of Eq. (2.47) with respect to the variational parameters, we obtain a mean-field ground-state energy $E_0(\theta_{\mathrm{mf}}) = E^{\mathrm{MF}}[\theta_{\mathrm{mf}},0,0,\chi(\theta_{\mathrm{mf}})]$ where

$$\tan\chi(\theta) = -\frac{2Jz\sqrt{n_0(n_0+1)}[1-\sin^2(\theta/2)]}{2\mu + Jz[1-\sin^2(\theta/2)]}, \tag{2.48}$$

and θ_{mf} is determined such that it minimizes the function $E_0(\theta)$. Using the optimized wave function after the variation, we also obtain the order parameter $\Psi = \langle\Omega|a_i|\Omega\rangle$ and mean density $\bar{n} = \langle\Omega|n_i|\Omega\rangle$ of the ground state as follows:

$$\Psi = \frac{1}{2}\sin\theta_{\mathrm{mf}}\left[\sqrt{n_0+1}\sin\left(\frac{\chi_{\mathrm{mf}}}{2}\right) + \sqrt{n_0}\cos\left(\frac{\chi_{\mathrm{mf}}}{2}\right)\right], \tag{2.49}$$

$$\bar{n} = n_0 - \sin^2\left(\frac{\theta_{\mathrm{mf}}}{2}\right)\cos\chi_{\mathrm{mf}}, \tag{2.50}$$

$$\chi_{\mathrm{mf}} = \chi(\theta_{\mathrm{mf}}). \tag{2.51}$$

It is easy to obtain an analytical form of θ_{mf} at commensurate filling rates. In this case, χ_{mf} turns out to be $\chi_{\mathrm{mf}} = \pi/2$ [see Eq. (2.51)]. Minimizing $E^{\mathrm{MF}}(\theta,0,0,\pi/2)$ with respect to θ, we obtain

$$\theta_{\mathrm{mf}} = \sin^{-1}\left(\sqrt{1-(Jz)^{-2}(\sqrt{n_0+1}+\sqrt{n_0})^{-4}}\right), \tag{2.52}$$

and the corresponding chemical potential at $\bar{n} = n_0$ reads

$$\mu_{n_0} = -\frac{1}{4}\left[zJ + (\sqrt{n_0+1} + \sqrt{n_0})^{-2}\right]. \tag{2.53}$$

Furthermore, it is worth noting that at $\chi_{\mathrm{mf}} = \pi/2$ the ground state is particle-hole symmetric. This is because the corresponding wave function (2.46) contains $t^{\dagger}_{1,i}$ and $t^{\dagger}_{-1,i}$ components with equal weights at each site.

From the Ginzburg–Landau expansion of E^{MF} of the ground state with respect to the order parameter $\Psi = \langle\Omega|a_i|\Omega\rangle$, we can determine the phase-boundary of the superfluid to insulator transition [33]. Now we introduce a dimensionless parameter $u = U/(4Jn_0z)$ measuring the distance from the critical point at the commensurate filling rate. The critical value of the superfluid to insulator transition within the mean-field approximation [33] is

$$u_c = \frac{1}{4n_0}(\sqrt{n_0+1} + \sqrt{n_0})^2. \tag{2.54}$$

In the limit of $n_0 \to \infty$, the critical value u_c approaches 1. At the unit filling rate $n_0 = 1$, $u_c = (\sqrt{2}+1)^2/4 \approx 1.457$. The same result has been obtained from the decoupling approximation for the Bose–Hubbard model (see Sect. 2.3.1). The exact critical value at the unit filling rate has been numerically computed as $u_c = 1.22(2)$ by the quantum Monte-Carlo method for the 3D Bose–Hubbard model in Ref. [22]. In Chap. 4, we mainly use the mean-field result of Eq. (2.54) to be consistent with our analysis on the mean-field ground state.

2.5.5 *Elementary Excitations Around the Gutzwiller Wave Function*

Using the effective pseudospin-1 model and Gutzwiller's wave function, we discuss elementary excitations around the Mott-insulator and superfluid states, respectively. For simplicity, we focus on the high-filling limit where the calculation is simple due to the particle-hole symmetry of the effective model. The low-filling generalization will be presented in Chap. 4 because it is closely related with our main analysis of this Thesis. In this subsection, we assume the commensurate case $B = 0$ in order to discuss the Higgs and NG modes. The following discussion is basically a review of Ref. [32].

To obtain the energy dispersion of elementary excitations in the superfluid phase (i.e., the amplitude and phase fluctuations), let us introduce a creation operator of the mean-field ground state $|\Omega\rangle \equiv \prod_i \hat{b}^{\dagger}_{0,i}|\mathrm{vac}\rangle$ and define a canonical transformation

$$\begin{aligned}\hat{b}^{\dagger}_{0,i} &= c_1\hat{t}^{\dagger}_{0,i} + s_1\left[s_2\hat{t}^{\dagger}_{1,i} + c_2\hat{t}^{\dagger}_{-1,i}\right],\\ \hat{b}^{\dagger}_{1,i} &= s_1\hat{t}^{\dagger}_{0,i} - c_1\left[s_2\hat{t}^{\dagger}_{1,i} + c_2\hat{t}^{\dagger}_{-1,i}\right],\\ \hat{b}^{\dagger}_{2,i} &= c_2\hat{t}^{\dagger}_{1,i} - s_2\hat{t}^{\dagger}_{-1,i},\end{aligned} \tag{2.55}$$

where the coefficients are $s_1 = \sin(\theta_{\rm mf}/2)$, $c_1 = \cos(\theta_{\rm mf}/2)$, $s_2 = \sin[\chi(\theta_{\rm mf})/2]$, and $c_2 = \cos[\chi(\theta_{\rm mf})/2]$. $\theta_{\rm mf}(\neq 0)$ denotes the optimal value of θ for the ground state. $\hat{b}^{\dagger}_{1,i}$ describes the amplitude fluctuation of the order parameter on the ground state while $\hat{b}^{\dagger}_{2,i}$ describes the phase fluctuation. These new operators fulfill the same commutation relations as the old operators $\hat{t}_{\alpha,i}$. In addition, the transformation retains the constraint (2.39) such that

$$\sum_{m=0}^{2}\hat{b}^{\dagger}_{m,i}\hat{b}_{m,i} = \hat{1}. \tag{2.56}$$

As a next step, we simplify the effective model by means of the Holstein–Primakoff (HP) expansion [63, 66]. Since the mean-field ground state can be regarded as a Bose–Einstein condensate of the constrained boson $\hat{b}_{0,i}$, we can eliminate $\hat{b}_{0,i}$ by an expansion with respect to the fluctuations (*spin waves*) $\hat{b}_{1,i}$ and $\hat{b}_{2,i}$:

$$\begin{aligned}\hat{b}^{\dagger}_{m,i}\hat{b}_{0,j} &= \hat{b}^{\dagger}_{m,i}\sqrt{1-\hat{b}^{\dagger}_{1,j}\hat{b}_{1,j}-\hat{b}^{\dagger}_{2,j}\hat{b}_{2,j}},\\ &\approx \hat{b}^{\dagger}_{m,i} - \frac{1}{2}\hat{b}^{\dagger}_{m,i}\hat{b}^{\dagger}_{1,j}\hat{b}_{1,j} - \frac{1}{2}\hat{b}^{\dagger}_{m,i}\hat{b}^{\dagger}_{2,j}\hat{b}_{2,j} + \cdots.\end{aligned} \tag{2.57}$$

When the expansion is stopped up to quadratic order, we obtain a free Hamiltonian, which describes the excitations within the non-interacting limit. Interaction or nonlinear effects beyond the quadratic order approximation will be discussed in Chap. 4.

The quadratic Hamiltonian is diagonalized through the standard Bogoliubov transformation [67]. In the high-filling limit, where the effective model has the explicit particle-hole symmetry, the transformation can be carried out independently in each branch because the amplitude and phase sectors are completely decoupled from each other. Notice that the HP expansion gives rise to no violation of such a symmetry. We rotate the operator basis by using a canonical transformation defined by

$$\begin{aligned}\hat{b}_{m,\mathbf{k}} &= u_{m,\mathbf{k}}\hat{\beta}_{m,\mathbf{k}} + v^{*}_{m,-\mathbf{k}}\hat{\beta}^{\dagger}_{m,-\mathbf{k}},\\ \hat{b}^{\dagger}_{m,\mathbf{k}} &= u^{*}_{m,-\mathbf{k}}\hat{\beta}^{\dagger}_{m,-\mathbf{k}} + v_{m,\mathbf{k}}\hat{\beta}_{m,\mathbf{k}},\end{aligned} \tag{2.58}$$

where $m \in \{1, 2\}$. Here we have introduced the Fourier transformation of the fluctuation operators $\hat{b}_{1,i}$ and $\hat{b}_{2,i}$,

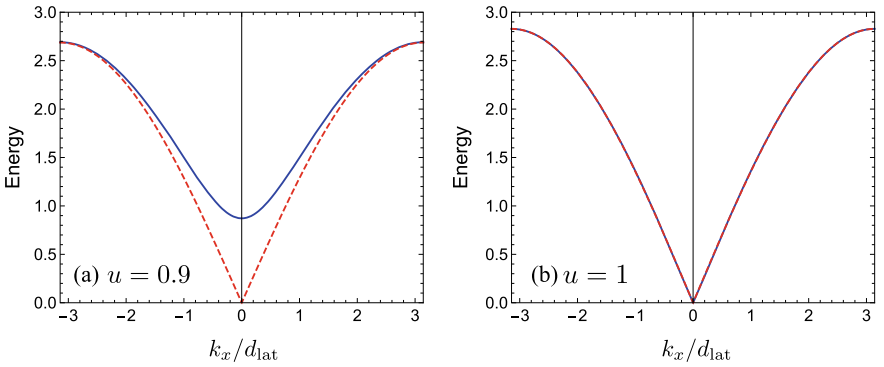

Fig. 2.3 Higgs (blue-solid) and NG (red-dashed) energy dispersions at the high-filling limit. The vertical axis represents the energy dispersions ($Jn_0z = 1$), whereas the horizontal axis does the wave-number vector in one dimension ($d_{\rm lat} = 1$). Two different results are calculated at **a** $u = 0.9$ and **b** $u = 1$, respectively

$$\hat{b}^\dagger_{m,i} = \frac{1}{\sqrt{M}} \sum_{\mathbf{k}\in\Lambda_0} \hat{b}^\dagger_{m,\mathbf{k}} e^{-\mathrm{i}\mathbf{k}\cdot\mathbf{r}_i}, \quad \hat{b}_{m,i} = \frac{1}{\sqrt{M}} \sum_{\mathbf{k}\in\Lambda_0} \hat{b}_{m,\mathbf{k}} e^{\mathrm{i}\mathbf{k}\cdot\mathbf{r}_i}.$$

The notation $\sum_{\mathbf{k}\in\Lambda_0}$ denotes that the momentum $\mathbf{k}$ runs over the cubic-shaped first Brillouin zone $\Lambda_0 \equiv [-\pi, \pi]^3$. The free coefficients of rotation, $u_{m,\mathbf{k}}$ and $v_{m,\mathbf{k}}$, should satisfy a condition $|u_{m,\mathbf{k}}|^2 - |v_{m,\mathbf{k}}|^2 = 1$. Then, the new operator $\hat{\beta}_{m,\mathbf{k}}$ fulfills the canonical commutation relation $[\hat{\beta}_{m,\mathbf{k}}, \hat{\beta}^\dagger_{m',\mathbf{k}'}] = \delta_{m,m'}\delta_{\mathbf{k},\mathbf{k}'}$. When we choose the coefficients such that

$$u_{1,\mathbf{k}} = \sqrt{\frac{2-u^2\gamma_\mathbf{k}}{4\sqrt{1-u^2\gamma_\mathbf{k}}} + \frac{1}{2}}, \quad v_{1,\mathbf{k}} = \mathrm{sgn}(\gamma_\mathbf{k})\sqrt{\frac{2-u^2\gamma_\mathbf{k}}{4\sqrt{1-u^2\gamma_\mathbf{k}}} - \frac{1}{2}}, \tag{2.59}$$

$$u_{2,\mathbf{k}} = \sqrt{\frac{2-\gamma_\mathbf{k}}{4\sqrt{1-\gamma_\mathbf{k}}} + \frac{1}{2}}, \quad v_{2,\mathbf{k}} = -\mathrm{sgn}(\gamma_\mathbf{k})\sqrt{\frac{2-\gamma_\mathbf{k}}{4\sqrt{1-\gamma_\mathbf{k}}} - \frac{1}{2}}, \tag{2.60}$$

where $\mathrm{sgn}(x)$ is the sign function, then the quadratic Hamiltonian reads a diagonalized form

$$\hat{\mathcal{H}}^{n_0\gg1}_{\rm eff} \approx \text{const.} + \sum_{m=1,2}\sum_{\mathbf{k}\in\Lambda_0} \mathcal{E}_{m,\mathbf{k}} \hat{\beta}^\dagger_{m,\mathbf{k}} \hat{\beta}_{m,\mathbf{k}}. \tag{2.61}$$

The band dispersions $\mathcal{E}_{1,\mathbf{k}}$ (Higgs) and $\mathcal{E}_{2,\mathbf{k}}$ (NG) are given by

$$\mathcal{E}_{1,\mathbf{k}} = 2Jn_0z\sqrt{1-u^2\gamma_\mathbf{k}}, \quad \mathcal{E}_{2,\mathbf{k}} = Jn_0z(1+u)\sqrt{1-\gamma_\mathbf{k}}, \tag{2.62}$$

where $\gamma_\mathbf{k} = \sum_{i=1}^d \cos(k_i d_{\rm lat})/d$. Figure 2.3 depicts the energy dispersions as a function of $\mathbf{k}$ in one dimension ($d = 1$). As shown in Fig. 2.3a, the Higgs dispersion has

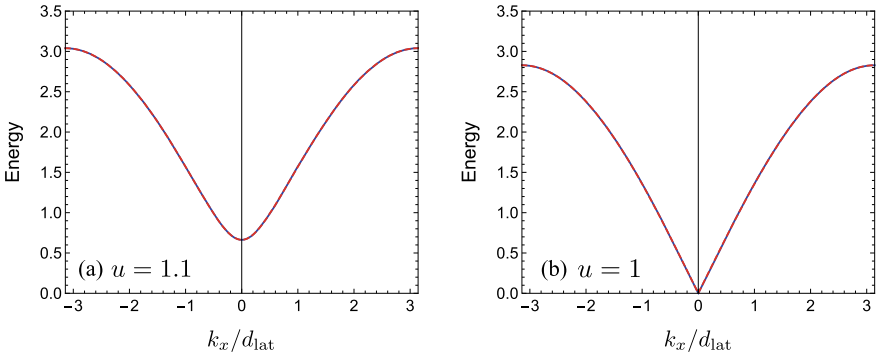

Fig. 2.4 Particle (blue-solid) and hole (red-dashed) energy dispersions at the high-filling limit. The vertical axis represents the energy dispersions ($Jn_0z = 1$), whereas the horizontal axis does the wave-number vector in one dimension ($d_{\rm lat} = 1$). Two different results are calculated at **a** $u = 1.1$ and **b** $u = 1$, respectively

a finite energy gap $\tilde{\Delta} = 2Jn_0z\sqrt{1-u^2}$ at $\mathbf{k} = 0$ (apart from $u = u_c = 1$) while the NG one is gapless at that point. Moreover, it is clearly seen that at the critical point $u = u_c = 1$, the energy gap $\tilde{\Delta}$ closes and these dispersions coincide with each other.

Similarly, we can derive the energy dispersion of the particle-hole excitations in the Mott-insulator state. To do that, we expand $\hat{t}_{0,i}$ in $\hat{t}_{1,i}$ and $\hat{t}_{-1,i}$ via the constraint $\sum_m \hat{t}_m^\dagger \hat{t}_m = \hat{1}$ within the quadratic order, i.e.,

$$\begin{aligned}\hat{t}_{0,i} &= \sqrt{1 - \hat{t}_{1,i}^\dagger \hat{t}_{1,i} - \hat{t}_{-1,i}^\dagger \hat{t}_{-1,i}} \\ &\approx 1 - \frac{1}{2}\hat{t}_{1,i}^\dagger \hat{t}_{1,i} - \frac{1}{2}\hat{t}_{-1,i}^\dagger \hat{t}_{-1,i} + \cdots . \end{aligned} \tag{2.63}$$

The diagonalization of the resulting quadratic Hamiltonian is also simple because the particle and hole sectors are completely decoupled from each other. After simple calculations on the basis of the Bogoliubov transformation, we finally arrive at the particle and hole dispersions [32], $\hbar\omega_p$ and $\hbar\omega_h$, which are written as

$$\hbar\omega_p = \hbar\omega_h = \frac{U}{2}\sqrt{1 - u^{-1}\gamma_{\mathbf{k}}}. \tag{2.64}$$

These dispersions have the entirely same form due to the commensurate filling ($B = 0$). In Fig. 2.4, we show $\hbar\omega_p$ and $\hbar\omega_h$ as a function of $\mathbf{k}$ in one dimension. For $u > u_c$, the excitation energies have a finite gap corresponding to the incompressibility of the Mott-insulator phase [Fig. 2.4a]. In contrast, the gap vanishes at $u = u_c = 1$ [Fig. 2.4b].

Within the quadratic approximation of the HP expansion, the Higgs and NG modes can be regarded as well-defined eigenstates because there is no transition among different levels. However, including further contributions of the expansion,

these modes are able to attenuate into other non-perturbed states with certain decay rates. The stability of the Higgs mode against quantum and thermal fluctuations mediated by the interactions is studied in Chap. 4. There, we apply the HP expansion to the high and low filling effective models, respectively, in order to analyze some response functions to external perturbations.

References

1. D. Jaksch, C. Bruder, J.I. Cirac, C.W. Gardiner, P. Zoller, Phys. Rev. Lett. **81**, 3108 (1998)
2. R. Grimm, M. Weidemüller, Y.B. Ovchinnikov, Adv. At. Mol. Opt. Phys. **42**, 95 (2000)
3. M. Greiner, Ultracold quantum gases in three-dimensional optical lattice potentials, Ph.D. thesis, Ludwig-Maximilians-Universität München (2003)
4. C.J. Pethick, H. Smith, *Bose-Einstein Condensation in Dilute Gases* (Cambridge University Press, Cambridge, 2008)
5. J. Sebby-Strabley, M. Anderlini, P.S. Jessen, J.V. Porto, Phys. Rev. A **73**, 033605 (2006)
6. G. Wirth, M. Olschlager, A. Hemmerich, Nat. Phys. **7**, 147 (2010)
7. P. Soltan-Panahi, J. Struck, P. Hauke, A. Bick, W. Plenkers, G. Meineke, C. Becker, P. Windpassinger, M. Lewenstein, K. Sengstock, Nat. Phys. **7**, 434 (2011)
8. C. Becker, P. Soltan-Panahi, J. Kronjäger, S. Dörscher, K. Bongs, K. Sengstock, New J. Phys. **12**, 065025 (2010)
9. J. Struck, C. Ölschläger, R.L. Targat, P. Soltan-Panahi, A. Eckardt, M. Lewenstein, P. Windpassinger, K. Sengstock, Science **333**, 996 (2011)
10. G.-B. Jo, J. Guzman, C.K. Thomas, P. Hosur, A. Vishwanath, D.M. Stamper-Kurn, Phys. Rev. Lett. **108**, 045305 (2012)
11. S. Taie, H. Ozawa, T. Ichinose, T. Nishio, S. Nakajima, Y. Takahashi, Sci. Adv. **1**, e1500854 (2015)
12. I. Bloch, J. Dalibard, W. Zwerger, Rev. Mod. Phys. **80**, 885 (2008)
13. M. Lewenstein, A. Sanpera, V. Ahufinger, *Ultracold Atoms in Optical Lattices: Simulating Quantum Many-Body Systems* (Oxford University Press, Oxford, 2012)
14. W. Hofstetter, T. Qin, J. Phys. B: At. Mol. Opt. Phys. **51**, 082001 (2018)
15. M. Ueda, *Fundamentals and New Frontiers of Bose-Einstein Condensation* (World Scientific, Singapore, 2010)
16. M.P.A. Fisher, P.B. Weichman, G. Grinstein, D.S. Fisher, Phys. Rev. B **40**, 546 (1989)
17. M. Greiner, O. Mandel, T. Esslinger, T.W. Hänsch, I. Bloch, Nature **415**, 39 (2002)
18. C. Chin, R. Grimm, P. Julienne, E. Tiesinga, Rev. Mod. Phys. **82**, 1225 (2010)
19. S. Sachdev, *Quantum Phase Transition*, 2nd edn. (Cambridge University Press, Cambridge, 2011)
20. D. van Oosten, P. van der Straten, H.T.C. Stoof, Phys. Rev. A **63**, 053601 (2001)
21. B. Capogrosso-Sansone, Ş.G. Söyler, N. Prokof'ev, B. Svistunov, Phys. Rev. A **77**, 015602 (2008)
22. B. Capogrosso-Sansone, N.V. Prokof'ev, B.V. Svistunov, Phys. Rev. B **75**, 134302 (2007)
23. N.D. Mermin, H. Wanger, Phys. Rev. Lett. **17**, 1133 (1966)
24. S. Coleman, Commun. Math. Phys. **31**, 259 (1973)
25. V.L. Berezinskii, Sov. Phys. JETP **32**, 493 (1970)
26. V.L. Berezinskii, Sov. Phys. JETP **34**, 601 (1971)
27. J.M. Kosterlitz, D.J. Thouless, J. Phys. C: Solid State Phys. **6**, 1181 (1973)
28. J.M. Kosterlitz, D.J. Thouless, J. Phys. C: Solid State Phys. **6**, 1046 (1974)
29. T. Giamarchi, *Quantum Physics in One Dimension* (Oxford University Press, New York, 2003)
30. D.S. Rokhsar, B.G. Kotliar, Phys. Rev. B **44**, 10328 (1991)
31. W. Krauth, M. Caffarel, J. Bouchaud, Phys. Rev. B **45**, 3137 (1992)

32. E. Altman, A. Auerbach, Phys. Rev. Lett. **89**, 250404 (2002)
33. S.D. Huber, E. Altman, H.P. Büchler, G. Blatter, Phys. Rev. B **75**, 085106 (2007)
34. T.D. Kühner, S.R. White, H. Monien, Phys. Rev. B **61**, 12474 (2000)
35. N. Teichmann, D. Hinrichs, M. Holthaus, A. Eckardt, Phys. Rev. B **79**, 100503(R) (2009)
36. T. Nakayama, I. Danshita, T. Nikuni, S. Tsuchiya, Phys. Rev. A **92**, 043610 (2015)
37. D. Pekker, C.M. Varma, Annu. Rev. Condens. Matter Phys. **6**, 269 (2015)
38. G.E. Volovik, M.A. Zubkov, J. Low Temp. Phys. **175**, 486 (2014)
39. R. Sooryakumar, M.V. Klein, Phys. Rev. Lett. **45**, 660 (1980)
40. R. Sooryakumar, M.V. Klein, Phys. Rev. B **23**, 3213 (1981)
41. P.B. Littlewood, C.M. Varma, Phys. Rev. Lett. **47**, 811 (1981)
42. P.B. Littlewood, C.M. Varma, Phys. Rev. B **26**, 4883 (1982)
43. M.-A. Méasson, Y. Gallais, M. Cazayous, B. Clair, P. Rodiére, L. Cario, A. Sacuto, Phys. Rev. B **89**, 060503 (2014)
44. R. Matsunaga, Y.I. Hamada, K. Makise, Y. Uzawa, H. Terai, Z. Wang, R. Shimano, Phys. Rev. Lett. **111**, 057002 (2013)
45. R. Matsunaga, N. Tsuji, H. Fujita, A. Sugioka, K. Makise, Y. Uzawa, H. Terai, Z. Wang, H. Aoki, R. Shimano, Science **345**, 6201 (2014)
46. D. Sherman, U.S. Pracht, B. Gorshunov, S. Poran, J. Jesudasan, M. Chand, P. Raychaudhuri, M. Swanson, N. Trivedi, A. Auerbach, M. Scheffler, A. Frydman, M. Dressel, Nat. Phys. **11**, 188 (2015)
47. R. Matsunaga, N. Tsuji, K. Makise, H. Terai, H. Aoki, R. Shimano, Phys. Rev. B **96**, 020505(R) (2017)
48. Ch. Rüegg, B. Normand, M. Matsumoto, A. Furrer, D.F. McMorrow, K.W. Kramer, H.U. Gudel, S.N. Gvasaliya, H. Mutka, M. Boehm, Phys. Rev. Lett. **100**, 205701 (2008)
49. P. Merchant, B. Normand, K.W. Krämer, M. Boehm, D.F. McMorrow, Ch. Rüegg, Nat. Phys. **10**, 373 (2014)
50. H. Kuroe, N. Takami, N. Niwa, T. Sekine, M. Matsumoto, F. Yamada, H. Tanaka, K. Takemura, J. Phys.: Conf. Ser. **400**, 032042 (2012)
51. J. Demsar, K. Biljaković, D. Mihailovic, Phys. Rev. Lett. **83**, 800 (1999)
52. H. Schaefer, V.V. Kabanov, J. Demsar, Phys. Rev. B **89**, 045106 (2014)
53. R. Yusupov, T. Mertelj, V.V. Kabanov, S. Brazovskii, P. Kusar, J.-H. Chu, I.R. Fisher, D. Mihailovic, Nat. Phys. **6**, 681 (2010)
54. T. Mertelj, P. Kusar, V.V. Kabanov, P. Giraldo-Gallo, I.R. Fisher, D. Mihailovic, Phys. Rev. Lett. **110**, 156401 (2013)
55. O. Avenel, E. Varoquaux, H. Ebisawa, Phys. Rev. Lett. **45**, 1952 (1980)
56. C.A. Collett, J. Pollanen, J.I.A. Li, W.J. Gannon, W.P. Halperin, J. Low Temp. Phys. **171**, 214 (2013)
57. A. Behrle, T. Harrison, J. Kombe, K. Gao, M. Link, J.-S. Bernier, C. Kollath, M. Köhl, Nat. Phys. **14**, 781 (2018)
58. U. Bissbort, S. Götze, Y. Li, J. Heinze, J.S. Krauser, M. Weinberg, C. Becker, K. Sengstock, W. Hofstetter, Phys. Rev. Lett. **106**, 205303 (2011)
59. M. Endres, T. Fukuhara, D. Pekker, M. Cheneau, P. Schauβ, C. Gross, E. Demler, S. Kuhrm, I. Bloch, Nature **487**, 454 (2012)
60. P.W. Higgs, Phys. Rev. Lett. **13**, 508 (1964)
61. D. Podolsky, A. Auerbach, D.P. Arovas, Phys. Rev. B **84**, 174522 (2011)
62. K. Nagao, I. Danshita, Prog. Theor. Exp. Phys. **2016**, 063I01 (2016)
63. A. Auerbach, *Interacting Electrons and Quantum Magnetism* (Springer, New York, 1994)
64. A. Polkovnikov, Phys. Rev. B **72**, 161201(R) (2005)
65. S.M. Davidson, A. Polkovnikov, Phys. Rev. Lett. **114**, 045701 (2015)
66. T. Holstein, H. Primakoff, Phys. Rev. **58**, 1908 (1940)
67. L. Pitaevskii, S. Stringari, *Bose-Einstein Condensation* (Oxford University Press, New York, 2003)

Chapter 3
Phase Space Methods for Quantum Dynamics

Abstract In this chapter, we review the phase-space method, which represents quantum systems using classical phase-space variables and quasi-probability distribution functions. In Sect. 3.1, we provide a general overview of the phase-space method and introduce the Wigner function for a quantum state and the Wigner–Weyl transform of operators, especially in the coordinate-momentum phase space. In Sect. 3.2, we formulate the phase-space representation of Bose fields using the Wigner function spanned by the coherent-state basis. In Sect. 3.3, we represent quantum dynamics of Bose fields by means of the time-dependent Wigner function and discuss the truncated-Wigner semiclassical approximation through two different ways.

3.1 Introduction

Phase-space representation of quantum systems provides a useful and interesting way to express general quantum states of quantized particles or fields using a distribution function in a classical phase space. For instance, a single-particle quantum state described by a density operator $\hat{\rho}$ can be represented by using a Wigner function [1], which is a distribution function defined in the coordinate-momentum phase space $(x, p) \in \mathbb{R}^2$:

$$W(x, p) = \int_{-\infty}^{\infty} dy \left\langle x - \frac{y}{2} \middle| \hat{\rho} \middle| x + \frac{y}{2} \right\rangle e^{\frac{i}{\hbar} p \cdot y}, \tag{3.1}$$

where $|x\rangle$ ($\langle x|$) is a ket (bra) vector with a position x. Unlike standard distribution functions encountered in classical statistical mechanics, the Wigner function is not positive definite. For such a reason, Eq. (3.1) is often termed a quasi-probability distribution function (for reviews of the Wigner function, see e.g. Refs. [2–5]).

K. Nagao, *Fluctuations and Non-Equilibrium Phenomena in Strongly-Correlated Ultracold Atoms*, Springer Theses, https://doi.org/10.1007/978-981-15-7171-8_3

The Wigner function allows us to express the quantum average of arbitrary operators using entirely classical objects. Let us consider the quantum average of an arbitrary operator $\hat{\Omega}(\hat{x}, \hat{p})$ with respect to the density operator $\hat{\rho}$, which is given by

$$\langle \hat{\Omega}(\hat{x}, \hat{p}) \rangle = \mathrm{Tr}\left\{ \hat{\rho} \hat{\Omega}(\hat{x}, \hat{p}) \right\}. \tag{3.2}$$

This can be translated into a phase-space integration form, where a classical function corresponding to $\hat{\Omega}(\hat{x}, \hat{p})$ is weighted with the coordinate-momentum Wigner function [2]:

$$\langle \hat{\Omega}(\hat{x}, \hat{p}) \rangle = \frac{1}{2\pi\hbar} \int dx dp W(x, p) \Omega_W(x, p). \tag{3.3}$$

Here, the classical function $\Omega_W(x, p)$ is referred to as the Wigner–Weyl transform [2] of $\hat{\Omega}(\hat{x}, \hat{p})$ (a.k.a. Weyl symbol) defined by

$$\Omega_W(x, p) = \int_{-\infty}^{\infty} dy \left\langle x - \frac{y}{2} \right| \hat{\Omega} \left| x + \frac{y}{2} \right\rangle e^{\frac{i}{\hbar} p \cdot y}. \tag{3.4}$$

Notice that the Wigner function is nothing else but the Weyl symbol of the density operator $\hat{\rho}$. The Weyl symbol is closely related with the Weyl-ordering rule for operator products of $\hat{x}$ and $\hat{p}$ [5, 6]. The above discussion for the single particle can be generalized into multi-particle cases straightforwardly.

In the so called Wigner (or Wigner–Weyl) representation based on the quasi-probability distribution function, the dynamics of the density operator in the Hilbert space are translated into those of the Wigner function in the phase space [2]. The corresponding phase-space equation is described by a generalized Poisson bracket, i.e., the so called Moyal bracket [7]. For two arbitrary operators $\hat{A}$ and $\hat{B}$, the Moyal bracket is defined by

$$\{A_W, B_W\}_{\mathrm{M.B.}} = \frac{2}{\hbar} A_W(x, p) \sin\left[\frac{\hbar}{2} \Lambda_{cm} \right] B_W(x, p), \tag{3.5}$$

where

$$\Lambda_{cm} = \frac{\overleftarrow{\partial}}{\partial x} \frac{\overrightarrow{\partial}}{\partial p} - \frac{\overleftarrow{\partial}}{\partial p} \frac{\overrightarrow{\partial}}{\partial x} \tag{3.6}$$

is the symplectic operator in the coordinate-momentum space. If one takes a classical limit $\hbar \to 0$, it is reduced to the standard Poisson bracket. As we will see later, the Moyal bracket is nothing else but the Weyl symbol of a commutator of two operators $[\hat{A}, \hat{B}]$, i.e., $([\hat{A}, \hat{B}])_W(x, p)$. Using the Moyal bracket, we can write down the equation of motion of the Wigner function as follows:

$$\frac{\partial W}{\partial t} = \{H_W, W\}_{\text{M.B.}} = \frac{2}{\hbar} H_W \sin\left[\frac{\hbar}{2}\Lambda_{cm}\right] W, \tag{3.7}$$

where H_W is a classical function mapped from a Hamiltonian operator through the Wigner–Weyl transform.

A similar representation by use of the Wigner function can be made for a system of Bose fields describing, e.g., photons or bosonic atoms [3, 4]. There, it is convenient to span the phase-space distribution function by means of the coherent state basis [2, 8]. The coherent state introduces a complex classical field as a phase-space variable. Such a complex field corresponds to a natural classical limit for Bose fields, especially for coherent bosons. The time evolution of the coherent-state Wigner function is described by a similar equation to Eq. (3.7) [5].

Our main purpose of this chapter is to provide the coherent-state Wigner representation of general Bose fields and show how to utilize it for describing quantum dynamics of the systems. In particular, we focus on a useful fact that within a semiclassical regime one can reduce the computational difficulty in simulating the quantum dynamics. Indeed, when the system is in a nearly classical limit, the dynamics of the system are approximated by a set of deterministic Hamilton or Gross–Pitaevskii trajectories of the classical field, whose initial conditions are weighted with the initial Wigner function. This treatment is often referred to as the truncated-Wigner approximation (TWA) in quantum optics and other fields [5, 9]. Since the number of the classical equations of motion is proportional to the total mode number or system size, the TWA is applicable even to macroscopic quantum many-body systems, to which exact numerical methods are inaccessible due to the exponentially-large Hilbert space.

In the past two decades, TWA or related semiclassical frameworks were widely used to explore non-equilibrium phenomena of isolated Bose gases trapped by optical lattices [5, 10–23], quantum spin systems [5, 24–27], open quantum systems [4, 28–32], spin-boson models [33–35], and interacting fermions [36–38]. In earlier works on interacting bosons in optical lattices [10, 11, 13, 19, 20, 22], it was argued that in a weakly interacting regime the semiclassical approach can be used to describe the time evolution induced by a sudden quench from a Mott-insulator state. However, the application of such semiclassical approaches to the three-dimensional (3D) case at unit filling, which is the situation realized in the experiment [39], has not been demonstrated in practice. One of the goals of this Thesis is to apply a TWA method, which was previously used to study dynamics of the one-dimensional (1D) Bose–Hubbard at a large-filling factor [10, 11, 13], to the experimental setup of Ref. [39] that the 3D Bose–Hubbard model is quenched from a singly-occupied Mott-insulator state. The details of the numerical simulation and direct comparison with the experimental data will be presented in Chap. 5.

3.2 Wigner Representation of Bose Fields

3.2.1 Coherent-State Phase Space Representation

Let us consider a single-mode Bose field described by boson annihilation and creation operators, $\hat{a}$ and $\hat{a}^\dagger$. An important step to build a phase-space representation of the Bose field is to introduce the coherent state [8], which is given by

$$|\alpha\rangle = \hat{D}(\alpha)|0\rangle, \quad \langle\alpha| = \langle 0|\hat{D}^\dagger(\alpha) = \langle 0|\hat{D}(-\alpha), \tag{3.8}$$

where $\alpha \in \mathbb{C}$ is a complex number, $\hat{D}(\alpha) = e^{\alpha\hat{a}^\dagger - \alpha^*\hat{a}}$ is the so called displacement operator [4], and $|0\rangle$ represents the vacuum state of the Bose field. This vector is normalized as $\langle\alpha|\alpha\rangle = 1$. The displacement operator is a unitary operator, and it yields a unitary transformation that adds an offset to the canonical field operators such that $\hat{a} \to \hat{a} + \alpha$, hence,

$$\hat{D}^\dagger(\alpha)\hat{a}\hat{D}(\alpha) = \hat{a} + \alpha, \quad \hat{D}^\dagger(\alpha)\hat{a}^\dagger\hat{D}(\alpha) = \hat{a}^\dagger + \alpha^*. \tag{3.9}$$

Because of this property, the coherent state is found to be a right (left) eigenstate of the field operator $\hat{a}$ ($\hat{a}^\dagger$),

$$\hat{a}|\alpha\rangle = \alpha|\alpha\rangle, \quad \langle\alpha|\hat{a}^\dagger = \alpha^*\langle\alpha|, \tag{3.10}$$

and the number α gives the resulting complex eigenvalues. This vector produces an over-complete basis to span the Hilbert space and satisfies a completeness relation

$$\int \frac{d^2\alpha}{\pi}|\alpha\rangle\langle\alpha| = \hat{1}, \tag{3.11}$$

where $d^2\alpha/\pi \equiv d\mathrm{Re}\,[\alpha]\,d\mathrm{Im}\,[\alpha]\,/\pi$. The conjugated pair (α, α^*) of the coherent-state index plays a role of natural phase-space variables for the Bose field in the following discussions.

The coherent state basis makes key ingredients for representing the Bose field using phase-space variables, i.e., the Weyl symbol of operators and Wigner function for quantum states. For the single-mode Bose field, the Weyl symbol of an arbitrary operator $\hat{\Omega} = \hat{\Omega}(\hat{a}, \hat{a}^\dagger)$ is defined as

$$\Omega_W(\alpha, \alpha^*) = \frac{1}{2}\int d\eta d\eta^* \left\langle \alpha - \frac{\eta}{2}\right| \hat{\Omega} \left|\alpha + \frac{\eta}{2}\right\rangle e^{\frac{1}{2}(\eta^*\alpha - \alpha^*\eta)}, \tag{3.12}$$

where $d\eta d\eta^* = d^2\eta/\pi$. When we insert a density operator $\hat{\rho}$ into $\hat{\Omega}$, it results in the corresponding Wigner function

$$W(\alpha,\alpha^*)=\frac{1}{2}\int d\eta d\eta^*\left\langle\alpha-\frac{\eta}{2}\right|\hat{\rho}\left|\alpha+\frac{\eta}{2}\right\rangle e^{\frac{1}{2}(\eta^*\alpha-\alpha^*\eta)}. \tag{3.13}$$

Using these classical functions, the quantum average of $\hat{\Omega}$ with respect to $\hat{\rho}$, i.e., $\langle\hat{\Omega}\rangle=\mathrm{Tr}[\hat{\rho}\hat{\Omega}]$, is written as

$$\langle\hat{\Omega}\rangle=\int d\alpha d\alpha^*\Omega_W(\alpha,\alpha^*)W(\alpha,\alpha^*). \tag{3.14}$$

This equation corresponds to Eq. (3.3) in the coordinate-momentum representation. The detailed derivation of Eq. (3.14) will be given in Sect. 3.2.4.

The multi-mode generalization of Eqs. (3.12)–(3.14) is straightforward: When the Bose field possesses an M-number of distinct modes, then the corresponding Weyl symbol and Wigner function are generalized into

$$\Omega_W(\boldsymbol{\alpha},\boldsymbol{\alpha}^*)=\frac{1}{2^M}\int d\boldsymbol{\eta}^* d\boldsymbol{\eta}\left\langle\boldsymbol{\alpha}-\frac{\boldsymbol{\eta}}{2}\right|\hat{\Omega}\left|\boldsymbol{\alpha}+\frac{\boldsymbol{\eta}}{2}\right\rangle e^{\frac{1}{2}(\boldsymbol{\eta}^*\cdot\boldsymbol{\alpha}-\boldsymbol{\alpha}^*\cdot\boldsymbol{\eta})}, \tag{3.15}$$

$$W(\boldsymbol{\alpha},\boldsymbol{\alpha}^*)=\frac{1}{2^M}\int d\boldsymbol{\eta}^* d\boldsymbol{\eta}\left\langle\boldsymbol{\alpha}-\frac{\boldsymbol{\eta}}{2}\right|\hat{\rho}\left|\boldsymbol{\alpha}+\frac{\boldsymbol{\eta}}{2}\right\rangle e^{\frac{1}{2}(\boldsymbol{\eta}^*\cdot\boldsymbol{\alpha}-\boldsymbol{\alpha}^*\cdot\boldsymbol{\eta})}, \tag{3.16}$$

where $\boldsymbol{\alpha}=(\alpha_1,\alpha_2,\ldots,\alpha_M)$ indicates a point in the $2M$-dimensional phase space and $d\boldsymbol{\eta}d\boldsymbol{\eta}^*=\prod_{i=1}^M d\eta_i d\eta_i^*=\prod_{i=1}^M[d^2\eta_i/\pi]$. The multiple coherent state $|\boldsymbol{\alpha}\rangle$ is written as a product state of the single-mode coherent state:

$$|\boldsymbol{\alpha}\rangle=\hat{D}_1(\alpha_1)\hat{D}_2(\alpha_2)\cdots\hat{D}_M(\alpha_M)|0,0,\ldots,0\rangle=\bigotimes_{i=1}^M\hat{D}_i(\alpha_i)|0\rangle, \tag{3.17}$$

where $\hat{D}_i(\alpha_i)\equiv e^{\alpha_i\hat{a}_i^\dagger-\alpha_i^*\hat{a}_i}$ and $[\hat{D}_i(\alpha_i),\hat{D}_j(\alpha_j)]=0$ for $i\neq j$. Thus, we obtain a general formula of the phase-space averaging:

$$\langle\hat{\Omega}\rangle=\int d\boldsymbol{\alpha}d\boldsymbol{\alpha}^*\Omega_W(\boldsymbol{\alpha},\boldsymbol{\alpha}^*)W(\boldsymbol{\alpha},\boldsymbol{\alpha}^*). \tag{3.18}$$

3.2.2 *Weyl Symbols and Weyl Ordering*

To illustrate the mapping of Eq. (3.12) from operators to classical functions, we calculate Weyl symbols of operators in practice. First, let us consider an operator where the canonical pairs are decoupled such that $\hat{\Omega}(\hat{a},\hat{a}^\dagger)=A(\hat{a})+B(\hat{a}^\dagger)$. When we choose $A(x)=ax^n$ and $B(x)=bx^m$, the corresponding Weyl symbol is given as

$$(\hat{\Omega})_W(\alpha,\alpha^*)=a\alpha^n+b(\alpha^*)^m. \tag{3.19}$$

Indeed, it can be confirmed that

$$\begin{aligned}
[\hat{a}^n]_W(\alpha,\alpha^*) &= \frac{1}{2}\int \frac{d^2\eta}{\pi}\left\langle \alpha-\frac{\eta}{2}\right|\hat{a}^n\left|\alpha+\frac{\eta}{2}\right\rangle e^{\frac{1}{2}(\eta^*\alpha-\alpha^*\eta)} \\
&= \frac{1}{2}\int \frac{d^2\eta}{\pi}\left(\alpha+\frac{\eta}{2}\right)^n e^{-\frac{1}{2}|\eta|^2} \\
&= \alpha^n, \\
[(\hat{a}^\dagger)^m]_W(\alpha,\alpha^*) &= \frac{1}{2}\int \frac{d^2\eta}{\pi}\left(\alpha^*-\frac{\eta^*}{2}\right)^m e^{-\frac{1}{2}|\eta|^2} \\
&= (\alpha^*)^m.
\end{aligned}$$

To calculate them, we have used two relations, i.e., the overlap between $|\alpha\rangle$ and $|\beta\rangle$

$$\langle\alpha|\beta\rangle = e^{-\frac{1}{2}|\alpha|^2-\frac{1}{2}|\beta|^2+\alpha^*\beta}, \tag{3.20}$$

and a set of Gaussian integrals,

$$[1]_\eta = 1, \quad [|\eta|^n]_\eta = 2^n n!, \quad [\eta^n]_\eta = [(\eta^*)^m]_\eta = 0, \tag{3.21}$$

where $[f(\eta,\eta^*)]_\eta = \frac{1}{2}\int \frac{d^2\eta}{\pi} f(\eta,\eta^*)e^{-\frac{1}{2}|\eta|^2}$. Thus, for the decoupled operators, the Weyl symbol can be obtained from replacing the canonical operators with corresponding classical numbers: $(\hat{\alpha},\hat{\alpha}^\dagger)\to(\alpha,\alpha^*)$.

The same operational manual based on such a replacement is also true when the operator of interest is fully symmetrized with respect to the canonical variables. To see that, let us consider a symmetrized operator

$$\frac{\hat{a}^\dagger\hat{a}+\hat{a}\hat{a}^\dagger}{2}. \tag{3.22}$$

Using Eqs. (3.12), (3.20), and (3.21), we find that the resulting Weyl symbol coincides with the classical number obtained from the replacement into Eq. (3.22):

$$\frac{1}{2}[\hat{a}^\dagger\hat{a}+\hat{a}\hat{a}^\dagger]_W(\alpha,\alpha^*) = \alpha^*\alpha. \tag{3.23}$$

This property implies the standard Weyl-ordering rule of operators that a c-number product constructed from some phase-space variables corresponds to a fully-symmetrized product of operators.

In contrast, if Eq. (3.22) is not symmetrized, for instance, if it is written as $\hat{a}^\dagger\hat{a}$ or $\hat{a}\hat{a}^\dagger$, then, there arises a constant factor in addition to $\alpha^*\alpha$:

$$[\hat{a}^\dagger\hat{a}]_W(\alpha,\alpha^*) = \alpha^*\alpha-\frac{1}{2}, \quad [\hat{a}\hat{a}^\dagger]_W(\alpha,\alpha^*) = \alpha\alpha^*+\frac{1}{2}. \tag{3.24}$$

The factors follow from the non-commutativity of the canonical variables $[\hat{a}, \hat{a}^\dagger] = 1$. Indeed, when we rewrite them as a fully symmetrized form, and perform the replacement, the same results are recovered:

$$\hat{a}^\dagger \hat{a} = \frac{\hat{a}^\dagger \hat{a} + \hat{a}\hat{a}^\dagger}{2} + \frac{1}{2}[\hat{a}^\dagger, \hat{a}] \to \alpha^* \alpha - \frac{1}{2},$$
$$\hat{a}\hat{a}^\dagger = \frac{\hat{a}^\dagger \hat{a} + \hat{a}\hat{a}^\dagger}{2} + \frac{1}{2}[\hat{a}, \hat{a}^\dagger] \to \alpha^* \alpha + \frac{1}{2}.$$

3.2.3 *Moyal Products and Bopp Operators*

In the coherent-state phase space, we can also define the Moyal product between two classical functions. For arbitrary operators $\hat{A}$ and $\hat{B}$, the Weyl symbol of the product of them, $(\hat{A}\hat{B})_W$, is expressed as follows [5]:

$$(\hat{A}\hat{B})_W(\alpha, \alpha^*) \equiv A_W(\alpha, \alpha^*) \exp\left[\frac{1}{2}\Lambda_c\right] B_W(\alpha, \alpha^*) \tag{3.25}$$
$$= B_W(\alpha, \alpha^*) \exp\left[-\frac{1}{2}\Lambda_c\right] A_W(\alpha, \alpha^*), \tag{3.26}$$

where Λ_c is the symplectic operator in the coherent phase space, given by

$$\Lambda_c = \frac{\overleftarrow{\partial}}{\partial\alpha}\frac{\overrightarrow{\partial}}{\partial\alpha^*} - \frac{\overleftarrow{\partial}}{\partial\alpha^*}\frac{\overrightarrow{\partial}}{\partial\alpha}. \tag{3.27}$$

The symplectic operator is a formal representation of the Poisson bracket in the complex phase space between $A_W(\alpha, \alpha^*)$ and $B_W(\alpha, \alpha^*)$:

$$A_W \Lambda_c B_W = \frac{\partial A_W}{\partial\alpha}\frac{\partial B_W}{\partial\alpha^*} - \frac{\partial A_W}{\partial\alpha^*}\frac{\partial B_W}{\partial\alpha} = \{A_W, B_W\}_{\text{P.B.}}. \tag{3.28}$$

Using the Moyal product (3.26), it is easy to obtain again the result of Eq. (3.24):

$$(\hat{a}^\dagger \hat{a})_W(\alpha, \alpha^*) = \alpha^* \left[1 + \frac{1}{2}\Lambda_c + \cdots\right]\alpha = \alpha^*\alpha - \frac{1}{2},$$
$$(\hat{a}\hat{a}^\dagger)_W(\alpha, \alpha^*) = \alpha \left[1 + \frac{1}{2}\Lambda_c + \cdots\right]\alpha^* = \alpha^*\alpha + \frac{1}{2}.$$

The concept of the Moyal product leads to the Moyal bracket, which is defined as a commutator associated with the Moyal product

$$\{A_W, B_W\}_{\text{M.B.}} \equiv A_W \star B_W - B_W \star A_W$$
$$= 2A_W \sinh\left[\frac{1}{2}\Lambda_c\right] B_W. \tag{3.29}$$

Here we have introduced the *star-product* notation, $A_W \star B_W = (\hat{A}\hat{B})_W$, for indicating the Moyal product. We note that the Moyal bracket is equivalent to the Weyl symbol of a commutator $[\hat{A}, \hat{B}]$, i.e.,

$$\{A_W, B_W\}_{\text{M.B.}} = ([\hat{A}, \hat{B}])_W. \tag{3.30}$$

If we take a classical limit, the Moyal bracket reduces to the Poisson bracket

$$\{A_W, B_W\}_{\text{M.B.}} \approx \{A_W, B_W\}_{\text{P.B.}}. \tag{3.31}$$

This limit is formally equivalent to eliminating higher-order terms of expansion of Eq. (3.29) in Λ_c.

It is also possible to calculate Weyl symbols using Bopp operators for the canonical variables [4, 5]. For the Bose operators $\hat{a}$ and $\hat{a}^\dagger$, the corresponding right-derivative Bopp operators are introduced as

$$\hat{a} \to \alpha + \frac{1}{2}\frac{\partial}{\partial \alpha^*}, \quad \hat{a}^\dagger \to \alpha^* - \frac{1}{2}\frac{\partial}{\partial \alpha}. \tag{3.32}$$

Using the Bopp operators, the Weyl symbols of $\hat{a}^\dagger\hat{a}$ and $\hat{a}\hat{a}^\dagger$ are calculated as follows:

$$\hat{a}^\dagger\hat{a}\hat{1} \to \left(\alpha^* - \frac{1}{2}\frac{\partial}{\partial \alpha}\right)\left(\alpha + \frac{1}{2}\frac{\partial}{\partial \alpha^*}\right)1 = \alpha^*\alpha - \frac{1}{2},$$
$$\hat{a}\hat{a}^\dagger\hat{1} \to \left(\alpha + \frac{1}{2}\frac{\partial}{\partial \alpha^*}\right)\left(\alpha^* - \frac{1}{2}\frac{\partial}{\partial \alpha}\right)1 = \alpha^*\alpha + \frac{1}{2}.$$

Moreover, we can write down left-derivative Bopp operators instead of the right-derivative ones, which are given by

$$\hat{a} \to \alpha - \frac{1}{2}\frac{\overleftarrow{\partial}}{\partial \alpha^*}, \quad \hat{a}^\dagger \to \alpha^* + \frac{1}{2}\frac{\overleftarrow{\partial}}{\partial \alpha}. \tag{3.33}$$

A similar calculation to the above is performed as follows:

$$\hat{1}\hat{a}^\dagger\hat{a} \to 1\left(\alpha^* + \frac{1}{2}\frac{\overleftarrow{\partial}}{\partial \alpha}\right)\left(\alpha - \frac{1}{2}\frac{\overleftarrow{\partial}}{\partial \alpha^*}\right) = \alpha^*\alpha - \frac{1}{2},$$
$$\hat{1}\hat{a}\hat{a}^\dagger \to 1\left(\alpha - \frac{1}{2}\frac{\overleftarrow{\partial}}{\partial \alpha^*}\right)\left(\alpha^* + \frac{1}{2}\frac{\overleftarrow{\partial}}{\partial \alpha}\right) = \alpha^*\alpha + \frac{1}{2}.$$

It is important to note that the Bopp-operator replacement is also valid for the time-dependent Heisenberg operators within a semiclassical limit (see Ref. [5]). The time-dependent Bopp operator is very useful to derive semiclassical representations of non-equal time correlation functions of the field operators.

3.2.4 Displacement Operator Expansion

It is convenient to expand an arbitrary operator $\hat{A}$ with respect to the displacement operator $\hat{D}(\alpha)$ [2, 40] as

$$\hat{A} = \int \frac{d^2\alpha}{\pi} \chi_A(\alpha) \hat{D}(\alpha), \tag{3.34}$$

in which the coefficient $\chi_A(\alpha)$ is referred to as the characteristic function of $\hat{A}$. Since the displacement operator satisfies relations

$$\hat{D}(\alpha)\hat{D}(\beta) = e^{\frac{1}{2}(\alpha\beta^* - \alpha^*\beta)} \hat{D}(\alpha + \beta), \tag{3.35}$$

$$\mathrm{Tr}[\hat{D}(\alpha)\hat{D}(\beta)] = \pi \delta^{(2)}(\alpha + \beta), \tag{3.36}$$

the characteristic function is given by

$$\chi_A(\alpha) = \mathrm{Tr}\left[\hat{A}\hat{D}^\dagger(\alpha)\right]. \tag{3.37}$$

Here we introduced the delta function in the complex plane given by

$$\delta^{(2)}(\alpha) = \frac{1}{\pi} \int \frac{d^2\xi}{\pi} e^{\alpha\xi^* - \xi\alpha^*}. \tag{3.38}$$

Notice that this expansion is similar with the usual expansion of a vector in a linear space with respect to an adequate basis. In particular, the trace operation implies an inner product between two *vectors* $\hat{D}(\alpha)$ and $\hat{D}^\dagger(\beta)$.

Starting from the displacement operator expansion (3.34), we can derive the phase-space representations in the previous subsections, which were given with no proof, and some useful formulae. Let us consider the Weyl symbol of Eq. (3.34):

$$A_W(\alpha) = \int \frac{d^2\xi}{\pi} \chi_A(\xi)[\hat{D}(\xi)]_W(\alpha). \tag{3.39}$$

The Weyl symbol of $\hat{D}(\xi)$ can be obtained from replacing the field operators with the corresponding complex numbers because the operator is written as the Weyl-ordered form. Therefore, $A_W(\alpha)$ reads

$$A_W(\alpha) = \int \frac{d^2\beta}{\pi} \chi_A(\beta) e^{\beta\alpha^* - \beta^*\alpha}. \tag{3.40}$$

If we substitute Eq. (3.34) into Eq. (3.12), we are able to obtain again this result. Indeed, it is checked that

$$\begin{aligned} A_W(\alpha) &= \frac{1}{2} \int \frac{d^2\eta}{\pi} \frac{d^2\xi}{\pi} \chi_A(\xi) \left\langle \alpha - \frac{\eta}{2} \right| \hat{D}(\xi) \left| \alpha + \frac{\eta}{2} \right\rangle e^{\frac{1}{2}(\eta^*\alpha - \alpha^*\eta)} \\ &= \frac{1}{2} \int \frac{d^2\eta}{\pi} \frac{d^2\xi}{\pi} \chi_A(\xi) e^{\xi\alpha^* - \xi^*\alpha - \frac{1}{2}|\eta+\xi|^2} \\ &= \frac{1}{2} \int \frac{d^2\xi}{\pi} \left[\int \frac{d^2\eta}{\pi} e^{-\frac{1}{2}|\eta|^2 - \frac{1}{2}(\eta^*\xi + \xi^*\eta)} \right] e^{-\frac{1}{2}|\xi|^2} \chi_A(\xi) e^{\xi\alpha^* - \xi^*\alpha} \\ &= \int \frac{d^2\xi}{\pi} \chi_A(\xi) e^{\xi\alpha^* - \xi^*\alpha}. \end{aligned} \tag{3.41}$$

In the last equality, we have performed a complex Gauss integration with respect to η [see, e.g., Eq. (3.52)]. Therefore, Eq. (3.40) gives another definition of the Weyl symbol of operators.

Next we express the trace of two arbitrary operators, $\mathrm{Tr}[\hat{A}\hat{B}]$, using the classical functions with the phase-space integration. Substituting Eq. (3.34) into the expression, it is found that

$$\begin{aligned} \mathrm{Tr}[\hat{A}\hat{B}] &= \int \frac{d^2\alpha}{\pi} \frac{d^2\beta}{\pi} \chi_A(\alpha) \chi_B(\beta) \mathrm{Tr}[\hat{D}(\alpha)\hat{D}(\beta)] \\ &= \int \frac{d^2\alpha}{\pi} \frac{d^2\beta}{\pi} \chi_A(\alpha) \chi_B(\beta) \cdot \pi\delta^{(2)}(\alpha + \beta) \\ &= \int \frac{d^2\alpha}{\pi} A_W(\alpha) B_W(\alpha). \end{aligned} \tag{3.42}$$

If we insert $\hat{A} = \hat{\Omega}$ and $\hat{B} = \hat{\rho}$, then Eq. (3.14) is recovered. In addition, this relation allows the characteristic function χ_A to be rewritten as a function of A_W:

$$\chi_A(\alpha) = \int \frac{d^2\xi}{\pi} A_W(\xi) e^{-\alpha\xi^* + \alpha^*\xi}. \tag{3.43}$$

Let us compute the Weyl symbol of a product of two arbitrary operators $\hat{A}$ and $\hat{B}$, i.e., $\hat{A}\hat{B}$. Using Eqs. (3.34), (3.38), and (3.42), we can perform the following calculations:

$$
\begin{aligned}
(\hat{A}\hat{B})_W(\alpha) &= \int \frac{d^2\eta}{\pi}\frac{d^2\xi}{\pi}\chi_A(\eta)\chi_B(\xi)[\hat{D}(\eta)\hat{D}(\xi)]_W(\alpha) \\
&= \int \frac{d^2\eta}{\pi}\frac{d^2\xi}{\pi}\chi_A(\eta)\chi_B(\xi)e^{\frac{1}{2}(\eta\xi^*-\eta^*\xi)}e^{(\eta+\xi)\alpha^*-(\eta^*+\xi^*)\alpha} \\
&= \int \frac{d^2\eta}{\pi}\frac{d^2\xi}{\pi}\frac{d^2\alpha_0}{\pi}\frac{d^2\beta_0}{\pi}A_W(\alpha_0)B_W(\beta_0) \\
&\qquad \times e^{-\eta\alpha_0^*+\eta^*\alpha_0-\xi\beta_0^*+\xi^*\beta_0}e^{\frac{1}{2}(\eta\xi^*-\eta^*\xi)}e^{(\eta+\xi)\alpha^*-(\eta^*+\xi^*)\alpha} \\
&= \int \frac{d^2\alpha_0}{\pi}\frac{d^2\eta}{\pi}A_W(\alpha_0)B_W(\alpha-\eta/2)e^{\eta(\alpha^*-\alpha_0^*)-\eta^*(\alpha-\alpha_0)}.
\end{aligned}
$$

Taking a transformation $\eta \to -2\alpha_0 - \sigma + 2\alpha$ under the integration of α_0, we obtain

$$
(\hat{A}\hat{B})_W(\alpha) = \int \frac{d^2\alpha_0 d^2\sigma}{\pi^2}A_W(\alpha_0)B_W(\alpha_0+\sigma/2)e^{\sigma^*(\alpha-\alpha_0)-\sigma(\alpha^*-\alpha_0^*)}. \tag{3.44}
$$

It is also possible to express this equation such that σ appears in the argument of $A_W(\alpha)$:

$$
(\hat{A}\hat{B})_W(\alpha) = \int \frac{d^2\alpha_0 d^2\sigma}{\pi^2}A_W(\alpha_0-\sigma/2)B_W(\alpha_0)e^{\sigma^*(\alpha-\alpha_0)-\sigma(\alpha^*-\alpha_0^*)}. \tag{3.45}
$$

Similarly, we can obtain the Weyl symbol of $\hat{B}\hat{A}$:

$$
(\hat{B}\hat{A})_W(\alpha) = \int \frac{d^2\alpha_0 d^2\sigma}{\pi^2}A_W(\alpha_0+\sigma/2)B_W(\alpha_0)e^{\sigma^*(\alpha-\alpha_0)-\sigma(\alpha^*-\alpha_0^*)}, \tag{3.46}
$$

$$
= \int \frac{d^2\alpha_0 d^2\sigma}{\pi^2}A_W(\alpha_0)B_W(\alpha_0-\sigma/2)e^{\sigma^*(\alpha-\alpha_0)-\sigma(\alpha^*-\alpha_0^*)}. \tag{3.47}
$$

Thus, the permutation of $\hat{A}$ and $\hat{B}$ leads to the sign inversion of σ in the argument of A_W or B_W.

If we expand $B_W(\alpha_0+\sigma/2)$ with respect to σ such that

$$
B_W(\alpha_0+\sigma/2) = B_W(\alpha_0) + \frac{\sigma}{2}\frac{\partial B_W(\alpha_0)}{\partial\alpha_0} + \frac{\sigma^*}{2}\frac{\partial B_W(\alpha_0)}{\partial\alpha_0^*} + \cdots, \tag{3.48}
$$

then, Eq. (3.44) reads

$$
\begin{aligned}
(\hat{A}\hat{B})_W(\alpha) &= \sum_{n,m=0}^{\infty}\frac{(-1)^n}{2^{m+n}m!n!}\frac{\partial^{m+n}A_W(\alpha)}{\partial\alpha^m(\partial\alpha^*)^n}\frac{\partial^{m+n}B_W(\alpha)}{\partial\alpha^n(\partial\alpha^*)^m} \\
&= A_W(\alpha)\exp\left[\frac{1}{2}\left(\frac{\overleftarrow{\partial}}{\partial\alpha}\frac{\overrightarrow{\partial}}{\partial\alpha^*} - \frac{\overleftarrow{\partial}}{\partial\alpha^*}\frac{\overrightarrow{\partial}}{\partial\alpha}\right)\right]B_W(\alpha).
\end{aligned}
$$

This is the derivation of the Moyal product given by Eq. (3.26). Furthermore, when $\hat{A} = \hat{a}$ and $\hat{B}$ is arbitrary, it follows from Eqs. (3.45) and (3.47) that

$$
\begin{aligned}
(\hat{a}\hat{B})_W(\alpha) &= \int \frac{d^2\alpha_0 d^2\sigma}{\pi^2}\left(\alpha_0 - \frac{\sigma}{2}\right) B_W(\alpha_0) e^{\sigma^*(\alpha-\alpha_0)-\sigma(\alpha^*-\alpha_0^*)} \\
&= \int \frac{d^2\alpha_0 d^2\sigma}{\pi^2}\left(\alpha_0 + \frac{1}{2}\frac{\partial}{\partial\alpha^*}\right) B_W(\alpha_0) e^{\sigma^*(\alpha-\alpha_0)-\sigma(\alpha^*-\alpha_0^*)} \\
&= \left(\alpha + \frac{1}{2}\frac{\partial}{\partial\alpha^*}\right) B_W(\alpha), \qquad (3.49)
\end{aligned}
$$

$$
(\hat{B}\hat{a})_W(\alpha) = \left(\alpha - \frac{1}{2}\frac{\partial}{\partial\alpha^*}\right) B_W(\alpha). \qquad (3.50)
$$

Hence, the Bopp operators, which were introduced in Sect. 3.2.3, are naturally derived from the simple starting point of Eq. (3.34).

3.2.5 *Wigner Functions*

In the coherent-state basis, the Wigner function exists as a quasi-probability distribution function in the complex-number phase space. Here, we present some examples of the Wigner functions for the Bose fields in the single-mode case. For reviews, see, e.g., Refs. [2–5, 9].

We start from the vacuum state denoted by $\hat{\rho} = |0\rangle\langle 0|$. Using Eq. (3.20), its Wigner function $W_{\rm vac} = (|0\rangle\langle 0|)_W$ reads

$$
W_{\rm vac}(\alpha, \alpha^*) = \frac{1}{2\pi}\int d^2\eta e^{-|\alpha|^2 - \frac{1}{4}|\eta|^2} e^{\frac{1}{2}(\eta^*\alpha - \alpha^*\eta)}. \qquad (3.51)
$$

The integration with respect to η and η^* can be performed directly by using the useful relation reviewed in Ref. [41]

$$
\int d^2z e^{-z^*wz + u^*z + z^*v} = \frac{\pi}{w} e^{\frac{u^*v}{w}}, \qquad (3.52)
$$

where $\mathrm{Re}[w] > 0$ and u^* and v are independent complex numbers. Thus, we obtain a Gaussian-form Wigner function with its variance $\sigma = 1/2$:

$$
W_{\rm vac}(\alpha, \alpha^*) = 2e^{-2|\alpha|^2}. \qquad (3.53)
$$

As seen in Fig. 3.1a, it describes the vacuum noise of the Bose field due to quantum fluctuations.

Similarly, we can also derive the Wigner function of the coherent state $|\alpha_0\rangle = \hat{D}(\alpha_0)|0\rangle$. The Weyl symbol of the density operator $|\alpha_0\rangle\langle\alpha_0|$ is given by

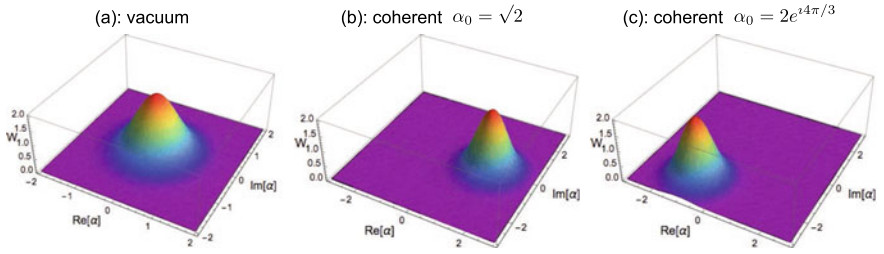

Fig. 3.1 Wigner functions of **a** the vacuum state and the coherent states with **b** $\alpha_0 = \sqrt{2}$ and **c** $\alpha_0 = 2e^{i4\pi/3}$

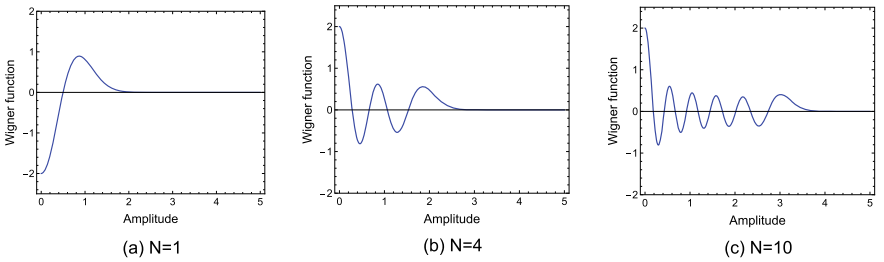

Fig. 3.2 Wigner functions of the Fock states at **a** $N = 1$, **b** $N = 4$, and **c** $N = 10$, respectively. The horizontal axis represents the radial direction of the phase space denoted by $|\alpha|$

$$W_{\alpha_0}(\alpha, \alpha^*) = 2e^{-2|\alpha-\alpha_0|^2}. \tag{3.54}$$

In Fig. 3.1, we show Eq. (3.54) with different values of α_0. As expected from Eq. (3.8), the central position of this distribution is shifted to $\alpha = \alpha_0$ compared with that of the vacuum Wigner function.

In contrast to the above examples, the Wigner function of Fock states takes negative values. Let us consider an N-particle Fock state given by

$$|N\rangle = \frac{1}{\sqrt{N!}}(\hat{a}^\dagger)^N|0\rangle. \tag{3.55}$$

Substituting $|N\rangle\langle N|$ into the definition, the Wigner function is written as

$$W_N(\alpha, \alpha^*) = \frac{1}{2N!\pi}\int d^2\eta \left(\alpha^* - \frac{\eta^*}{2}\right)^N \left(\alpha + \frac{\eta}{2}\right)^N e^{-|\alpha|^2 - \frac{1}{4}|\eta|^2} e^{(\eta^*\alpha - \alpha^*\eta)/2}.$$

The exponential factor can be separated into two independent factors such that

$$\exp\left[-\frac{1}{4}|\eta|^2 + \frac{1}{2}(\eta^*\alpha - \alpha^*\eta)\right] = e^{-|\alpha|^2} e^{-\frac{1}{4}\{\eta_1 - 2i\alpha_2\}^2} e^{-\frac{1}{4}\{\eta_2 + 2i\alpha_1\}^2}, \tag{3.56}$$

in which we have used $\eta_1 = \mathrm{Re}[\eta]$, $\eta_2 = \mathrm{Im}[\eta]$, $\alpha_1 = \mathrm{Re}[\alpha]$, and $\alpha_2 = \mathrm{Im}[\alpha]$. Introducing new variables of integration as

$$z_1 = \frac{\eta_1}{2} - i\alpha_2, \quad z_2 = \frac{\eta_2}{2} + i\alpha_1, \tag{3.57}$$

and noticing the fact that the integration of z_1 (z_2) over $[-\infty - i\alpha_2, \infty - i\alpha_2]$ ($[-\infty + i\alpha_1, \infty + i\alpha_1]$) is equal to the integration along the real axis over $[-\infty, \infty]$, we can evaluate the integral as

$$\begin{aligned} W_N(\alpha, \alpha^*) &= \frac{2}{\pi N!} e^{-2|\alpha|^2} \int d^2\tilde{\eta} (2\alpha^* - \tilde{\eta}^*)^N (2\alpha + \tilde{\eta})^N e^{-|\tilde{\eta}|^2}, \\ &= \frac{2}{\pi N!} e^{-2|\alpha|^2} \sum_{n=0}^{N} \sum_{m=0}^{N} \int d^2\tilde{\eta} \frac{N!(2\alpha^*)^{N-n}}{(N-n)!n!} \frac{N!(2\alpha)^{N-m}}{(N-m)!m!} (-\tilde{\eta}^*)^n (\tilde{\eta})^m e^{-|\tilde{\eta}|^2} \\ &= \frac{2}{\pi} e^{-2|\alpha|^2} \sum_{n=0}^{N} \frac{N!(-1)^n}{(N-n)!^2 n!^2} (4|\alpha|^2)^{N-n} \int d^2\tilde{\eta} |\tilde{\eta}|^{2n} e^{-|\tilde{\eta}|^2} \\ &= 2e^{-2|\alpha|^2} (-1)^N L_N(4|\alpha|^2), \end{aligned} \tag{3.58}$$

where

$$L_N(x) = \sum_{r=0}^{N} (-1)^r \frac{N!}{(N-r)!(r!)^2} x^r \tag{3.59}$$

is the Nth order Laguerre polynomial. Due to the property of the Laguerre polynomial, the Wigner function of the Fock state is not positive for $N > 0$. At $N = 0$, the function is positive because it corresponds to the vacuum state. In Fig. 3.2, we present $W_N(\alpha, \alpha^*)$ at different N.

3.3 Quantum Dynamics in the Coherent-State Phase Space

In this section, we formulate dynamics of a system of Bose fields in terms of the phase-space representation. When the system is isolated from external environments, its real time dynamics are governed by the von-Neumann equation

$$i\hbar \frac{\partial}{\partial t} \hat{\rho}(t) = [\hat{H}, \hat{\rho}(t)], \tag{3.60}$$

where $\hat{H} = \hat{H}^\dagger$ denotes the Hamiltonian and the density operator $\hat{\rho}(t)$ describes the quantum state of the system at time t. For pure states, the von-Neumann equation reduces to the Schrödinger equation, which describes the time evolution of the wave function $|\psi(t)\rangle$:

$$i\hbar\frac{\partial}{\partial t}|\psi(t)\rangle = \hat{H}|\psi(t)\rangle. \tag{3.61}$$

The density operator or wave function is assumed to be normalized at $t = 0$ with a condition $\mathrm{Tr}[\hat{\rho}(0)] = 1$ or $\langle\psi(0)|\psi(0)\rangle = 1$. Since the time evolution described by Eq. (3.60) or (3.61) is unitary, the normalization condition is preserved in time: $\mathrm{Tr}[\hat{\rho}(t)] = 1$ or $\langle\psi(t)|\psi(t)\rangle = 1$ $(t > 0)$.

The density operator leads to the expectation value of an arbitrary operator $\hat{\Omega}(\hat{a}, \hat{a}^\dagger)$ at time t, i.e.,

$$\langle\hat{\Omega}(t)\rangle = \mathrm{Tr}[\hat{\rho}(t)\hat{\Omega}]. \tag{3.62}$$

Using the general relation (3.42), one can translate Eq. (3.62) into the phase-space averaged form, in which the Weyl symbol of $\hat{\Omega}$, i.e., $\Omega_W(\boldsymbol{\alpha}, \boldsymbol{\alpha}^*)$, is weighted with the time-dependent Wigner function $W(\boldsymbol{\alpha}, \boldsymbol{\alpha}^*, t) = [\hat{\rho}(t)]_W(\boldsymbol{\alpha}, \boldsymbol{\alpha}^*)$:

$$\langle\hat{\Omega}(t)\rangle = \int d\boldsymbol{\alpha}d\boldsymbol{\alpha}^*\Omega_W(\boldsymbol{\alpha}, \boldsymbol{\alpha}^*)W(\boldsymbol{\alpha}, \boldsymbol{\alpha}^*, t). \tag{3.63}$$

In this representation, the dynamics of the system are entirely represented through the time evolution of the classical distribution function in the phase space. Due to the normalization condition $\mathrm{Tr}[\hat{\rho}(0)] = 1$, the Wigner function is normalized at $t = 0$ as follows:

$$\int d\boldsymbol{\alpha}d\boldsymbol{\alpha}^* W(\boldsymbol{\alpha}, \boldsymbol{\alpha}^*, 0) = 1. \tag{3.64}$$

The unitarity of dynamics says that this condition must be preserved under the time evolution generated by Eq. (3.60).

To derive an equation of motion for the Wigner function, let us make the Wigner–Weyl transform of the von-Neumann equation (3.60). The result is given by

$$\begin{aligned} i\hbar\frac{\partial W}{\partial t} &= \{H_W, W\}_{\mathrm{M.B.}} \\ &= 2H_W\sinh\left[\frac{1}{2}\Lambda_c\right]W. \end{aligned} \tag{3.65}$$

Here, $H_W = (\hat{H})_W$ is the Weyl symbol of the Hamiltonian. This equation is linear in W, and the Moyal-bracket part in the righthand side typically involves complicated differentials with respect to the phase-space variables. If we have an explicit form of the Wigner function for any t, which satisfies Eq. (3.65) exactly, the full quantum dynamics of quantum states and operator expectation values are completely described.

3.3.1 Truncated-Wigner Approximation

The full information of the quantum dynamics is encoded in the Wigner function $W(\boldsymbol{\alpha}, \boldsymbol{\alpha}^*, t)$, which is obtained as a solution of Eq. (3.65). Nevertheless, solving the time-evolution Eq. (3.65) and determining $W(\boldsymbol{\alpha}, \boldsymbol{\alpha}^*, t)$ with no approximation is generally hard even for small systems having a few degrees of freedom.

When the system is near a semiclassical limit, it is allowed to reduce the difficulty in solving the time evolution by using a semiclassical expansion. To illustrate our idea, let us formally expand the righthand side of Eq. (3.65) in the symplectic operator Λ_c:

$$i\hbar\frac{\partial W}{\partial t} = H_W \Lambda_c W + \frac{1}{3!2^2} H_W \Lambda_c^3 W + \frac{1}{5!2^4} H_W \Lambda_c^5 W + \cdots . \tag{3.66}$$

If we truncate higher-order terms of order $O(\Lambda_c^3)$ from the expansion series, then the time evolution of the Wigner function is effectively generated by the classical Liouville equation

$$i\hbar\frac{\partial W}{\partial t} \approx \{H_W, W\}_{\text{P.B.}}. \tag{3.67}$$

Within Eq. (3.67), the Wigner function is conserved along characteristic trajectories, which are solutions of the classical Hamilton equation:

$$i\hbar\frac{\partial \alpha_{\text{cl},j}}{\partial t} = \frac{\partial H_W}{\partial \alpha^*_{\text{cl},j}}, \quad i\hbar\frac{\partial \alpha^*_{\text{cl},j}}{\partial t} = -\frac{\partial H_W}{\partial \alpha_{\text{cl},j}}. \tag{3.68}$$

In classical statistical mechanics, this property is known as the Liouville theorem [2]. Using this theorem, we find that the quantum average $\langle\hat{\Omega}(t)\rangle$ reduces to a semiclassical form

$$\langle\hat{\Omega}(t)\rangle \approx \int d\boldsymbol{\alpha}_0 d\boldsymbol{\alpha}_0^* W_0(\boldsymbol{\alpha}_0, \boldsymbol{\alpha}_0^*) \Omega_W[\boldsymbol{\alpha}_{\text{cl}}(\boldsymbol{\alpha}_0, \boldsymbol{\alpha}_0^*, t), \boldsymbol{\alpha}_{\text{cl}}^*(\boldsymbol{\alpha}_0, \boldsymbol{\alpha}_0^*, t)]. \tag{3.69}$$

This semiclassical formula is constructed from two ingredients: the classical Hamilton trajectory $\boldsymbol{\alpha}_{\text{cl}}(\boldsymbol{\alpha}_0, \boldsymbol{\alpha}_0^*, t)$ starting from a point $\boldsymbol{\alpha}_0$ and the Wigner function $W_0(\boldsymbol{\alpha}_0, \boldsymbol{\alpha}_0^*) = [\hat{\rho}(0)]_W(\boldsymbol{\alpha}_0, \boldsymbol{\alpha}_0^*)$ for the initial density operator. Usually, obtaining these is much simpler than directly solving Eq. (3.65). This approximation is called the TWA [5, 9].

Equation (3.69) says that the initial classical field $\boldsymbol{\alpha}_0$ is distributed over the phase space according to the Wigner function of the initial quantum state. Within the TWA, the initial conditions of the classical dynamics fluctuate around a mean configuration, whereas the time evolution itself is entirely deterministic. This *randomness* of the initial configurations describes a leading-order correction to the mean-field solution of dynamics due to quantum fluctuations [5, 11, 14]. Indeed, the mean-field result

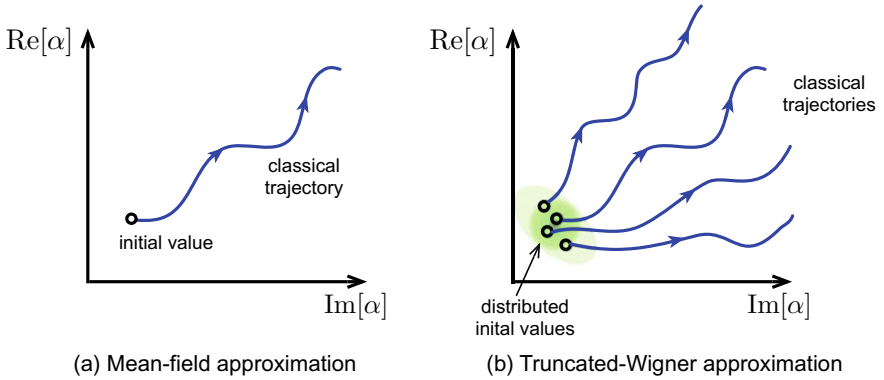

Fig. 3.3 Schematic picture of the **a** MFA and **b** TWA. The vertical and horizontal axes indicate the phase-space variable α. Each line represents the solution of the Hamilton equation

can be obtained if we formally neglect the width of the Wigner function. Then, the classical field evolves from a fixed configuration $\alpha_{\mathrm{cl},j}(t=0) = \langle \hat{a}_j \rangle$. In Fig. 3.3, we show the difference between the MFA and TWA schematically. It should be emphasized that since the Wigner function is not positive definite, it is not always appropriate to interpret each trajectory as a randomized sample from a well-defined probability distribution (see also Ref. [5]). Nevertheless, such a rough picture is often useful, and effectively valid for some cases where we are able to find an appropriate Gaussian distribution to approximate the exact Wigner function within the same accuracy of TWA (for details of the Gaussian approximation, see Chap. 5).

We note that the classical field scales with a square root of the mode occupancy n_{ocp}, so that the expansion in Λ_c is characterized by the inverse of n_{ocp}. For the Bose–Hubbard model, n_{ocp} is equal to the filling factor per site. It is known that the TWA is asymptotically exact at short times, and the valid timescale of the semiclassical approximation becomes longer for larger n_{ocp} (see also Ref. [5]). Moreover, if the system is linear or non-interacting, the semiclassical approximation then becomes exact because the higher-order terms exactly vanish. Usually, the TWA offers a good approach for systems where fluctuations are small or the Hamiltonian has a weak non-linearity. Indeed, a small non-linearity implies a small error of the truncation as seen in Eq. (3.66).

3.3.2 Semiclassical Approximation in Phase-Space Path Integrals

The method of characteristic we presented above, i.e., the Liouville theorem is a straightforward way to derive the TWA. There is another approach to derive the same result: this approach is made through a phase-space path-integral representation of

the quantum expectation values [40]. For simplicity, we restrict ourselves to the single-mode case in what follows.

Our starting point is the Heisenberg operator associated with the unitary time-evolution operator $\hat{\mathcal{U}}(t, t_0)$:

$$\hat{\Omega}_{t_0}(t) = \hat{\mathcal{U}}^{\dagger}(t, t_0)\hat{\Omega}(t)\hat{\mathcal{U}}(t, t_0), \tag{3.70}$$

where the foot index indicates the time, at which $\hat{\Omega}_{t_0}(t)$ coincides with the Schrödinger representation $\hat{\Omega}(t)$. In addition, we take into account the explicit dependence of the Schrödinger representation on time. Using the Heisenberg representation, the quantum expectation value of $\hat{\Omega}(t)$ with $\hat{\rho}(t) = \hat{\mathcal{U}}(t, t_0)\hat{\rho}_0\hat{\mathcal{U}}^{\dagger}(t, t_0)$ reads

$$\langle\hat{\Omega}(t)\rangle = \mathrm{Tr}\left[\hat{\rho}(t_0)\hat{\Omega}_{t_0}(t)\right]. \tag{3.71}$$

The next step is to transform this into the phase-space representation form. Using Eq. (3.42), it reads

$$\langle\hat{\Omega}(t)\rangle = \int \frac{d^2\alpha_0}{\pi} W(\alpha_0, t_0)[\hat{\Omega}_{t_0}(t)]_W(\alpha_0), \tag{3.72}$$

where $W(t_0) = [\hat{\rho}(t_0)]_W$. It is easily confirmed that the time-dependent Weyl symbol $[\hat{\Omega}_{t_0}(t)]_W(\alpha_0)$ is linearly related with the one at time t_0:

$$[\hat{\Omega}_{t_0}(t)]_W(\alpha_0) = \int \frac{d^2\alpha}{\pi} \Omega_W(\alpha, t) U_W(\alpha, t; \alpha_0, t_0), \tag{3.73}$$

where $U_W(\alpha, t; \alpha_0, t_0)$ is given by

$$\begin{aligned} U_W(\alpha, t; \alpha_0, t_0) = \int \frac{d^2\beta d^2\beta_0}{\pi^2} e^{-\alpha\beta^* + \alpha^*\beta} e^{-\alpha_0\beta_0^* + \alpha_0^*\beta_0} \\ \times \mathrm{Tr}[\hat{D}^{\dagger}(\beta)\hat{\mathcal{U}}(t, t_0)\hat{D}^{\dagger}(\beta_0)\hat{\mathcal{U}}^{\dagger}(t, t_0)]. \end{aligned} \tag{3.74}$$

Thus, the expectation value is expressed as

$$\langle\hat{\Omega}_{t_0}(t)\rangle = \int \frac{d^2\alpha d^2\alpha_0}{\pi^2} \Omega_W(\alpha, t) U_W(\alpha, t; \alpha_0, t_0) W(\alpha_0, t_0). \tag{3.75}$$

The two point function $U_W(\alpha, t; \alpha_0, t_0)$ can be regarded as a propagator connecting the initial and end points of the time evolution in the phase space.

Let us explain the basic and important properties of the phase-space propagator $U_W(\alpha, t; \alpha_0, t_0)$. Due to the unitarity of the time evolution operator, there is a recursion relation for $t_0 \leq t_1 \leq t$:

$$\hat{\mathcal{U}}(t,t_1)\hat{\mathcal{U}}(t_1,t_0)=\hat{\mathcal{U}}(t,t_0). \tag{3.76}$$

Inserting this relation into each interval of the time evolution, we arrive at an iterative relation for $t_0 \le t_1 \le t_2 \le \cdots \le t_{N-1} \le t_N \le t$:

$$\hat{\mathcal{U}}(t,t_N)\hat{\mathcal{U}}(t_N,t_{N-1})\cdots\hat{\mathcal{U}}(t_2,t_1)\hat{\mathcal{U}}(t_1,t_0)=\hat{\mathcal{U}}(t,t_0). \tag{3.77}$$

There are similar relations for the phase-space propagator. Indeed, through direct calculations, one can confirm that the propagator fulfills

$$U_W(\alpha,t;\alpha_0,t_0)=\int\frac{d^2\alpha_1}{\pi}U_W(\alpha,t;\alpha_1,t_1)U_W(\alpha_1,t_1;\alpha_0,t_0) \tag{3.78}$$

for $t_0 \le t_1 \le t$. Using this relation iteratively, we arrive at a phase-space representation of the iterative relation

$$U_W(\alpha,t;\alpha_0,t_0)=\int\prod_{n=1}^{N}\frac{d^2\alpha_n}{\pi}U_W(\alpha,t;\alpha_N,t_N)U_W(\alpha_N,t_N;\alpha_{N-1},t_{N-1})\cdots \times U_W(\alpha_2,t_2;\alpha_1,t_1)U_W(\alpha_1,t_1;\alpha_0,t_0). \tag{3.79}$$

If the number of steps N is so large that the time interval is infinitesimal, Eq. (3.75) can be rewritten into a phase-space path-integral form. Notice that the boundary of the path integral is now not fixed by specific phase-space points. In particular, the initial point is weighted with the initial Wigner function $W(\alpha_0,t_0)$.

Let us determine the phase-space propagator for the infinitesimal interval. For the purpose, we use the fact that we also have a similar relation to Eq. (3.73) for the Wigner function:

$$W(\alpha,t)=\int\frac{d^2\alpha_0}{\pi}U_W(\alpha,t;\alpha_0,t_0)W(\alpha_0,t_0). \tag{3.80}$$

For a small interval between t and $t+\Delta t$, the Wigner function propagates in phase space and time and satisfies

$$W(\alpha,t+\Delta t)=\int\frac{d^2\alpha_0}{\pi}U_W(\alpha,t+\Delta t;\alpha_0,t)W(\alpha_0,t). \tag{3.81}$$

To obtain the interval propagator $U_W(\alpha,t+\Delta t;\alpha_0,t)$, we consider the von-Neumann equation, which is discretized in time for the interval time step:

$$\hat{\rho}(t+\Delta t)=\hat{\rho}(t)+\frac{\Delta t}{i\hbar}[\hat{H}\hat{\rho}(t)-\hat{\rho}(t)\hat{H}]. \tag{3.82}$$

From Eq. (3.82), we obtain the following expression:

$$W(\alpha, t+\Delta t) = W(\alpha, t) + \int \frac{d^2\alpha_0}{\pi}\frac{d^2\sigma}{\pi} e^{\sigma^*(\alpha-\alpha_0)-\sigma(\alpha^*-\alpha_0^*)} \times \left\{1 - \frac{\Delta t}{i\hbar}\sum_{n=0}^{\infty}\frac{1}{2^{2n}}\sum_{s_1,s_2=0}^{s_1+s_2=2n+1}\frac{H_W^{(s_1,s_2)}(\alpha_0)}{s_1!s_2!}(\sigma)^{s_1}(\sigma^*)^{s_2}\right\} W(\alpha_0, t), \tag{3.83}$$

where $H_W^{(s_1,s_2)}(\alpha)$ implies

$$H_W^{(s_1,s_2)}(\alpha) = \frac{\partial^{s_1+s_2} H_W(\alpha)}{\partial\alpha^{s_1}\partial(\alpha^*)^{s_2}}. \tag{3.84}$$

Comparing Eqs. (3.81) and (3.83), we have the infinitesimal propagator in the phase space

$$U_W(\alpha, t+\Delta t; \alpha_0, t) = \int \frac{d^2\sigma}{\pi} e^{\sigma^*(\alpha-\alpha_0)-\sigma(\alpha^*-\alpha_0^*)} \times \left\{1 - \frac{\Delta t}{i\hbar}\sum_{n=0}^{\infty}\frac{1}{2^{2n}}\sum_{s_1,s_2=0}^{s_1+s_2=2n+1}\frac{H_W^{(s_1,s_2)}(\alpha_0)}{s_1!s_2!}(\sigma)^{s_1}(\sigma^*)^{s_2}\right\}. \tag{3.85}$$

Notice that α and α_0 correspond to the mean-field degrees of freedom, whereas σ describes the quantum fluctuations.

Equation (3.85) has no approximation and actually contains the full information of the exact quantum dynamics. If we neglect higher-order terms with respect to the quantum fluctuations, we arrive at the TWA once again. Up to the leading order of the σ-field, the infinitesimal propagator turns out to be a delta function:

$$\begin{aligned} U_W(\alpha, t+\Delta t; \alpha_0, t) &\approx \int \frac{d^2\sigma}{\pi} e^{\sigma^*(\alpha-\alpha_0)-\sigma(\alpha^*-\alpha_0^*)}\left\{1 - \frac{\Delta t}{i\hbar}\frac{\partial H_W}{\partial\alpha_0^*}\sigma^* - \frac{\Delta t}{i\hbar}\frac{\partial H_W}{\partial\alpha_0}\sigma\right\} \\ &\approx \int \frac{d^2\sigma}{\pi}\exp\left[\sigma^*\left(\alpha-\alpha_0 - \frac{\Delta t}{i\hbar}\frac{\partial H_W}{\partial\alpha_0^*}\right) - \sigma\left(\alpha^*-\alpha_0^* + \frac{\Delta t}{i\hbar}\frac{\partial H_W}{\partial\alpha_0}\right)\right] \\ &= \pi\,\delta\left(\alpha-\alpha_0 - \frac{\Delta t}{i\hbar}\frac{\partial H_W}{\partial\alpha_0^*}\right)\delta\left(\alpha^*-\alpha_0^* + \frac{\Delta t}{i\hbar}\frac{\partial H_W}{\partial\alpha_0}\right). \end{aligned} \tag{3.86}$$

Using this result, we finally obtain the TWA formula ($\Delta t \to 0$):

$$\begin{aligned} \langle\hat{\Omega}_{t_0}(t)\rangle &\approx \int \frac{d^2\alpha d^2\alpha_0}{\pi^2}\prod_{n=1}^{N}\frac{d^2\alpha_n}{\pi}\Omega_W(\alpha, t)\prod_{m=1}^{N+1}\pi\,\delta^{(2)}\left(\alpha_m - \alpha_{m-1} - \frac{\Delta t}{i\hbar}\frac{\partial H_W}{\partial\alpha_{m-1}^*}\right) W(\alpha_0, t_0) \\ &= \int d\alpha_0 d\alpha_0^*\,\Omega_W[\alpha_{\rm cl}(\alpha_0, t)]W(\alpha_0, t_0) \end{aligned} \tag{3.87}$$

where $\alpha_{N+1} = \alpha$ and $\alpha_{\rm cl}(\alpha_0, t)$ is the solution of the single-mode Hamilton equation starting from $\alpha = \alpha_0$ at time t_0.

Within the leading order, the time evolution is entirely deterministic and described within the classical Hamilton equation. Then, the quantum fluctuation effects are

encoded only in the Wigner function at time t_0. It is worth noting that the higher-order corrections of the fluctuations give rise to infinitesimal jumps of each classical trajectory and lead to perturbative modifications of the TWA expectation value, which can be regarded as non-linear responses to the jumps [5, 14]. However, we do not take into account these higher-order contributions in this Thesis.

References

1. E.P. Wigner, Phys. Rev. **40**, 749 (1932)
2. M. Hillery, R.F. O'Connell, M.O. Scully, E.P. Wigner, Phys. Rep. **106**, 121 (1984)
3. D. Walls, G. Milburn, *Quantum Optics* (Springer, Berlin, 1994)
4. C.W. Gardiner, P. Zoller, *Quantum Noise: a Handbook of Markovian and Non-Markovian Quantum Stochastic Methods with Applications to Quantum Optics* (Springer, Berlin, 2004)
5. A. Polkovnikov, Ann. Phys. **325**, 1790 (2010)
6. H. Weyl, Z. Phys. **46**, 1 (1927)
7. J. Moyal, Proc. Camb. Philos. Soc. **45**, 99 (1949)
8. R.J. Glauber, Phys. Rev. Lett. **10**, 84 (1963)
9. P.B. Blakie, A.S. Bradley, M.J. Davis, R.J. Ballagh, C.W. Gardiner, Adv. Phys. **57**, 363 (2008)
10. A. Polkovnikov, S. Sachdev, S.M. Girvin, Phys. Rev. A **66**, 053607 (2002)
11. A. Polkovnikov, Phys. Rev. A **68**, 033609 (2003)
12. L. Isella, J. Ruostekoski, Phys. Rev. A **72**, 011601(R) (2005)
13. A.K. Tuchman, C. Orzel, A. Polkovnikov, M.A. Kasevich, Phys. Rev. A **74**, 051601(R) (2006)
14. A. Polkovnikov, Phys. Rev. A **68**, 053604 (2003)
15. A. Polkovnikov, D.-W. Wang, Phys. Rev. Lett. **93**, 070401 (2004)
16. L. Mathey, A. Polkovnikov, Phys. Rev. A **80**, 041601(R) (2009)
17. L. Mathey, A. Polkovnikov, Phys. Rev. A **81**, 033605 (2010)
18. L. Mathey, K.J. Günter, J. Dalibard, A. Polkovnikov, Phys. Rev. A **95**, 053630 (2017)
19. J. Dziarmaga, M. Tylutki, W.H. Zurek, Phys. Rev. B **86**, 144521 (2012)
20. I.S. Landea, N. Nessi, Phys. Rev. A **91**, 063601 (2015)
21. K. Fujimoto, R. Hamazaki, M. Ueda, Phys. Rev. Lett. **120**, 073002 (2018)
22. J.G. Cosme, Phys. Rev. A **97**, 043610 (2018)
23. M. Kunimi, I. Danshita, unpublished
24. J. Schachenmayer, A. Pikovski, A.M. Rey, Phys. Rev. X **5**, 011022 (2015)
25. J. Schachenmayer, A. Pikovski, A.M. Rey, New J. Phys. **17**, 065009 (2015)
26. S.M. Davidson, A. Polkovnikov, Phys. Rev. Lett. **114**, 045701 (2015)
27. J. Wurtz, A. Polkovnikov, D. Sels, Ann. Phys. **395**, 341 (2018)
28. A.M. Rey, A.V. Gorshkov, C.V. Kraus, M.J. Martin, M. Bishof, M.D. Swallows, X. Zhang, C. Benko, J. Ye, N.D. Lemke, A.D. Ludlow, Ann. Phys. **340**, 311 (2014)
29. G. Kordas, D. Witthaut, S. Wimberger, Ann. Phys. (Berlin) **527**, 619 (2015)
30. A. Johnson, S.S. Szigeti, M. Schemmer, I. Bouchoule, Phys. Rev. A **96**, 013623 (2017)
31. F. Vicentini, F. Minganti, R. Rota, G. Orso, C. Ciuti, Phys. Rev. A **97**, 013853 (2018)
32. J.G. Cosme, C. Georges, A. Hemmerich, L. Mathey, Phys. Rev. Lett. **121**, 153001 (2018)
33. A. Altland, V. Gurarie, T. Kriecherbauer, A. Polkovnikov, Phys. Rev. A **79**, 042703 (2009)
34. A. Piñeiro Orioli, A. Safavi-Naini, M.L. Wall, A.M. Rey, Phys. Rev. A **96**, 033607 (2017)
35. D. Raventós, T. Graß, B. Juliá-Díaz, M. Lewenstein, Phys. Rev. A **97**, 052310 (2018)
36. S.M. Davidson, D. Sels, A. Polkovnikov, Ann. Phys. **384**, 128 (2017)
37. T. Scaffidi, E. Altman, Phys. Rev. B **100**, 155128 (2019)
38. M. Schmitt, D. Sels, S. Kehrein, A. Polkovnikov, Phys. Rev. B **99**, 134301 (2019)
39. Y. Takasu, T. Yagami, H. Asaka, Y. Fukushima, K. Nagao, S. Goto, I. Danshita, Y. Takahashi, arXiv:2002.12025 [cond-mat.quant-gas]

40. B. Berg, L.I. Plimak, A. Polkovnikov, M.K. Olsen, M. Fleischhauer, W.P. Schleich, Phys. Rev. A **80**, 033624 (2009)
41. A. Altland, B.D. Simons, *Condensed Matter Field Theory*, 2nd edn. (Cambridge University Press, Cambridge, 2010)

Chapter 4
Response of the Higgs Mode in a Three Dimensional Optical Lattice

Abstract In this chapter, we investigate responses of the Higgs mode in strongly-correlated Bose gases in a three-dimensional optical lattice. Our goal is to examine the detectability of the long-lived Higgs modes in real experiments of ultracold gases. In Sect. 4.1, we discuss time-dependent external perturbations to excite the Higgs mode in the optical lattice and formulate response functions within the linear-response theory. In Sect. 4.2, we generalize the effective model presented in Chap. 2 for the high-filling limit into low-filling cases, and derive interaction vertices among collective modes by identifying higher-order contributions of the Holstein–Primakoff expansion. In Sect. 4.3, we calculate the response functions using Feynman's diagrammatic perturbation theory for a finite-temperature Green's function. In Sect. 4.4, we numerically evaluate the analytical expressions obtained from the perturbative expansion and show that these exhibit a characteristic signal associated with the Higgs mode. In addition, we deal with a harmonic trap effect on the response functions within a local density approximation and discuss the detectability of the Higgs mode in typical experiments.

4.1 Linear Response Theory for External Modulations

Throughout this chapter, we set $\hbar = k_{\mathrm{B}} = 1$. For simplicity, we omit the *hat* symbols from operators.

4.1.1 Kinetic Energy Modulations

The Higgs mode is the collective excitation associated with fluctuations of the order-parameter amplitude around its equilibrium configuration. A direct way of exciting this mode in cold atomic experiments is to modulate the condensate density $|\Psi|^2$ by using the technique of periodic optical-lattice-amplitude modulation [1, 2]. For the system described by the Bose–Hubbard model, atoms look at the periodic modulation

K. Nagao, *Fluctuations and Non-Equilibrium Phenomena in Strongly-Correlated Ultracold Atoms*, Springer Theses, https://doi.org/10.1007/978-981-15-7171-8_4

as a hopping strength modulation, i.e., a kinetic energy modulation (for details of this technique, see Refs. [3–5]). In Ref. [2], the experimental group has achieved a rather small amplitude modulation, whose vibration amplitude is approximately 3% of the initial depth. Therefore, the system is weakly perturbed during the modulation time, so that one can describe responses to the modulations by the linear response functions.

To get the linear response function to the J modulation, let us suppose that the system is in a thermal equilibrium state with the inverse temperature $\beta = T^{-1}$ at $t \to -\infty$. When we add a small and periodic modulation to the hopping strength J slowly such that $J \to [1 + \Delta_J(t)]J$, where $\Delta_J(t) = \delta_J \cos(\omega t)$ and δ_J is sufficiently small, the perturbed system can be described by the following Hamiltonian with an oscillating perturbation term:

$$\mathcal{H}_{\mathrm{BH}} \to \mathcal{H}_{\mathrm{BH}} + \Delta_J(t) K,$$

where $K \equiv -J \sum_{\langle ij \rangle} a_i^\dagger a_j$ expresses the kinetic energy of the Bose–Hubbard model. The perturbation comes from the weak coupling with the external field. The instantaneous change of the total energy by such a modulation is proportional to the instantaneous quantum mechanical average of the kinetic energy [3, 5]. Therefore, the response of the system is characterized only by the kinetic energy response. The corresponding response function turns out to be the following K-to-K response function [4, 6]

$$D^{\mathrm{R}}_{KK}(t - t') = -i\Theta(t - t') \left\langle \left[K(t), K(t') \right] \right\rangle_{\mathrm{eq}}, \tag{4.1}$$

where $\Theta(t)$ is the step function defined by

$$\Theta(t) = \begin{cases} 1 & \text{for } t > 0, \\ 0 & \text{for } t < 0. \end{cases} \tag{4.2}$$

$K(t) = e^{i\mathcal{H}_{\mathrm{BH}} t} K e^{-i\mathcal{H}_{\mathrm{BH}} t}$ denotes the Heisenberg representation of the kinetic-energy operator. The bracket $\langle \cdots \rangle_{\mathrm{eq}} \equiv \mathrm{Tr}(\mathrm{e}^{-\beta \mathcal{H}_{\mathrm{BH}}} \cdots)/\mathrm{Tr}\ \mathrm{e}^{-\beta \mathcal{H}_{\mathrm{BH}}}$ means the thermal average with the normalized canonical Gibbs distribution. The superscript character "R" indicates that D^{R}_{KK} measures a retarded correlation between different times and satisfies the causality law.

Transforming Eq. (4.1) into the frequency space, we have the dynamical susceptibility associated with the kinetic-energy modulation. At a given ω, it is written in the form

$$\chi_{KK}(\omega) = \int_{-\infty}^{\infty} D^{\mathrm{R}}_{KK}(t) \mathrm{e}^{i\omega t} dt. \tag{4.3}$$

The imaginary part of this function gives the so called spectral function $S_{KK}(\omega) \equiv -\mathrm{Im}\,[\chi_{KK}(\omega)]$, which is proportional to the external energy absorbed by the system

for a finite-time period of the modulation [2, 5]. The response function or its susceptibility characterizes the resonance of the Higgs mode in experimental systems [2, 6]. The Max-Planck group has experimentally obtained $S_{KK}(\omega)$ at low frequencies by measuring the temperature increase of the system after the lattice-amplitude modulation with a fixed modulation time [2].

4.1.2 Onsite-Interaction Energy Modulations

The hopping modulation changes the condensate density periodically in time because the latter one is a function of J/U. This implies that in order to make a periodic driving of the condensate density one can take another modulation scheme, i.e., modulation of the onsite interaction energy. To our knowledge, this kind of modulation has not been discussed thus far as a probe of the Higgs mode. In this section, we identify what types of response function characterize the response to the U modulation and how one can realize such a modulation in experiments with high controllability. Some detailed relationships between the response function and absorbed energy under the U modulation are presented in Appendix A.

Let us consider a temporal and sufficiently weak driving of U. This is described by $U \to [1 + \Delta_U(t)]U$, where $\Delta_U(t) = \delta_U \cos(\omega t)$ and δ_U is sufficiently small. The Hamiltonian of the perturbed system is given by

$$\mathcal{H}_{\mathrm{BH}} \to \mathcal{H}_{\mathrm{BH}} + \Delta_U(t) O.$$

Here, $O \equiv \frac{U}{2} \sum_i (n - n_0)^2$ is the onsite-interaction energy of the system. It is shown in Appendix A that the instantaneous change rate of the total energy is proportional to the quantum mechanical average of O. Within the linear response regime, the resulting response can be characterized by the following O-to-O-type response function

$$D^{\mathrm{R}}_{OO}(t - t') = -i\Theta(t - t') \left\langle \left[O(t), O(t') \right] \right\rangle_{\mathrm{eq}}, \tag{4.4}$$

where $O(t) = e^{i\mathcal{H}_{\mathrm{BH}}t} O e^{-i\mathcal{H}_{\mathrm{BH}}t}$. For this function, one can define the dynamical susceptibility of the U modulation,

$$\chi_{OO}(\omega) = \int_{-\infty}^{\infty} D^{\mathrm{R}}_{OO}(t) \mathrm{e}^{i\omega t} dt. \tag{4.5}$$

As in the case of the J modulation, its imaginary part is nothing else but the spectral function $S_{OO}(\omega) = -\mathrm{Im}\left[\chi_{OO}(\omega)\right]$ for the U modulation, which is proportional to the absorption energy under the external driving (see also Appendix A). We expect that this type of driving can also be utilized as an experimental probe of the Higgs mode and leads to a Higgs resonance in the spectral function.

Thanks to the recent developments of the experimental technology in atomic, molecular, and optical (AMO) physics, one has been allowed to control the s-wave scattering length, i.e., the strength of the onsite interaction, by utilizing highly controlled optical techniques. The experimental techniques include *the optical Feshbach resonance* [7–9] and *the optically induced Feshbach resonance* [10, 11]. In contrast to the conventional magnetic Feshbach resonance, these techniques allow for fast temporal modulation of U with a frequency on the order of 1 to 10 kHz, which is supposed to be comparable to a typical resonance frequency (or mass) of the Higgs mode in the cold-atomic system.

4.2 Interactions Between Collective Modes

The main purpose of this chapter is to analyze the dynamical susceptibilities (4.3) and (4.5), respectively for the grand-canonical three-dimensional (3D) Bose–Hubbard model (2.20) in the strongly-interacting regime in which the Higgs and NG modes can appear as dominant low-energy excitations. To do that, we utilize the effective pseudospin-1 mapping explained in Chap. 2 for simplifying the original Bose–Hubbard model. In particular, in order to deal with an experimental situation where the atomic occupation is tuned to unity, the modified effective model (2.45) is mainly used. An entirely similar analysis based on the high-filling effective model is also performed to compare two results at different fillings (see Sect. 4.4.1).

In this section, before going to our main analysis of the susceptibilities, we derive an approximate *spin-wave* Hamiltonian, which describes the mean-field dispersion relations of the Higgs and NG modes and interactions among them. To perform that, we apply the Holstein–Primakoff (HP) expansion to the effective pseudospin-1 model at low fillings (2.45). Although a similar expansion up to the quadratic order (no interaction) was discussed by Huber et al. in Ref. [12], we present its derivation in details because our analysis successfully gives higher-order corrections beyond their results and deals with transitions or mixing between quadratic-order eigenstates for the linearized Hamiltonian in fluctuations. As we will see below, the subsequent corrections give rise to a finite lifetime of the collective modes.

4.2.1 Fluctuations from the Mean-Field Ground State

Let us start again from considering fluctuations around the mean-field superfluid state derived from the Gutzwiller ansatz in Chap. 2. Substituting the canonical transformation (2.55) into the low-filling effective model (2.45), we obtain the Hamiltonian describing the collective fluctuations around the mean field. The resulting Hamiltonian can be separated into five parts:

$$\mathcal{H}_{\rm eff} = \mathcal{H}_{\rm eff}^{(0)} + \mathcal{H}_{\rm eff}^{(1)} + \mathcal{H}_{\rm eff}^{(2)} + \mathcal{H}_{\rm eff}^{(3)} + \mathcal{H}_{\rm eff}^{(4)}, \tag{4.6}$$

where each term contained in $\mathcal{H}_{\rm eff}^{(l)}$ ($l = 0, 1, 2, 3, 4$) has l numbers of the fluctuation operator $b_{m,i}^{\dagger}$, $b_{m,i}$ ($m = 1, 2$). The explicit forms of $\mathcal{H}_{\rm eff}^{(0)}$ and $\mathcal{H}_{\rm eff}^{(1)}$ are given by

$$\begin{aligned}
\mathcal{H}_{\rm eff}^{(0)} =& \sum_{\langle ij\rangle} \frac{1}{z} A_0 b_{0,i}^{\dagger} b_{0,i} b_{0,j}^{\dagger} b_{0,j} + \sum_i \tilde{A}_0 b_{0,i}^{\dagger} b_{0,i}, \\
\mathcal{H}_{\rm eff}^{(1)} =& \sum_{\langle ij\rangle} \frac{1}{z} A_1 b_{0,i}^{\dagger} b_{0,i} b_{1,j}^{\dagger} b_{0,j} + \sum_{\langle ij\rangle} \frac{1}{z} B_1 b_{0,i}^{\dagger} b_{0,i} b_{2,j}^{\dagger} b_{0,j} \\
&+ \sum_i \tilde{A}_1 b_{1,i}^{\dagger} b_{0,i} + \sum_i \tilde{B}_1 b_{2,i}^{\dagger} b_{0,i} + \text{H.c.}.
\end{aligned}$$

The quadratic term $\mathcal{H}_{\rm eff}^{(2)}$ is presented by

$$\begin{aligned}
\mathcal{H}_{\rm eff}^{(2)} =& \sum_{\langle ij\rangle} \frac{1}{2z} A_2 b_{0,i}^{\dagger} b_{0,i} b_{1,j}^{\dagger} b_{1,j} + \sum_{\langle ij\rangle} \frac{1}{z} B_2 b_{0,i}^{\dagger} b_{0,i} b_{1,j}^{\dagger} b_{2,j} \\
&+ \sum_{\langle ij\rangle} \frac{1}{z} D_2 b_{1,i}^{\dagger} b_{0,i} b_{1,j}^{\dagger} b_{0,j} + \sum_{\langle ij\rangle} \frac{1}{2z} E_2 b_{1,i}^{\dagger} b_{0,i} b_{0,j}^{\dagger} b_{1,j} \\
&+ \sum_{\langle ij\rangle} \frac{1}{z} F_2 b_{1,i}^{\dagger} b_{0,i} b_{0,j}^{\dagger} b_{2,j} + \sum_{\langle ij\rangle} \frac{1}{z} G_2 b_{1,i}^{\dagger} b_{0,i} b_{2,j}^{\dagger} b_{0,j} \\
&+ \sum_{\langle ij\rangle} \frac{1}{z} H_2 b_{0,i}^{\dagger} b_{2,i} b_{0,j}^{\dagger} b_{2,j} + \sum_{\langle ij\rangle} \frac{1}{2z} I_2 b_{0,i}^{\dagger} b_{2,i} b_{2,j}^{\dagger} b_{0,j} \\
&+ \sum_i \frac{1}{2} \tilde{A}_2 b_{1,i}^{\dagger} b_{1,i} + \sum_i \tilde{B}_2 b_{1,i}^{\dagger} b_{2,i} + \sum_i \frac{1}{2} \tilde{C}_2 b_{2,i}^{\dagger} b_{2,i} + \text{H.c.}.
\end{aligned}$$

Moreover, the remaining terms $\mathcal{H}_{\rm eff}^{(3)}$ and $\mathcal{H}_{\rm eff}^{(4)}$ are given by

$$\begin{aligned}
\mathcal{H}_{\rm eff}^{(3)} =& \sum_{\langle ij\rangle} \frac{1}{z} A_3 b_{1,i}^{\dagger} b_{1,i} b_{1,j}^{\dagger} b_{0,j} + \sum_{\langle ij\rangle} \frac{1}{z} B_3 b_{1,i}^{\dagger} b_{1,i} b_{2,j}^{\dagger} b_{0,j} \\
&+ \sum_{\langle ij\rangle} \frac{1}{z} C_3 b_{1,i}^{\dagger} b_{0,i} b_{2,j}^{\dagger} b_{1,j} + \sum_{\langle ij\rangle} \frac{1}{z} D_3 b_{1,i}^{\dagger} b_{0,i} b_{1,j}^{\dagger} b_{2,j} \\
&+ \sum_{\langle ij\rangle} \frac{1}{z} E_3 b_{0,i}^{\dagger} b_{2,i} b_{2,j}^{\dagger} b_{1,j} + \sum_{\langle ij\rangle} \frac{1}{z} F_3 b_{0,i}^{\dagger} b_{2,i} b_{1,j}^{\dagger} b_{2,j} + \text{H.c.}, \\
\mathcal{H}_{\rm eff}^{(4)} =& \sum_{\langle ij\rangle} \frac{1}{2z} A_4 b_{1,i}^{\dagger} b_{1,i} b_{1,j}^{\dagger} b_{1,j} + \sum_{\langle ij\rangle} \frac{1}{z} B_4 b_{1,i}^{\dagger} b_{2,i} b_{1,j}^{\dagger} b_{2,j} \\
&+ \sum_{\langle ij\rangle} \frac{1}{z} C_4 b_{1,i}^{\dagger} b_{2,i} b_{1,j}^{\dagger} b_{1,j} + \sum_{\langle ij\rangle} \frac{1}{2z} D_4 b_{1,i}^{\dagger} b_{2,i} b_{2,j}^{\dagger} b_{1,j} + \text{H.c.}.
\end{aligned}$$

In the above representations, the coefficients such as A_0, $\tilde{A}_0$, A_1, B_1, ... depend on J and μ through the variational parameter $\theta_{\rm mf}$. The explicit forms are complicated functions of J and μ. These are given in Appendix B. We note that $z = 2d = 6$ is the coordination number for the cubic lattice.

4.2.2 Holstein–Primakoff Expansion

As a next step, we expand $\mathcal{H}_{\rm eff}^{(l)}$ ($l = 0, 1, 2, 3, 4$) in fluctuations by use of the HP expansion (2.57) for the three-flavor bosons:

$$b_{m,i}^{\dagger} b_{0,j} \approx b_{m,i}^{\dagger} - \frac{1}{2} b_{m,i}^{\dagger} b_{1,j}^{\dagger} b_{1,j} - \frac{1}{2} b_{m,i}^{\dagger} b_{2,j}^{\dagger} b_{2,j} + \cdots .$$

We eliminate $b_{0,i}^{\dagger} b_{0,i}$ in the Hamiltonian (4.6) by using the local constraint $\sum_n b_n^{\dagger} b_n = 1$, and then substitute this expansion into the equation. A direct computation leads to the following series

$$\mathcal{H}_{\rm eff} \approx \mathcal{H}_{\rm SW}^{(0)} + \mathcal{H}_{\rm SW}^{(1)} + \mathcal{H}_{\rm SW}^{(2)} + \mathcal{H}_{\rm SW}^{(3)} + \mathcal{H}_{\rm SW}^{(4)} \cdots . \tag{4.7}$$

Each term $\mathcal{H}_{\rm SW}^{(l)}$ (for $l = 0, 1, 2, 3, 4, \ldots$) involves l collective-mode or spin-wave operators. The zeroth order term for $l = 0$ gives a constant contribution to this series. The control parameter of such an expansion is given by S^{-1}, where S is the spin magnitude of the system. In fact, each term $\mathcal{H}_{\rm SW}^{(l)}$ is of order $O(S^{2-l/2})$. In this work, in order to see the lowest order effects on the response properties to the J and U modulations, we deal with fluctuation effects on the linear response functions up to order $O(S^0)$. Keeping this point in mind, the expansion (4.7) is stopped at $l = 4$. A similar spin-wave analysis has been made for some concrete quantum-spin models by Chernyshev and Zhitomirsky in Ref. [13].

Let us look at details of the terms $\mathcal{H}_{\rm SW}^{(0)}$, $\mathcal{H}_{\rm SW}^{(1)}$, $\mathcal{H}_{\rm SW}^{(2)}$, and $\mathcal{H}_{\rm SW}^{(3)}$ in the expansion (4.7), respectively. We begin with the zeroth order term denoted by $\mathcal{H}_{\rm SW}^{(0)}$. This gives the ground state energy, which is a c-number functional obtained from the mean-field treatment with no fluctuation:

$$\mathcal{H}_{\rm SW}^{(0)} = N(A_0 + \tilde{A}_0) = N E^{\rm MF}(\theta_{\rm mf}), \tag{4.8}$$

where $E^{\rm MF}(\theta_{\rm mf})$ is Eq. (2.47) derived from the Gutzwiller ansatz (see Sect. 2.5.4). We note that N is used as the total lattice number throughout this chapter.

The leading order correction in the expansion is a linear combination of the spin-wave operators:

$$\mathcal{H}_{\rm SW}^{(1)} = \sqrt{N}(A_1 + \tilde{A}_1)(b_{1,\mathbf{0}}^{\dagger} + b_{1,\mathbf{0}}) + \sqrt{N}(B_1 + \tilde{B}_1)(b_{2,\mathbf{0}}^{\dagger} + b_{2,\mathbf{0}}). \tag{4.9}$$

This term is of order $O(S^{3/2})$. For the mean-field ground state, we can easily verify that $\mathcal{H}_{\rm SW}^{(1)} = 0$. This is consistent with the fact that at the mean-field configuration the first-order derivatives of the energy functional with respect to the variational parameters should vanish.

The quadratic term $\mathcal{H}_{\rm SW}^{(2)} = O(S)$ can be formally written in the matrix form

$$\mathcal{H}_{\rm SW}^{(2)} = \delta E_2 + \sum_{\lambda=1}^{4}\sum_{\nu=1}^{4}\sum_{\mathbf{k}\in\Lambda_0} b_{\lambda,\mathbf{k}}^{\dagger}(\mathrm{H}_{\mathbf{k}})_{\lambda\nu} b_{\nu,\mathbf{k}}, \tag{4.10}$$

where $\mathbf{b}_{\mathbf{k}} = (b_{1,\mathbf{k}}, b_{2,\mathbf{k}}, b_{3,\mathbf{k}}, b_{4,\mathbf{k}})^{\rm T}$ with $(b_{3,\mathbf{k}}, b_{4,\mathbf{k}}) = (b_{1,-\mathbf{k}}^{\dagger}, b_{2,-\mathbf{k}}^{\dagger})$ is a vector representation for the spin-wave operators. The 4×4 matrix $\mathrm{H}_{\mathbf{k}}$ acting on that vector is a matrix representation of the second-order Hamiltonian given by

$$\mathrm{H}_{\mathbf{k}} = \begin{pmatrix} f_{11}(\mathbf{k}) & f_{12}(\mathbf{k}) & g_{11}(\mathbf{k}) & g_{12}(\mathbf{k}) \\ f_{21}(\mathbf{k}) & f_{22}(\mathbf{k}) & g_{21}(\mathbf{k}) & g_{22}(\mathbf{k}) \\ g_{11}(\mathbf{k}) & g_{12}(\mathbf{k}) & f_{11}(\mathbf{k}) & f_{12}(\mathbf{k}) \\ g_{21}(\mathbf{k}) & g_{22}(\mathbf{k}) & f_{21}(\mathbf{k}) & f_{22}(\mathbf{k}) \end{pmatrix}, \tag{4.11}$$

where

$$\begin{aligned} f_{11}(\mathbf{k}) &= (A_2 + \tilde{A}_2 - 2A_0 - \tilde{A}_0 + E_2\gamma_{\mathbf{k}})/2, \\ f_{12}(\mathbf{k}) &= f_{21}(\mathbf{k}) = (B_2 + \tilde{B}_2 + F_2\gamma_{\mathbf{k}})/2, \\ f_{22}(\mathbf{k}) &= (\tilde{C}_2 - 2A_0 - \tilde{A}_0 + I_2\gamma_{\mathbf{k}})/2, \\ g_{11}(\mathbf{k}) &= D_2\gamma_{\mathbf{k}}, \\ g_{12}(\mathbf{k}) &= g_{21}(\mathbf{k}) = G_2\gamma_{\mathbf{k}}/2, \\ g_{22}(\mathbf{k}) &= H_2\gamma_{\mathbf{k}}. \end{aligned}$$

The periodic function $\gamma_{\mathbf{k}} = (\cos k_x + \cos k_y + \cos k_z)/3$ characterizes the band structure in the 3D wave-number space. At $n_0 \gg 1$, $f_{12}(\mathbf{k}) = f_{21}(\mathbf{k}) = g_{12}(\mathbf{k}) = g_{21}(\mathbf{k}) = 0$. Hence, at this limit, $\mathcal{H}_{\rm SW}^{(2)}$ has no mixing term such as $b_{1,\mathbf{k}}^{\dagger} b_{2,\mathbf{k}}$, and we can see that two quadratic parts labelled by either 1 or 2 can be entirely decoupled from each other. This feature stems from the explicit particle-hole symmetry of the effective pseudospin-1 model for $n_0 \gg 1$ (see also Sect. 2.5.2). Indeed, terms with an odd number of $b_{2,\mathbf{k}}$ are forbidden by the particle-hole symmetry at the microscopic level because an exchange between a particle $t_{1,i}$ and hole $t_{-1,i}$ leads to a change of the sign of $b_{2,\mathbf{k}}$ while such a transformation remains the sign of $b_{1,\mathbf{k}}$. On the other hand, at lower filling rates, there is no restriction to remove such cross terms.

We note that the constant part coming from the quadratic operator, $\delta E_2 = -\sum_{\mathbf{k}\in\Lambda_0}(f_{11}(\mathbf{k}) + f_{22}(\mathbf{k}))$, can be interpreted as a quantum fluctuation correction to the mean-field energy of the ground state $\mathcal{H}_{\rm SW}^{(0)}(\theta_{\rm mf}, \chi_{\rm mf})$. The detailed discussion will be presented in Sect. 4.2.4.

The cubic term $\mathcal{H}_{\rm SW}^{(3)}$, which describes interactions among three spin waves, has many non-zero terms. We can write it as

$$\mathcal{H}_{\rm SW}^{(3)}Sect. = \frac{1}{\sqrt{N}}\prod_{i=1}^{3}\sum_{\lambda_i=1}^{4}\sum_{\mathbf{k}_i\in\Lambda_0} \mathrm{C}^{(\lambda_1\lambda_2\lambda_3)}_{p_{\lambda_1}\mathbf{k}_1,p_{\lambda_2}\mathbf{k}_2,p_{\lambda_3}\mathbf{k}_3}\delta_{\mathbf{k}_1+\mathbf{k}_2+\mathbf{k}_3,\mathbf{0}}\; b_{\lambda_1,\mathbf{k}_1}b_{\lambda_2,\mathbf{k}_2}\; b_{\lambda_3,\mathbf{k}_3}, \tag{4.12}$$

where $p_\lambda = 1$ (for $\lambda = 1, 2$) or $p_\lambda = -1$ (for $\lambda = 3, 4$). Under the symbol of the momentum summation, $\delta_{\mathbf{k}_1+\mathbf{k}_2+\mathbf{k}_3,\mathbf{0}}$ is introduced to impose the momentum conservation law on the spin waves. This conservation should be satisfied at every interaction vertex in any scattering processes. Non-zero coefficients of $\mathrm{C}^{(\lambda_1\lambda_2\lambda_3)}_{\mathbf{k}_1,\mathbf{k}_2,\mathbf{k}_3}$ are given by

$$\begin{aligned}
\mathrm{C}^{(331)}_{\mathbf{k}_1,\mathbf{k}_2,\mathbf{k}_3} &= \mathrm{C}^{(131)}_{\mathbf{k}_1,\mathbf{k}_2,\mathbf{k}_3} = (A_3 - A_1)\gamma_{\mathbf{k}_1},\\
\mathrm{C}^{(342)}_{\mathbf{k}_1,\mathbf{k}_2,\mathbf{k}_3} &= \mathrm{C}^{(142)}_{\mathbf{k}_1,\mathbf{k}_2,\mathbf{k}_3} = -A_1\gamma_{\mathbf{k}_1},\\
\mathrm{C}^{(431)}_{\mathbf{k}_1,\mathbf{k}_2,\mathbf{k}_3} &= \mathrm{C}^{(231)}_{\mathbf{k}_1,\mathbf{k}_2,\mathbf{k}_3} = (B_3 - B_1)\gamma_{\mathbf{k}_1},\\
\mathrm{C}^{(442)}_{\mathbf{k}_1,\mathbf{k}_2,\mathbf{k}_3} &= \mathrm{C}^{(242)}_{\mathbf{k}_1,\mathbf{k}_2,\mathbf{k}_3} = -B_1\gamma_{\mathbf{k}_1},\\
\mathrm{C}^{(341)}_{\mathbf{k}_1,\mathbf{k}_2,\mathbf{k}_3} &= \mathrm{C}^{(132)}_{\mathbf{k}_1,\mathbf{k}_2,\mathbf{k}_3} = C_3\gamma_{\mathbf{k}_1},\\
\mathrm{C}^{(332)}_{\mathbf{k}_1,\mathbf{k}_2,\mathbf{k}_3} &= \mathrm{C}^{(141)}_{\mathbf{k}_1,\mathbf{k}_2,\mathbf{k}_3} = D_3\gamma_{\mathbf{k}_1},\\
\mathrm{C}^{(432)}_{\mathbf{k}_1,\mathbf{k}_2,\mathbf{k}_3} &= \mathrm{C}^{(241)}_{\mathbf{k}_1,\mathbf{k}_2,\mathbf{k}_3} = E_3\gamma_{\mathbf{k}_1},\\
\mathrm{C}^{(441)}_{\mathbf{k}_1,\mathbf{k}_2,\mathbf{k}_3} &= \mathrm{C}^{(232)}_{\mathbf{k}_1,\mathbf{k}_2,\mathbf{k}_3} = F_3\gamma_{\mathbf{k}_1},
\end{aligned}$$

and the others are identically zero. Specifically for $n_0 \gg 1$, $\mathrm{C}^{(431)}_{\mathbf{k}_1,\mathbf{k}_2,\mathbf{k}_3} = \mathrm{C}^{(231)}_{\mathbf{k}_1,\mathbf{k}_2,\mathbf{k}_3} = \mathrm{C}^{(442)}_{\mathbf{k}_1,\mathbf{k}_2,\mathbf{k}_3} = \mathrm{C}^{(242)}_{\mathbf{k}_1,\mathbf{k}_2,\mathbf{k}_3} = \mathrm{C}^{(341)}_{\mathbf{k}_1,\mathbf{k}_2,\mathbf{k}_3} = \mathrm{C}^{(132)}_{\mathbf{k}_1,\mathbf{k}_2,\mathbf{k}_3} = \mathrm{C}^{(332)}_{\mathbf{k}_1,\mathbf{k}_2,\mathbf{k}_3} = \mathrm{C}^{(141)}_{\mathbf{k}_1,\mathbf{k}_2,\mathbf{k}_3} = 0$ because these terms have an odd number of $b_{2,\mathbf{k}}$.

Here we make a comment on the quartic term $\mathcal{H}_{\rm SW}^{(4)}$. In this Thesis, the quartic term does not enter into our theoretical calculations for the linear response functions because, as we will see in Sect. 4.2.4, it would not provide significant effects on the stability of the Higgs mode.

4.2.3 Bogoliubov Transformation for the Spin Waves

In the previous section, we have performed the HP expansion for the Hamiltonian (4.6) and looked at some properties of $\mathcal{H}_{\rm SW}^{(l)}$, individually. In the representation with the spin-wave operators $b_{m,\mathbf{k}}$, the quadratic part of the expanded Hamiltonian can have off-diagonal terms. In this section, we diagonalize the quadratic Hamiltonian by using the Bogoliubov transformation for the multi-component spin-wave operators as we did in Sect. 2.5.5. Compared with the method shown there, the following approach, which was also employed by Huber et al. in Ref. [12], is applicable even

to low-filling cases, in which two different flavors are not decoupled in the quadratic Hamiltonian.

To find the diagonalized basis, we define a new boson denoted by $\beta_{m,\mathbf{k}}$ through the following linear transformation:

$$\mathbf{b}_{\mathbf{k}} = \mathrm{W}_{\mathbf{k}}\boldsymbol{\beta}_{\mathbf{k}}, \quad \boldsymbol{\beta}_{\mathbf{k}} = \mathrm{W}_{\mathbf{k}}^{-1}\mathbf{b}_{\lambda,\mathbf{k}}, \tag{4.13}$$

where $\boldsymbol{\beta}_{\mathbf{k}} = (\beta_{1,\mathbf{k}}, \beta_{2,\mathbf{k}}, \beta_{3,\mathbf{k}}, \beta_{4,\mathbf{k}})^{\mathrm{T}}$, $\beta_{3,\mathbf{k}} \equiv \beta_{1,-\mathbf{k}}^{\dagger}$, and $\beta_{4,\mathbf{k}} \equiv \beta_{2,-\mathbf{k}}^{\dagger}$. These new bosons are supposed to satisfy the usual canonical relation for bosons

$$[\beta_{m,\mathbf{k}}, \beta_{n,\mathbf{k}'}^{\dagger}] = \delta_{m,n}\delta_{\mathbf{k},\mathbf{k}'}, \quad [\beta_{m,\mathbf{k}}, \beta_{n,\mathbf{k}'}] = [\beta_{m,\mathbf{k}}^{\dagger}, \beta_{n,\mathbf{k}'}^{\dagger}] = 0, \tag{4.14}$$

for $m, n = 1$ or 2. Due to this, the linear transformation $\mathrm{W}_{\mathbf{k}}$ fulfills

$$\mathrm{W}_{\mathbf{k}}\mathrm{g}\mathrm{W}_{\mathbf{k}}^{\dagger} = \mathrm{W}_{\mathbf{k}}^{\dagger}\mathrm{g}\mathrm{W}_{\mathbf{k}} = \mathrm{g}, \tag{4.15}$$

where $\mathrm{g} = \mathrm{diag}(1, 1, -1, -1)$ is the metric tensor in the Minkowski space $\mathbb{M}^{2\otimes 2}$. Without loss of generality, one can write the elements of $\mathrm{W}_{\mathbf{k}}$ in the form

$$\mathrm{W}_{\mathbf{k}} = \begin{pmatrix} u_{11}(\mathbf{k}) & u_{12}(\mathbf{k}) & v_{11}(\mathbf{k}) & v_{12}(\mathbf{k}) \\ u_{21}(\mathbf{k}) & u_{22}(\mathbf{k}) & v_{21}(\mathbf{k}) & v_{22}(\mathbf{k}) \\ v_{11}^{*}(-\mathbf{k}) & v_{12}^{*}(-\mathbf{k}) & u_{11}^{*}(-\mathbf{k}) & u_{12}^{*}(-\mathbf{k}) \\ v_{21}^{*}(-\mathbf{k}) & v_{22}^{*}(-\mathbf{k}) & u_{21}^{*}(-\mathbf{k}) & u_{22}^{*}(-\mathbf{k}) \end{pmatrix}. \tag{4.16}$$

The transformation parameters such as $u_{11}(\mathbf{k})$ are determined as follows: For an adequate set of parameters, the Hamiltonian should have a diagonalized form

$$\begin{aligned} \mathcal{H}_{\mathrm{SW}}^{(2)} &= \delta E_2 + \sum_{\lambda=1}^{4}\sum_{\nu=1}^{4}\sum_{\mathbf{k}\in\Lambda_0} \beta_{\lambda,\mathbf{k}}^{\dagger}(\mathrm{D}_{\mathbf{k}})_{\lambda\nu}\beta_{\nu,\mathbf{k}}, \\ \mathrm{D}_{\mathbf{k}} &= \mathrm{diag}[e_1(\mathbf{k}), e_2(\mathbf{k}), e_3(\mathbf{k}), e_4(\mathbf{k})]. \end{aligned} \tag{4.17}$$

The diagonal matrix $\mathrm{D}_{\mathbf{k}}$ is not known at the moment, and it is obtained from the similarity transformation with use of $\mathrm{W}_{\mathbf{k}}$ for the 4×4 matrix $\mathrm{g}\mathrm{H}_{\mathbf{k}}$, but not $\mathrm{H}_{\mathbf{k}}$ itself:

$$\mathrm{W}_{\mathbf{k}}^{-1}(\mathrm{g}\mathrm{H}_{\mathbf{k}})\mathrm{W}_{\mathbf{k}} = \mathrm{g}\mathrm{D}_{\mathbf{k}}. \tag{4.18}$$

This can be regarded as an eigenvalue equation for $\mathrm{g}\mathrm{H}_{\mathbf{k}}$. If it is solved, we have two dispersions, $\mathcal{E}_{1,\mathbf{k}} = e_1(\mathbf{k}) + e_3(\mathbf{k})$ for $\beta_{1,\mathbf{k}}$ and $\mathcal{E}_{2,\mathbf{k}} = e_2(\mathbf{k}) + e_4(\mathbf{k})$ for $\beta_{2,\mathbf{k}}$, as the gapped Higgs and gapless NG dispersions, respectively. The matrix $\mathrm{W}_{\mathbf{k}}$ can be constructed from right eigenvectors belonging to the different eigenvalues. Notice that the left eigenvectors can be computed as well, but generally they do not agree with the right ones because $\mathrm{g}\mathrm{H}_{\mathbf{k}}$ is a non-Hermitian matrix.

One can solve this eigenvalue problem analytically or numerically. In the large-filling limit $n_0 \gg 1$, since the branches labeled by 1 or 2 are completely decoupled, it can be solved analytically. In this case, the transformation matrix is reduced such that

$$\mathrm{W}_{\mathbf{k}} \to \begin{pmatrix} u_{1,\mathbf{k}} & 0 & v_{1,\mathbf{k}} & 0 \\ 0 & u_{2,\mathbf{k}} & 0 & v_{2,\mathbf{k}} \\ v^*_{1,-\mathbf{k}} & 0 & u^*_{1,-\mathbf{k}} & 0 \\ 0 & v^*_{2,-\mathbf{k}} & 0 & u^*_{2,-\mathbf{k}} \end{pmatrix}, \tag{4.19}$$

where the elements have been given by Eqs. (2.59) and (2.60). This matrix can reproduce the dispersion relations for the large-filling limit [see Eq. (2.62)]. At low fillings, Huber and his coworkers derived the analytical expression for the dispersion relations in the superfluid phase [12]. In this Thesis, we simply solve the eigenvalue problem using a numerical diagonalization approach in order to have both dispersions and transformation matrix. These will be needed to make calculations of the response functions in Sect. 4.3.

In the diagonalized frame of the quadratic part, the cubic term $\mathcal{H}^{(3)}_{\mathrm{SW}}$ becomes

$$\mathcal{H}^{(3)}_{\mathrm{SW}} = \frac{1}{\sqrt{N}} \prod_{i=1}^{3} \sum_{\lambda_i=1}^{4} \sum_{\mathbf{k}_i \in \Lambda_0} \mathrm{M}^{(\lambda_1\lambda_2\lambda_3)}_{p_{\lambda_1}\mathbf{k}_1, p_{\lambda_2}\mathbf{k}_2, p_{\lambda_3}\mathbf{k}_3} \delta_{\mathbf{k}_1+\mathbf{k}_2+\mathbf{k}_3,\mathbf{0}}\, \beta_{\lambda_1,\mathbf{k}_1} \beta_{\lambda_2,\mathbf{k}_2} \beta_{\lambda_3,\mathbf{k}_3}. \tag{4.20}$$

The new coefficient $\mathrm{M}^{(\lambda_1\lambda_2\lambda_3)}_{\mathbf{k}_1,\mathbf{k}_2,\mathbf{k}_3}$ is a linear combination of the old ones $\mathrm{C}^{(\lambda_1\lambda_2\lambda_3)}_{\mathbf{k}_1,\mathbf{k}_2,\mathbf{k}_3}$. It has been introduced through the following relation

$$\mathrm{M}^{(\lambda_1\lambda_2\lambda_3)}_{p_{\lambda_1}\mathbf{k}_1, p_{\lambda_2}\mathbf{k}_2, p_{\lambda_3}\mathbf{k}_3} = \sum_{\nu_1,\nu_2,\nu_3=1}^{4} \mathrm{C}^{(\nu_1\nu_2\nu_3)}_{p_{\nu_1}\mathbf{k}_1, p_{\nu_2}\mathbf{k}_2, p_{\nu_3}\mathbf{k}_3} (\mathrm{W}_{\mathbf{k}_1})_{\nu_1}^{\ \lambda_1} (\mathrm{W}_{\mathbf{k}_2})_{\nu_2}^{\ \lambda_2} (\mathrm{W}_{\mathbf{k}_3})_{\nu_3}^{\ \lambda_3}, \tag{4.21}$$

which looks like a basis change of tensors having three indices. The delta $\delta_{\mathbf{k}_1+\mathbf{k}_2+\mathbf{k}_3,\mathbf{0}}$ describes the momentum-conservation law among three new operators in the transformed basis.

The coefficient $\mathrm{M}^{(\lambda_1\lambda_2\lambda_3)}_{\mathbf{k}_1,\mathbf{k}_2,\mathbf{k}_3}$ characterizes the interactions among the three collective modes expressed in the diagonalized basis, i.e., the Bogoliubov quasi-particles. For the large-filling limit $n_0 \gg 1$, scattering processes with an odd number of the NG modes are prohibited because the effective model in this limit (2.44) has the explicit particle-hole symmetry. On the other hand, the effective model at lower filling rates (2.45) has no longer such a symmetry, thereby permitting not only the even-NG processes, but also the odd-NG ones. As we will see in Sect. 4.3.3, new types of contribution show up in calculations of the response functions at low fillings due to such a difference at the microscopic level.

4.2.4 Normal-Ordered Hamiltonian

So far we have formulated the Bogoliubov transformation for the spin-wave Hamiltonian $\mathcal{H}_{\rm SW}$. Obviously, the transformed Hamiltonian, which is obtained after plugging the transformation (4.13) into Eq. (4.7), is not written in the normal-ordered form with respect to $\beta_{m,\mathbf{k}}$. Before proceeding to the field-theoretical calculation for the spin-wave model presented in Sect. 4.3, we here need to deal with the normal-ordered spin-wave Hamiltonian.

Let us begin with the quadratic part of the total spin-wave Hamiltonian, i.e., $\mathcal{H}^{(2)}_{\rm SW}$. In the following discussion, two colons $:\mathcal{A}:$ denote the normal-ordering operation for an arbitrary field operator $\mathcal{A}$, where all creation operators of the quasi-particle are put in the left-hand side of products of the annihilation operators. This is a subtraction of the vacuum-expectation-value contribution for arbitrary field operators. In the quadratic Hamiltonian, bilinear operators, which are not in the normal-ordered form, can yield a constant shift after taking permutation between two canonical pairs, i.e., $\beta_{m,\mathbf{k}}$ and $\beta^{\dagger}_{m,\mathbf{k}}$. A direct calculation leads to the following form

$$\mathcal{H}^{(2)}_{\rm SW} = \delta E_2 + \delta\tilde{E}_2 + :\tilde{\mathcal{H}}^{(2)}_{\rm SW}:,$$

where $\delta\tilde{E}_2$ is the constant shift arising after permutation of the operators.

Writing the cubic term, i.e., $\mathcal{H}^{(3)}_{\rm SW}$, in the normal-ordered form, we have

$$\mathcal{H}^{(3)}_{\rm SW} =: \mathcal{H}^{(3)}_{\rm SW} : + \delta\mathcal{H}^{(1)}_{\rm SW}.$$

As the result of permutation, a linear term $\delta\mathcal{H}^{(1)}_{\rm SW}$ arises from the cubic term. This modifies the *bare* linear term in the spin wave Hamiltonian. Similarly, the quartic Hamiltonian, i.e., $\mathcal{H}^{(4)}_{\rm SW}$, can take the following form:

$$\mathcal{H}^{(4)}_{\rm SW} = \delta E_4 + :\delta\mathcal{H}^{(2)}_{\rm SW}: + :\mathcal{H}^{(4)}_{\rm SW}:,$$

where δE_4 and $:\delta\mathcal{H}^{(2)}_{\rm SW}:$ can be viewed as the constant and quadratic corrections to the corresponding *bare* terms.

The total constant shift $\delta E_2 + \delta\tilde{E}_2 + \delta E_4$ can be interpreted as a fluctuation correction to the mean-field ground state energy $\mathcal{H}^{(0)}_{\rm SW}$ [12]. The first two terms represent $1/S$ corrections to the ground-state energy and the last term is a higher order correction of order $1/S^2$. Minimizing the modified ground-state energy with respect to θ and χ leads to a renormalization of the variational parameters of the mean-field configuration: $\theta_{\rm mf} \to \theta_{\rm ren} = \theta_{\rm mf} + \delta\theta_{\rm cor}$ and $\chi_{\rm mf} \to \chi_{\rm ren} = \chi_{\rm mf} + \delta\chi_{\rm cor}$. This corresponds to a reduction of the order-parameter amplitude induced by quantum and thermal fluctuations. At the renormalized configuration, the linear term including the shift from the cubic Hamiltonian $\mathcal{H}^{(3)}_{\rm SW}$ can vanish: $\mathcal{H}^{(1)}_{\rm SW} + \delta\mathcal{H}^{(1)}_{\rm SW} = 0$. Moreover, the renormalized parameters and additional quadratic term $:\delta\mathcal{H}^{(2)}_{\rm SW}:$ modify the mean-field band dispersions $\mathcal{E}_{1,\mathbf{k}}$ and $\mathcal{E}_{2,\mathbf{k}}$, which are calculated within the Gutzwiller-type variational ansatz.

Naively, it is expected that inclusion of the renormalization effect due to the fluctuations should make the low-energy properties more quantitative. The fluctuation correction, which is perturbatively incorporated around the mean-field state, leads to, however, a finite gap opening of the NG branch. In general, the NG mode must be gapless in the symmetry-broken phase in the thermodynamic limit. It seems that the appearance of the finite gap in our perturbative scheme would be an artifact of this approach. Moreover, whether the finite gap exists or not strongly affects the decay processes of the Higgs mode because the possible scattering channels are restricted by the on-shell energy-momentum conservation laws between the collective modes [14]. Thus, in order to describe the stability of the Higgs mode corresponding to experiments, we need to eliminate the finite gap from the NG mode branch.

The similar theoretical problem also happens in the well-known Hartree–Fock–Bogoliubov (HFB) approximation for single component dilute Bose gases [15–18]. In this approximation, it is observed that an off-diagonal or anomalous average of non-condensate bosons remains nonzero and leads to a gap opening in the low-energy NG or Bogoliubov spectrum. Such an artificial energy gap is often eliminated by the so called Popov–Shohno prescription [15, 18, 19], in which the anomalous average is detuned by hands such that the artificial gap vanishes. Nevertheless, the generalization of this prescription to our case is not straightforward because our spin-wave bosons possess two flavors corresponding to the Higgs and NG modes. Therefore, in this Thesis, we do neglect the modification of the mean-field variational parameters as a simpler prescription. Our prescription done in this Thesis is similar in spirit to the standard Bogoliubov approximation for dilute Bose gases [20]. We expect that this treatment becomes better as the spatial dimension of the system increases and the temperature decreases.

In addition to such a prescription, we also neglect the normal-ordered quartic term $:\mathcal{H}_{\rm SW}^{(4)}:$ throughout our analysis. Within our lowest order $O(S^0)$, the term only generates a shift of the peak position of the Higgs mode, but no contribution to the peak width itself. Moreover, the shift is expected to be rather small at sufficiently low temperatures. Thus, it makes no important difference whether the quartic term exists or not, as far as the problem of the stability of the Higgs mode is concerned.

We would like to close this section with the following normal-ordered Hamiltonian up to the third-order term:

$$\mathcal{H}_{\rm SW} = \text{const.} + :\tilde{\mathcal{H}}_{\rm SW}^{(2)}: + :\mathcal{H}_{\rm SW}^{(3)}: . \tag{4.22}$$

This model will be a starting point of our field-theoretical calculations for analyzing the linear-response functions.

4.3 Linear Response Analysis

In this section, we study the linear response functions, Eqs. (4.1) and (4.4), for the normal-ordered spin-wave Hamiltonian (4.22). We develop a diagrammatic perturbation theory for calculating imaginary-time Green's functions at nonzero temper-

atures. This Thesis has no part for reviewing the finite-temperature quantum field theory for a system of Bose particles. For instructive explanations associated with this theoretical technique, see textbooks, e.g., Refs. [21–23].

4.3.1 Response Functions to the External Modulations

In the spin-wave theory, arbitrary operators in the original model are expressed by means of the spin-wave operators in the diagonalized basis, i.e., $\beta_{m,\mathbf{k}}$. Let us derive the spin-wave representation of the K-to-K response function (4.1). Using the HP expansion (2.57) and performing the Bogoliubov transformation (4.13), the kinetic energy K becomes

$$K = NA_0 + \sqrt{N}\Upsilon_1(\beta^\dagger_{1,\mathbf{0}} + \beta_{1,\mathbf{0}}) + \cdots . \tag{4.23}$$

The coefficient Υ_1 is a functional of the coefficient of the Bogoliubov transformation at $\mathbf{k} = \mathbf{0}$:

$$\Upsilon_1 = A_1[u_{11}(\mathbf{0}) + v_{11}(\mathbf{0})] + B_1[u_{21}(\mathbf{0}) + v_{21}(\mathbf{0})]. \tag{4.24}$$

It should be noted that the rest of the terms in Eq. (4.23) includes a linear term, which is proportional to $\beta_{2,\mathbf{0}} + \beta^\dagger_{2,\mathbf{0}}$. Here, $\beta_{2,\mathbf{0}}$ corresponds to the zero energy mode of the system. We can easily check that the coefficient of $\beta_{2,\mathbf{0}} + \beta^\dagger_{2,\mathbf{0}}$ should be zero because of the property of the eigenvalue equation for $[u_{12}(\mathbf{0}), v_{12}(\mathbf{0}), u_{22}(\mathbf{0}), v_{22}(\mathbf{0})]$ in Eq. (4.18). As shown below, the zero-mode contribution to the linear response functions is therefore eliminated from our analysis.

Substituting Eq. (4.23) into the definition of $D^{\mathrm{R}}_{KK}(t-t')$ and keeping leading-order terms, we obtain the approximate response function

$$\begin{aligned} D^{\mathrm{R}}_{KK}(t-t') = N|\Upsilon_1|^2 \big\{ & G^{\mathrm{R}}_{13,\mathbf{0}}(t-t') + G^{\mathrm{R}}_{31,\mathbf{0}}(t-t') \\ & + G^{\mathrm{R}}_{11,\mathbf{0}}(t-t') + G^{\mathrm{R}}_{33,\mathbf{0}}(t-t') \big\} . \end{aligned} \tag{4.25}$$

To express this function, we have introduced four types of retarded Green's function for the zero-momentum Higgs-mode operators, i.e., $\beta_{1,\mathbf{0}}$ and $\beta^\dagger_{1,\mathbf{0}}$:

$$\begin{aligned} G^{\mathrm{R}}_{13,\mathbf{0}}(t-t') &= -i\Theta(t-t')\langle[\beta_{1,\mathbf{0}}(t), \beta^\dagger_{1,\mathbf{0}}(t')]\rangle_{\mathrm{eq}}, \\ G^{\mathrm{R}}_{11,\mathbf{0}}(t-t') &= -i\Theta(t-t')\langle[\beta_{1,\mathbf{0}}(t), \beta_{1,\mathbf{0}}(t')]\rangle_{\mathrm{eq}}, \\ G^{\mathrm{R}}_{31,\mathbf{0}}(t-t') &= -i\Theta(t-t')\langle[\beta^\dagger_{1,\mathbf{0}}(t), \beta_{1,\mathbf{0}}(t')]\rangle_{\mathrm{eq}}, \\ G^{\mathrm{R}}_{33,\mathbf{0}}(t-t') &= -i\Theta(t-t')\langle[\beta^\dagger_{1,\mathbf{0}}(t), \beta^\dagger_{1,\mathbf{0}}(t')]\rangle_{\mathrm{eq}}. \end{aligned} \tag{4.26}$$

Higher-order terms eliminated from the expansion correspond to multi-spin-wave propagators, which are negligible if the fluctuations are sufficiently small. Thus, up to

the leading order, evaluating the response function $D^{\mathrm{R}}_{KK}(t-t')$ is reduced to calculating the retarded Green's functions for the Higgs mode. The Fourier transformation of Eq. (4.25) with respect to the time argument provides the dynamical susceptibility associated with the kinetic-energy modulation as seen in Eq. (4.3). Now the Higgs mode is captured as a characteristic pole in the retarded single-particle propagators for the collective quasi-particle excitation.

Similarly, one can expand the O-to-O response function (4.4) in the Bogoliubov operators. Keeping terms up to the linear order, the onsite interaction energy O is approximated to

$$O = N\tilde{A}'_0 + \sqrt{N}\Upsilon_2(\beta^\dagger_{1,\mathbf{0}} + \beta_{1,\mathbf{0}}) + \cdots . \tag{4.27}$$

The coefficient Υ_2 is defined by

$$\Upsilon_2 = \tilde{A}'_1[u_{11}(\mathbf{0}) + v_{11}(\mathbf{0})], \tag{4.28}$$

and the constants $\tilde{A}'_0$ and $\tilde{A}'_1$ are given by

$$\tilde{A}'_0 = \frac{1}{2}s_1^2, \quad \tilde{A}'_1 = -\frac{1}{2}s_1c_1. \tag{4.29}$$

The expansion (4.27) has no zero-mode term of $\beta_{2,\mathbf{0}} + \beta^\dagger_{2,\mathbf{0}}$ for the same reason as Eq. (4.23). Plugging Eq. (4.27) into $D^{\mathrm{R}}_{OO}(t-t')$ and neglecting higher-order corrections, we have

$$\begin{aligned} D^{\mathrm{R}}_{OO}(t-t') = N|\Upsilon_2|^2 \big\{ & G^{\mathrm{R}}_{13,\mathbf{0}}(t-t') + G^{\mathrm{R}}_{31,\mathbf{0}}(t-t') \\ & + G^{\mathrm{R}}_{11,\mathbf{0}}(t-t') + G^{\mathrm{R}}_{33,\mathbf{0}}(t-t') \big\} . \end{aligned} \tag{4.30}$$

The dynamical susceptibility $\chi_{OO}(\omega)$ is given by the real-time Fourier transformation of this equation [see also Eq. (4.5)].

Within the leading order, the form of the O-to-O response function is the same as that of the K-to-K response function except for the coefficients $|\Upsilon_1|^2$ and $|\Upsilon_2|^2$. In Fig. 4.1, we show the chemical potential dependence of the coefficients at $\bar{n} = n_0 = 1$ and $u = 1$. The point indicated by a solid arrow in Fig. 4.1 is at the commensurate filling rate n_0, and the corresponding chemical potential is expressed by μ_{n_0} whose explicit form is presented by Eq. (2.53). As depicted in Fig. 4.1, it is found that the coefficients completely coincide with each other for any μ. Hence, there is no difference between two response functions, at least, within our approximation. We note that for other values of n_0 and u two curves also coincide with each other.

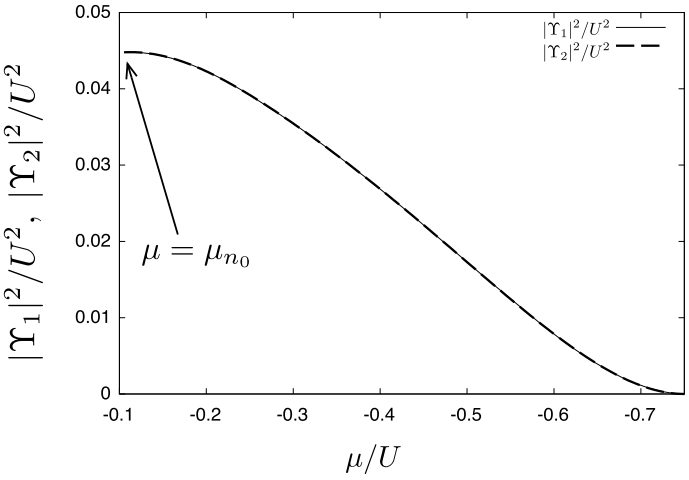

Fig. 4.1 μ dependence of the coefficients $|\Upsilon_1|^2$ and $|\Upsilon_2|^2$, respectively. In this figure, the parameters are $n_0 = 1$ and $u = 1$ ($zJ/U = 0.25$). The solid (dashed) line expresses $|\Upsilon_1|^2/U^2$ ($|\Upsilon_2|^2/U^2$) corresponding to the hopping (onsite-interaction) modulation. The solid arrow indicates the unit filling case $\bar{n} = n_0 = 1$. The mean filling rate $\bar{n}$ decreases as μ decreases. Below $\mu \approx -0.75$, $\bar{n}$ becomes zero. (This figure is reproduced from Ref. [25]. Copyright © 2018 American Physical Society. All rights reserved)

4.3.2 *Imaginary-Time Green's Functions*

We analyze the retarded single-particle Green's functions in linear response functions (4.25) and (4.30) by using techniques of the finite-temperature quantum-field theory. Let us consider three imaginary-time single-particle Green's functions, where the time-dependent field operators are ordered in time along the imaginary-time axis [21–23]:

$$
\begin{aligned}
G_{1,\mathbf{k}}(\tau - \tau') &= -\langle T_\tau \beta_{1,\mathbf{k}}(\tau)\beta^\dagger_{1,\mathbf{k}}(\tau')\rangle_{\mathrm{eq}} + \langle \beta_{1,\mathbf{0}}(0)\rangle_{\mathrm{eq}}\langle \beta^\dagger_{1,\mathbf{0}}(0)\rangle_{\mathrm{eq}}, \\
F_{1,\mathbf{k}}(\tau - \tau') &= -\langle T_\tau \beta_{1,\mathbf{k}}(\tau)\beta_{1,-\mathbf{k}}(\tau')\rangle_{\mathrm{eq}} + \langle \beta_{1,\mathbf{0}}(0)\rangle^2_{\mathrm{eq}}, \\
F^\dagger_{1,\mathbf{k}}(\tau - \tau') &= -\langle T_\tau \beta^\dagger_{1,-\mathbf{k}}(\tau)\beta^\dagger_{1,\mathbf{k}}(\tau')\rangle_{\mathrm{eq}} + \langle \beta^\dagger_{1,\mathbf{0}}(0)\rangle^2_{\mathrm{eq}}.
\end{aligned}
$$

Here, T_τ indicates the imaginary-time ordering for field operators, and $\tau, \tau' \in [0, \beta]$. The last two functions are referred to as anomalous Green's functions in some contexts [21, 22] because they can vanish if the quantum state of the system has a conserved quasi-particle occupation.

We suppose that the imaginary-time Green's functions are periodic along the time direction. Intuitively, the domain of definition looks like a closed strip with the length of the inverse temperature β [21–23]. One can decompose them into the Fourier series in the Matsubara frequency space. The coefficients of such a decomposition are given by

$$\mathcal{G}_{1,\mathbf{k}}(i\omega_n) = \int_0^\beta d\tau G_{1,\mathbf{k}}(\tau)e^{i\omega_n\tau},$$
$$\mathcal{F}_{1,\mathbf{k}}(i\omega_n) = \int_0^\beta d\tau F_{1,\mathbf{k}}(\tau)e^{i\omega_n\tau},$$
$$\mathcal{F}^\dagger_{1,\mathbf{k}}(i\omega_n) = \int_0^\beta d\tau F^\dagger_{1,\mathbf{k}}(\tau)e^{i\omega_n\tau},$$

where $\omega_n = 2\pi n/\beta$ ($n \in \mathbb{Z}$) is the Matsubara frequency for bosons [21–23]. It should be noted that a relation $\mathcal{F}^\dagger_{1,\mathbf{k}}(i\omega_n) = \mathcal{F}_{1,\mathbf{k}}(-i\omega_n)$ holds for any n, at least, within our leading order $O(S^0)$. In fact, this is verified by a straightforward calculation based on the perturbative expansion. According to more general consideration [22], this relation is expected to be true at any order of the perturbation series.

For a fixed ω_n and at $\mathbf{k} = \mathbf{0}$, the imaginary-time Green functions $\mathcal{G}_{1,\mathbf{k}}(i\omega_n)$ and $\mathcal{F}_{1,\mathbf{k}}(i\omega_n)$ obey Dyson's equation as follows [21, 22]:

$$\begin{aligned}\mathcal{G}_{1,\mathbf{0}}(i\omega_n) = \mathcal{G}^{(0)}_{1,\mathbf{0}}(i\omega_n) + \mathcal{G}^{(0)}_{1,\mathbf{0}}(i\omega_n)\Sigma_{11}(i\omega_n)\mathcal{G}_{1,\mathbf{0}}(i\omega_n) \\ + \mathcal{G}^{(0)}_{1,\mathbf{0}}(i\omega_n)\Sigma_{02}(i\omega_n)\mathcal{F}_{1,\mathbf{0}}(-i\omega_n),\\ \mathcal{F}_{1,\mathbf{0}}(i\omega_n) = \mathcal{G}^{(0)}_{1,\mathbf{0}}(i\omega_n)\Sigma_{11}(i\omega_n)\mathcal{F}_{1,\mathbf{0}}(i\omega_n) + \mathcal{G}^{(0)}_{1,\mathbf{0}}(i\omega_n)\Sigma_{02}(i\omega_n)\mathcal{G}_{1,\mathbf{0}}(-i\omega_n),\end{aligned}$$

where $\Sigma_{11}(i\omega_n)$ and $\Sigma_{02}(i\omega_n)$ are the self-energy functions for the normal and anomalous Green's functions. Here,

$$\mathcal{G}^{(0)}_{1,\mathbf{0}}(i\omega_n) = \frac{1}{i\omega_n - \Delta} \tag{4.31}$$

is the non-interacting propagator of the Higgs mode with $\mathbf{k} = \mathbf{0}$, where the characteristic pole is centered at the energy gap position Δ, i.e., the mean-field Higgs gap. Since the Dyson equation is closed up to the single-particle Green's functions, we can solve it formally with respect to $\mathcal{G}_{1,\mathbf{0}}(i\omega_n)$ and $\mathcal{F}_{1,\mathbf{0}}(i\omega_n)$ [21, 22]. The solutions are simply given by

$$\mathcal{G}_{1,\mathbf{0}}(i\omega_n) = -\frac{1}{D}\left\{\left[\mathcal{G}^{(0)}_{1,\mathbf{0}}(-i\omega_n)\right]^{-1} - \Sigma_{11}(-i\omega_n)\right\}, \tag{4.32}$$
$$\mathcal{F}_{1,\mathbf{0}}(i\omega_n) = -\frac{1}{D}\Sigma_{02}(i\omega_n). \tag{4.33}$$

The denominator D defined by

$$D = [\Sigma_{02}(i\omega_n)]^2 - [i\omega_n - \Delta - \Sigma_{11}(i\omega_n)]\,[-i\omega_n - \Delta - \Sigma_{11}(-i\omega_n)], \tag{4.34}$$

characterizes the poles of these Green's functions, whose properties are modified due to the self-energy effects. The self-energy corrections can arise when non-linear terms in the Hamiltonian perturb free propagation of the quasi-particle excitations.

Calculating such corrections by means of the normal-ordered spin-wave Hamiltonian will be a main subject in the next section.

Let us briefly see the relationship between our imaginary-time functions and the real-time response functions. In the linear response theory, retarded correlation functions associated with physical quantities can be obtained from an analytical continuation procedure for corresponding imaginary-time Green's functions [23]. The latter ones are given as a set of discrete data points distributed along an imaginary axis on a complex plane $\tilde{z}$, and they are typically computed by some techniques, e.g., field theoretical perturbation theories or quantum Monte-Carlo methods. To get the retarded functions, the data for all positive frequencies $n > 0$ are mapped onto a horizontal line that lies along nearby the real axis of the complex plane; it is a cutting line given by $\tilde{z} = \omega + i\epsilon$ where $\epsilon > 0$ is infinitesimally small [23]. We note that the points for negative frequencies $n < 0$ correspond to the so called advanced correlation functions at $\tilde{z} = \omega - i\epsilon$.

As an advantage, the perturbative approach that we use allows us to find concrete analytical forms of the imaginary-time Green's functions and self-energy functions. If we know the self-energy functions as a function of ω_n, the analytical continuation can be performed by just making a replacement as $i\omega_n \to \omega + i\epsilon$. Then, we can have the Fourier transformation of Eq. (4.26) in such a way that

$$\begin{aligned} G^{\mathrm{R}}_{13,\mathbf{0}}(\omega) &= \mathcal{G}_{1,\mathbf{0}}(i\omega_n)\big|_{i\omega_n\to\omega+i\epsilon}\,, \\ G^{\mathrm{R}}_{11,\mathbf{0}}(\omega) &= \mathcal{F}_{1,\mathbf{0}}(i\omega_n)\big|_{i\omega_n\to\omega+i\epsilon}\,, \\ G^{\mathrm{R}}_{31,\mathbf{0}}(\omega) &= \mathcal{G}_{1,\mathbf{0}}(-i\omega_n)\big|_{i\omega_n\to\omega+i\epsilon}\,, \\ G^{\mathrm{R}}_{33,\mathbf{0}}(\omega) &= \mathcal{F}_{1,\mathbf{0}}(-i\omega_n)\big|_{i\omega_n\to\omega+i\epsilon}\,. \end{aligned} \tag{4.35}$$

For the last equality, we used $\mathcal{F}^{\dagger}_{1,\mathbf{0}}(i\omega_n) = \mathcal{F}_{1,\mathbf{0}}(-i\omega_n)$. Using these results, the dynamical susceptibilities, $\chi_{KK}(\omega)$ and $\chi_{OO}(\omega)$, read

$$\chi_{KK}(\omega) = N|\Upsilon_1|^2\left\{G^{\mathrm{R}}_{13,\mathbf{0}}(\omega) + G^{\mathrm{R}}_{11,\mathbf{0}}(\omega) + G^{\mathrm{R}}_{31,\mathbf{0}}(\omega) + G^{\mathrm{R}}_{33,\mathbf{0}}(\omega)\right\}, \tag{4.36}$$

$$\chi_{OO}(\omega) = N|\Upsilon_2|^2\left\{G^{\mathrm{R}}_{13,\mathbf{0}}(\omega) + G^{\mathrm{R}}_{11,\mathbf{0}}(\omega) + G^{\mathrm{R}}_{31,\mathbf{0}}(\omega) + G^{\mathrm{R}}_{33,\mathbf{0}}(\omega)\right\}. \tag{4.37}$$

The final expressions are important for us because those characterize the spectral property of the Higgs mode resonance when the mode is kicked out by the external modulations. The numerical evaluation of them will be presented in Sect. 4.4.

4.3.3 One-Loop Self-energy Functions

We calculate the self-energy functions by using Feynman's perturbative technique with a diagrammatic expression of physical processes scattered by interactions. We focus on the lowest order contributions that are obtained from the second order perturbation of $:\mathcal{H}^{(3)}_{\mathrm{SW}}:$. The expansion is stopped up to 1-loop order, i.e., $O(S^0)$.

First, let us calculate the self-energy function $\Sigma_{11}(i\omega_n)$. The 1-loop contributions to this function are shown in Fig. 4.2. This 1-loop result can be divided into four different parts

$$\Sigma_{11}(i\omega_n) = \Sigma_{11}^{(a)}(i\omega_n) + \Sigma_{11}^{(b)}(i\omega_n) + \Sigma_{11}^{(c)}(i\omega_n) + \Sigma_{11}^{(d)}(i\omega_n). \tag{4.38}$$

These are given by

$$\begin{aligned}
\Sigma_{11}^{(a)}(i\omega_n) = &-\frac{1}{2N}\sum_{\mathbf{k}_1\in\Lambda_0} \mathrm{M}^{[333]}_{\mathbf{0},\mathbf{k}_1,-\mathbf{k}_1}\mathrm{M}^{[111]}_{\mathbf{k}_1,-\mathbf{k}_1,\mathbf{0}}\frac{1+2n_{\mathrm{B}}[\mathcal{E}_{1,\mathbf{k}_1}]}{i\omega_n+2\mathcal{E}_{1,\mathbf{k}_1}}\\
&-\frac{1}{2N}\sum_{\mathbf{k}_1\in\Lambda_0} \mathrm{M}^{[344]}_{\mathbf{0},\mathbf{k}_1,-\mathbf{k}_1}\mathrm{M}^{[221]}_{\mathbf{k}_1,-\mathbf{k}_1,\mathbf{0}}\frac{1+2n_{\mathrm{B}}[\mathcal{E}_{2,\mathbf{k}_1}]}{i\omega_n+2\mathcal{E}_{2,\mathbf{k}_1}}\\
&-\frac{1}{N}\sum_{\mathbf{k}_1\in\Lambda_0} \mathrm{M}^{[334]}_{\mathbf{0},\mathbf{k}_1,-\mathbf{k}_1}\mathrm{M}^{[211]}_{-\mathbf{k}_1,\mathbf{k}_1,\mathbf{0}}\frac{1+n_{\mathrm{B}}[\mathcal{E}_{1,\mathbf{k}_1}]+n_{\mathrm{B}}[\mathcal{E}_{2,\mathbf{k}_1}]}{i\omega_n+\mathcal{E}_{1,\mathbf{k}_1}+\mathcal{E}_{2,\mathbf{k}_1}},
\end{aligned} \tag{4.39}$$

$$\begin{aligned}
\Sigma_{11}^{(b)}(i\omega_n) = &\frac{1}{2N}\sum_{\mathbf{k}_1\in\Lambda_0} \mathrm{M}^{[311]}_{\mathbf{0},\mathbf{k}_1,-\mathbf{k}_1}\mathrm{M}^{[331]}_{\mathbf{k}_1,-\mathbf{k}_1,\mathbf{0}}\frac{1+2n_{\mathrm{B}}[\mathcal{E}_{1,\mathbf{k}_1}]}{i\omega_n-2\mathcal{E}_{1,\mathbf{k}_1}}\\
&+\frac{1}{2N}\sum_{\mathbf{k}_1\in\Lambda_0} \mathrm{M}^{[322]}_{\mathbf{0},\mathbf{k}_1,-\mathbf{k}_1}\mathrm{M}^{[441]}_{\mathbf{k}_1,-\mathbf{k}_1,\mathbf{0}}\frac{1+2n_{\mathrm{B}}[\mathcal{E}_{2,\mathbf{k}_1}]}{i\omega_n-2\mathcal{E}_{2,\mathbf{k}_1}}\\
&+\frac{1}{N}\sum_{\mathbf{k}_1\in\Lambda_0} \mathrm{M}^{[312]}_{\mathbf{0},\mathbf{k}_1,-\mathbf{k}_1}\mathrm{M}^{[341]}_{\mathbf{k}_1,-\mathbf{k}_1,\mathbf{0}}\frac{1+n_{\mathrm{B}}[\mathcal{E}_{1,\mathbf{k}_1}]+n_{\mathrm{B}}[\mathcal{E}_{2,\mathbf{k}_1}]}{i\omega_n-\mathcal{E}_{1,\mathbf{k}_1}-\mathcal{E}_{2,\mathbf{k}_1}},
\end{aligned} \tag{4.40}$$

$$\begin{aligned}
\Sigma_{11}^{(c)}(i\omega_n) = &-\frac{1}{N}\sum_{\mathbf{k}_1\in\Lambda_0} \mathrm{M}^{[332]}_{\mathbf{0},\mathbf{k}_1,\mathbf{k}_1}\mathrm{M}^{[411]}_{\mathbf{k}_1,\mathbf{k}_1,\mathbf{0}}\frac{n_{\mathrm{B}}[\mathcal{E}_{2,\mathbf{k}_1}]-n_{\mathrm{B}}[\mathcal{E}_{1,\mathbf{k}_1}]}{i\omega_n+\mathcal{E}_{1,\mathbf{k}_1}-\mathcal{E}_{2,\mathbf{k}_1}}\\
&-\frac{1}{N}\sum_{\mathbf{k}_1\in\Lambda_0} \mathrm{M}^{[312]}_{\mathbf{0},\mathbf{k}_1,\mathbf{k}_1}\mathrm{M}^{[341]}_{\mathbf{k}_1,\mathbf{k}_1,\mathbf{0}}\frac{n_{\mathrm{B}}[\mathcal{E}_{1,\mathbf{k}_1}]-n_{\mathrm{B}}[\mathcal{E}_{2,\mathbf{k}_1}]}{i\omega_n+\mathcal{E}_{2,\mathbf{k}_1}-\mathcal{E}_{1,\mathbf{k}_1}},
\end{aligned} \tag{4.41}$$

$$\begin{aligned}
\Sigma_{11}^{(d)}(i\omega_n) = &-\frac{1}{N}\sum_{\mathbf{k}_1\in\Lambda_0} \mathrm{M}^{[332]}_{\mathbf{0},\mathbf{0},\mathbf{0}}\mathrm{M}^{[411]}_{\mathbf{k}_1,\mathbf{0},\mathbf{k}_1}\frac{1}{\Delta}n_{\mathrm{B}}[\mathcal{E}_{1,\mathbf{k}_1}]\\
&-\frac{1}{N}\sum_{\mathbf{k}_1\in\Lambda_0} \mathrm{M}^{[341]}_{\mathbf{0},\mathbf{0},\mathbf{0}}\mathrm{M}^{[321]}_{\mathbf{0},\mathbf{k}_1,\mathbf{k}_1}\frac{1}{\Delta}n_{\mathrm{B}}[\mathcal{E}_{1,\mathbf{k}_1}]\\
&-\frac{1}{N}\sum_{\mathbf{k}_1\in\Lambda_0} \mathrm{M}^{[331]}_{\mathbf{0},\mathbf{0},\mathbf{0}}\mathrm{M}^{[311]}_{\mathbf{k}_1,\mathbf{0},\mathbf{k}_1}\frac{1}{\Delta}n_{\mathrm{B}}[\mathcal{E}_{2,\mathbf{k}_1}]\\
&-\frac{1}{N}\sum_{\mathbf{k}_1\in\Lambda_0} \mathrm{M}^{[311]}_{\mathbf{0},\mathbf{0},\mathbf{0}}\mathrm{M}^{[442]}_{\mathbf{k}_1,\mathbf{0},\mathbf{k}_1}\frac{1}{\Delta}n_{\mathrm{B}}[\mathcal{E}_{2,\mathbf{k}_1}].
\end{aligned} \tag{4.42}$$

Here, $n_{\mathrm{B}}(x) = (e^{\beta x}-1)^{-1}$ is the equilibrium Bose distribution function at temperature T. To get a simple expression, we introduced a symmetrized vertex coefficient

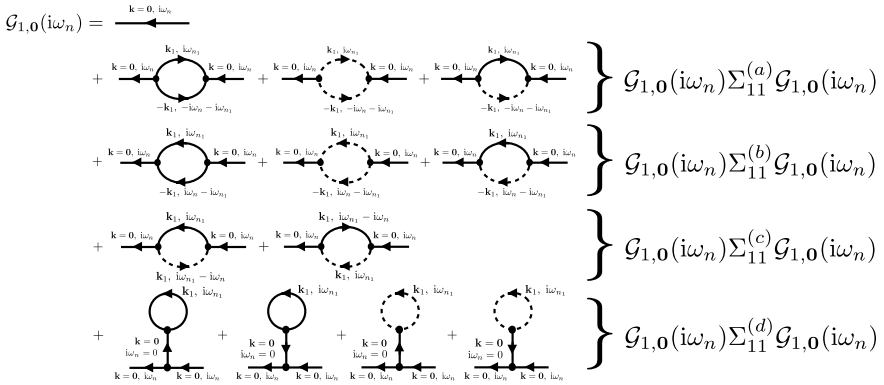

Fig. 4.2 Leading 1-loop order contributions to the normal Green's function $\mathcal{G}_{1,\mathbf{0}}(i\omega_n)$ and corresponding self-energy functions. The momenta and frequencies with an integer suffix imply the summation over possible internal states. The solid line denotes the non-interacting Higgs-mode propagator while the dashed one represents a free propagation of the NG mode. The arrow pointing to the left direction in the first column represents the zeroth-order Green's function of the Higgs mode. The diagrams in each column form an individual group labeled by $\Sigma_{11}^{(a)}(i\omega_n)$, $\Sigma_{11}^{(b)}(i\omega_n)$, $\Sigma_{11}^{(c)}(i\omega_n)$, or $\Sigma_{11}^{(d)}(i\omega_n)$. (This figure is reproduced from Ref. [25]. Copyright © 2018 American Physical Society. All rights reserved)

$$\mathrm{M}^{[l_1l_2l_3]}_{\mathbf{k}_1,\mathbf{k}_2,\mathbf{k}_3} = \mathrm{M}^{(l_1l_2l_3)}_{\mathbf{k}_1,\mathbf{k}_2,\mathbf{k}_3} + \mathrm{M}^{(l_1l_3l_2)}_{\mathbf{k}_1,\mathbf{k}_3,\mathbf{k}_2} + \mathrm{M}^{(l_2l_1l_3)}_{\mathbf{k}_2,\mathbf{k}_1,\mathbf{k}_3} + \mathrm{M}^{(l_2l_3l_1)}_{\mathbf{k}_2,\mathbf{k}_3,\mathbf{k}_1} + \mathrm{M}^{(l_3l_1l_2)}_{\mathbf{k}_3,\mathbf{k}_1,\mathbf{k}_2} + \mathrm{M}^{(l_3l_2l_1)}_{\mathbf{k}_3,\mathbf{k}_2,\mathbf{k}_1}. \tag{4.43}$$

Most dominant contributions to the decay of the Higgs mode stem from $\Sigma_{11}^{(b)}(i\omega_n)$. This part corresponds to the Beliaev damping process where one Higgs mode with zero momentum collapses into two NG modes with opposite momenta $\mathbf{k}$ and $-\mathbf{k}$ with satisfying the on-shell energy and momentum conservation, i.e., $\mathcal{E}_{1,\mathbf{0}} - \mathcal{E}_{2,\mathbf{k}} - \mathcal{E}_{2,-\mathbf{k}} = 0$. The Beliaev damping is a fundamental decay process of the Higgs mode in the Bose–Hubbard systems. This type of damping of the Higgs mode has been studied in some literature, in which its damping rate is calculated for $n_0 \gg 1$ at zero temperature [24] and at nonzero temperatures [14]. In particular, in the former article by Altman and Auerbach [24], the zero-temperature damping rate was calculated by combining the effective pseudspin-1 model approach and Fermi's golden rule.

In our previous study on the basis of the finite-temperature quantum field theory [14], we have calculated the damping rate $\Gamma \equiv -\mathrm{Im}\Sigma_{11}(i\omega_n)|_{i\omega_n\to\omega+i\epsilon}$ only at a resonant position $\omega = \mathcal{E}_{1,\mathbf{0}} = \Delta$ in order to qualitatively estimate the stability of the Higgs mode in experimental systems. Our results presented in this Thesis generalize this analysis such that the real and imaginary parts of the self-energy function are taken into account even at off-resonant frequencies. In particular, the real part of this function gives a mass renormalization to the mean-field Higgs gap due to the interactions between collective modes.

The contributions shown in Fig. 4.2 include some processes with an odd number of NG modes. Such terms should vanish if one takes a large filling limit $n_0 \gg 1$

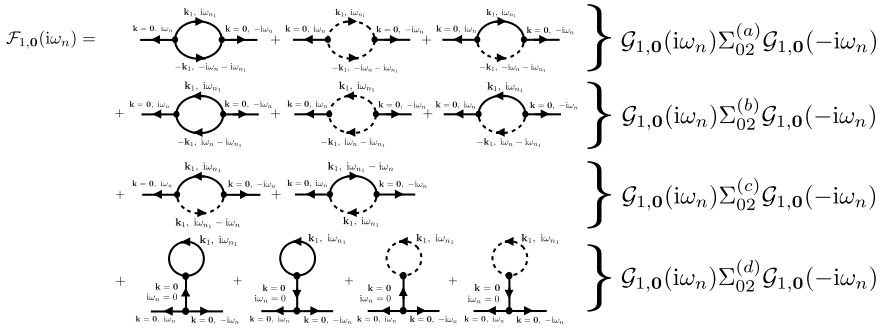

Fig. 4.3 Leading 1-loop order contributions to the anomalous Green's function $\mathcal{F}_{1,\mathbf{0}}(i\omega_n)$ and corresponding self-energy functions. The diagrams in each column form an individual group labeled by $\Sigma_{02}^{(a)}(i\omega_n)$, $\Sigma_{02}^{(b)}(i\omega_n)$, $\Sigma_{02}^{(c)}(i\omega_n)$, or $\Sigma_{02}^{(d)}(i\omega_n)$. See also Fig. 4.2. (This figure is reproduced from Ref. [25]. Copyright © 2018 American Physical Society. All rights reserved)

because the explicit particle-hole symmetry is restored at this limit. The self energy $\Sigma_{11}^{(c)}$ becomes relevant at $n_0 \sim 1$ and gives a thermal effect on the damping of the Higgs mode. The corresponding exchange process of collective excitations can be regarded as a Landau-type damping of the Higgs mode with absorbing an NG mode from a *thermal cloud* and emitting a Higgs mode. In Ref. [14], it has been reported that an interacting NG-mode propagator with a non-zero momentum shows a similar damping, for which an injected NG mode attenuates into a Higgs mode via interactions with a thermal cloud of NG modes. For further information about physics of the Landau damping of collective excitations in Bose–Einstein condensates, see, e.g., Ref. [18].

As well as the normal part, one can obtain the anomalous self energy $\Sigma_{02}(i\omega_n)$ within the leading order perturbation, and separate it into four parts: $\Sigma_{02}(i\omega_n) = \Sigma_{02}^{(a)}(i\omega_n) + \Sigma_{02}^{(b)}(i\omega_n) + \Sigma_{02}^{(c)}(i\omega_n) + \Sigma_{02}^{(d)}(i\omega_n)$. The contributions to this function are expressed in Fig. 4.3. Each diagram appearing in $\Sigma_{02}(i\omega_n)$ formally has the same structure as the corresponding one of $\Sigma_{11}(i\omega_n)$, except for the details of the interaction vertices connecting with external lines. A direct calculation leads to the following analytical expression of the separated functions:

$$
\begin{aligned}
\Sigma_{02}^{(a)}(i\omega_n) = &-\frac{1}{2N}\sum_{\mathbf{k}_1\in\Lambda_0} \mathrm{M}^{[333]}_{\mathbf{0},\mathbf{k}_1,-\mathbf{k}_1}\mathrm{M}^{[311]}_{\mathbf{0},\mathbf{k}_1,-\mathbf{k}_1}\frac{1+2n_{\mathrm{B}}[\mathcal{E}_{1,\mathbf{k}_1}]}{i\omega_n+2\mathcal{E}_{1,\mathbf{k}_1}} \\
&-\frac{1}{2N}\sum_{\mathbf{k}_1\in\Lambda_0} \mathrm{M}^{[344]}_{\mathbf{0},\mathbf{k}_1,-\mathbf{k}_1}\mathrm{M}^{[322]}_{\mathbf{0},\mathbf{k}_1,-\mathbf{k}_1}\frac{1+2n_{\mathrm{B}}[\mathcal{E}_{2,\mathbf{k}_1}]}{i\omega_n+2\mathcal{E}_{2,\mathbf{k}_1}} \\
&-\frac{1}{N}\sum_{\mathbf{k}_1\in\Lambda_0} \mathrm{M}^{[344]}_{\mathbf{0},\mathbf{k}_1,-\mathbf{k}_1}\mathrm{M}^{[312]}_{\mathbf{0},\mathbf{k}_1,-\mathbf{k}_1}\frac{1+n_{\mathrm{B}}[\mathcal{E}_{1,\mathbf{k}_1}]+n_{\mathrm{B}}[\mathcal{E}_{2,\mathbf{k}_1}]}{i\omega_n+\mathcal{E}_{1,\mathbf{k}_1}+\mathcal{E}_{2,\mathbf{k}_1}}, \qquad (4.44)\\
\Sigma_{02}^{(b)}(i\omega_n) = &\ \frac{1}{2N}\sum_{\mathbf{k}_1\in\Lambda_0} \mathrm{M}^{[311]}_{\mathbf{0},\mathbf{k}_1,-\mathbf{k}_1}\mathrm{M}^{[333]}_{\mathbf{0},\mathbf{k}_1,-\mathbf{k}_1}\frac{1+2n_{\mathrm{B}}[\mathcal{E}_{1,\mathbf{k}_1}]}{i\omega_n-2\mathcal{E}_{1,\mathbf{k}_1}}
\end{aligned}
$$

$$+\frac{1}{2N}\sum_{\mathbf{k}_1\in\Lambda_0}\mathrm{M}^{[322]}_{\mathbf{0},\mathbf{k}_1,-\mathbf{k}_1}\mathrm{M}^{[344]}_{\mathbf{0},\mathbf{k}_1,-\mathbf{k}_1}\frac{1+2n_{\mathrm{B}}[\mathcal{E}_{2,\mathbf{k}_1}]}{i\omega_n-2\mathcal{E}_{2,\mathbf{k}_1}}$$

$$+\frac{1}{N}\sum_{\mathbf{k}_1\in\Lambda_0}\mathrm{M}^{[312]}_{\mathbf{0},\mathbf{k}_1,-\mathbf{k}_1}\mathrm{M}^{[334]}_{\mathbf{0},\mathbf{k}_1,-\mathbf{k}_1}\frac{1+n_{\mathrm{B}}[\mathcal{E}_{1,\mathbf{k}_1}]+n_{\mathrm{B}}[\mathcal{E}_{2,\mathbf{k}_1}]}{i\omega_n-\mathcal{E}_{1,\mathbf{k}_1}-\mathcal{E}_{2,\mathbf{k}_1}}, \tag{4.45}$$

$$\Sigma^{(c)}_{02}(i\omega_n)=-\frac{1}{N}\sum_{\mathbf{k}_1\in\Lambda_0}\mathrm{M}^{[332]}_{\mathbf{0},\mathbf{k}_1,\mathbf{k}_1}\mathrm{M}^{[344]}_{\mathbf{0},\mathbf{k}_1,\mathbf{k}_1}\frac{n_{\mathrm{B}}[\mathcal{E}_{1,\mathbf{k}_1}]-n_{\mathrm{B}}[\mathcal{E}_{2,\mathbf{k}_1}]}{i\omega_n+\mathcal{E}_{2,\mathbf{k}_1}-\mathcal{E}_{1,\mathbf{k}_1}}$$

$$-\frac{1}{N}\sum_{\mathbf{k}_1\in\Lambda_0}\mathrm{M}^{[341]}_{\mathbf{0},\mathbf{k}_1,\mathbf{k}_1}\mathrm{M}^{[332]}_{\mathbf{0},\mathbf{k}_1,\mathbf{k}_1}\frac{n_{\mathrm{B}}[\mathcal{E}_{2,\mathbf{k}_1}]-n_{\mathrm{B}}[\mathcal{E}_{1,\mathbf{k}_1}]}{i\omega_n+\mathcal{E}_{1,\mathbf{k}_1}-\mathcal{E}_{2,\mathbf{k}_1}}, \tag{4.46}$$

$$\Sigma^{(d)}_{02}(i\omega_n)=-\frac{1}{N}\sum_{\mathbf{k}_1\in\Lambda_0}\mathrm{M}^{[333]}_{\mathbf{0},\mathbf{0},\mathbf{0}}\mathrm{M}^{[311]}_{\mathbf{k}_1,\mathbf{k}_1,\mathbf{0}}\frac{1}{\Delta}n_{\mathrm{B}}[\mathcal{E}_{1,\mathbf{k}_1}]$$

$$-\frac{1}{N}\sum_{\mathbf{k}_1\in\Lambda_0}\mathrm{M}^{[331]}_{\mathbf{0},\mathbf{0},\mathbf{0}}\mathrm{M}^{[331]}_{\mathbf{0},\mathbf{k}_1,\mathbf{k}_1}\frac{1}{\Delta}n_{\mathrm{B}}[\mathcal{E}_{1,\mathbf{k}_1}]$$

$$-\frac{1}{N}\sum_{\mathbf{k}_1\in\Lambda_0}\mathrm{M}^{[333]}_{\mathbf{0},\mathbf{0},\mathbf{0}}\mathrm{M}^{[421]}_{\mathbf{k}_1,\mathbf{k}_1,\mathbf{0}}\frac{1}{\Delta}n_{\mathrm{B}}[\mathcal{E}_{2,\mathbf{k}_1}] \tag{4.47}$$

$$-\frac{1}{N}\sum_{\mathbf{k}_1\in\Lambda_0}\mathrm{M}^{[331]}_{\mathbf{0},\mathbf{0},\mathbf{0}}\mathrm{M}^{[423]}_{\mathbf{k}_1,\mathbf{k}_1,\mathbf{0}}\frac{1}{\Delta}n_{\mathrm{B}}[\mathcal{E}_{2,\mathbf{k}_1}].$$

An analytical evaluation of the momentum summation for each self-energy function is impossible in practice. Instead, in our analysis, we numerically compute the retarded (or analytically continued) self-energy functions for the real-time propagators, such as $\Sigma^{\mathrm{R}}_{11}(\omega)=\Sigma_{11}(i\omega_n)|_{i\omega_n\to\omega+i\epsilon}$, for a fixed frequency after replacing the summation with the corresponding integral, i.e., $\sum_{\mathbf{k}_1\in\Lambda_0}\to\int_{-\pi}^{\pi}\int_{-\pi}^{\pi}\int_{-\pi}^{\pi}dk_xdk_y dk_z/(2\pi)^3$. As the integration scheme, we have chosen the standard trapezoidal rule in a three-dimensional lattice space with a sufficiently large number of lattices. Once the self-energy functions are numerically obtained, we can calculate the dynamical susceptibilities $\chi_{KK}(\omega)$ and $\chi_{OO}(\omega)$ as functions of frequency with use of the formulae (4.36) and (4.37).

4.4 Numerical Results

In this section, we show a numerical evaluation of the dynamical susceptibilities that can be written in terms of the self-energy functions computed perturbatively. To argue the stability of the Higgs mode in experiments, we focus especially on the imaginary part of the susceptibility, which is nothing else but the spectral function for the Higgs mode. In this Thesis, we present only the results when the kinetic-energy modulation is applied because, as mentioned in Sect. 4.3, the response function of this modulation completely coincides with that of the onsite-interaction modulation, at least, within our spin-wave approximation.

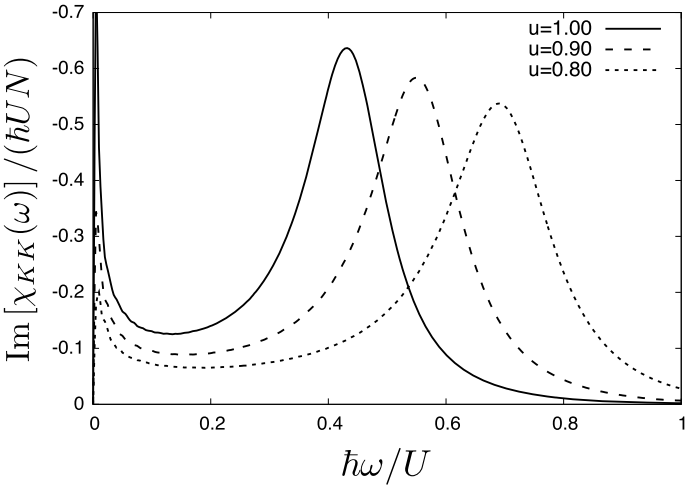

Fig. 4.4 Dynamical susceptibility at unit filling $n_0 = 1$ and at zero temperature. The resonance peak position increases away from the critical point $u_c \approx 1.457$. (This figure is reproduced from Ref. [25]. Copyright © 2018 American Physical Society. All rights reserved)

4.4.1 Response Functions in the Uniform System

In this subsection, we show the imaginary part of the dynamical susceptibility subject to no trapping potential in order to discuss the broadening of the resonance peak solely due to quantum and thermal fluctuations. Figure 4.4 displays a curve corresponding to Im $[\chi_{KK}(\omega)]$ at the unit filling rate and at zero temperature. There, one can observe that a Lorentzian-like curve appears and exhibits a sufficiently sharp resonance peak corresponding to the Higgs mode. The center position of the peak defines a Higgs gap, which is renormalized due to the interactions. The peak width corresponds to the damping rate of the Higgs mode and takes a relatively small value compared with the mass gap. The existence of such a sharp resonance peak implies that the Higgs mode in the 3D system is stable within the lowest order correction of quantum fluctuations. In addition, the position of the peak is shifted to the high-ω side as the dimensionless parameter u leaves from the mean-field critical point $u = u_c$. Table 4.1 shows each value of the renormalized Higgs gap Δ_* scaled by the corresponding Mott gap Δ_{MI}, which has a same relative distance from the critical point, $\bar{u}_{\mathrm{rel}} = |u - u_c|/u_c$, as that of the Higgs gap. To make the gap dimensionless, we used the mean-field Mott gap $\Delta_{\mathrm{MI}} = \sqrt{U^2 - 2JzU(2n_0 + 1) + (Jz)^2}$, which is derived in Ref. [12].

We also see the similar behavior at a large filling rate $n_0 \gg 1$ as shown in Fig. 4.5. Figure 4.5 draws the frequency dependence of Im $[\chi_{KK}(\omega)]$ at a large filling rate and at zero temperature. The width of this peak approximately coincides with the damping rate evaluated by using Fermi's golden rule at a large filling rate [24]. It should be noted that one can find another peak near $\omega = 0$, which does not correspond to the Higgs mode. Such an additional peak also appears in Fig. 4.4, i.e., in the case

Table 4.1 Numerical values of the renormalized Higgs gap Δ_* scaled by the Mott gap Δ_{MI}. The energy scales Δ_* and Δ_{MI} locate at a same relative distance $\bar{u}_{\mathrm{rel}}$ from $u_c \approx 1.457$. Here, u_o (u_d) is the corresponding value of u at a given $\bar{u}_{\mathrm{rel}} = |u - u_c|/u_c$ in the ordered-superfluid (disordered-insulator) side. (This table is reproduced from Ref. [25]. Copyright © 2018 American Physical Society. All rights reserved.)

$\Delta_*/\Delta_{\mathrm{MI}}$	$\Delta/\Delta_{\mathrm{MI}}$	$\bar{u}_{\mathrm{rel}}$	u_o	u_d
0.890	1.081	0.314	1.000	1.914
1.057	1.206	0.382	0.900	2.014
1.251	1.359	0.451	0.800	2.114

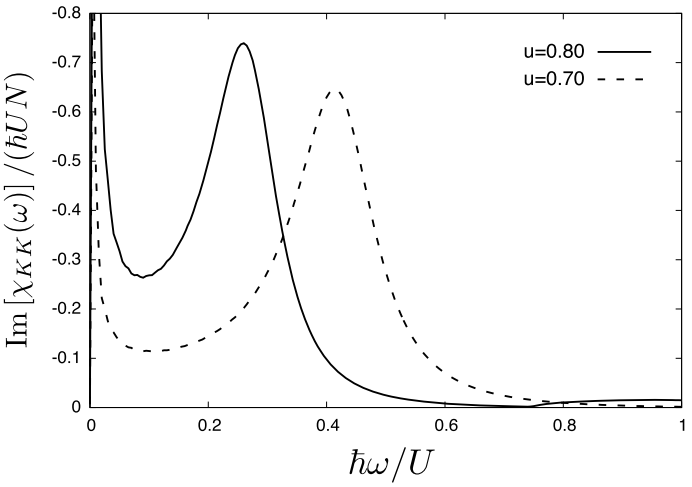

Fig. 4.5 Dynamical susceptibility at a large filling rate $n_0 \gg 1$ and at zero temperature. In this case, the critical point is at $u = u_c = 1$. (This figure is reproduced from Ref. [25]. Copyright © 2018 American Physical Society. All rights reserved)

of unit filling. This peak can be interpreted as an artifact of our method based on the perturbative expansion around the mean-field limit. In fact, the real parts of the self-energy functions become as large as the mean-field Higgs gap near $\omega = 0$. This means that the corrections to the Higgs gap, which are produced by the perturbative expansion of the spin waves, are no longer small compared with the zeroth-order value of the energy gap. In other words, it turns out that our perturbative approximation of the response function breaks down especially near $\omega = 0$. Nevertheless, around the renormalized Higgs-peak position at $\omega = \Delta_*$, the corrections are sufficiently small compared to the mean-field gap Δ. This means that our approach is valid around the Higgs-gap energy scale, which we are especially interested in. For the $(3 + 1)$-dimensional relativistic O(N) scalar model in quantum field theory, a similar breakdown of the perturbation theory and leading to an additional peak near zero frequency happen as a result of the logarithmic infrared divergence of the self-energy function [26]. We have to emphasize that in contrast to the infrared divergence of the

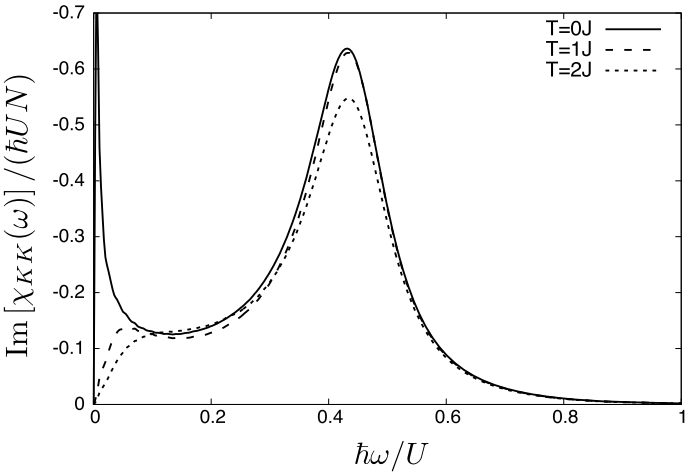

Fig. 4.6 Dynamical susceptibility at unit filling $n_0 = 1$ and at typical temperatures, especially for $u = 1$ ($zJ/U = 0.25$). The temperature is measured by units of J. (This figure is reproduced from Ref. [25]. Copyright © 2018 American Physical Society. All rights reserved)

self-energy function, our naive perturbation approach fails to capture the logarithmic corrections that appear as a result of renormalization of the marginal terms [27]. Such a careful renormalization treatment has not been done in our analysis.

Next, we incorporate nonzero-temperature effects on the susceptibility. Figure 4.6 shows several susceptibilities at $u = 1$ and at different temperatures until $T = 2J$. This result means that the thermal fluctuation only makes the peak width slightly broader. The resonance peak in the spectral function is therefore quite robust against thermal fluctuations at sufficiently low temperatures. It should be noted that the temperature of real experiments is typically of order J. Hence, we conclude that the Higgs resonance peak survives in the unit-filling spectral function even at typical temperatures. Our result in three dimensions is in contrast to the case of the two-dimensional (2D) Bose–Hubbard model. Pollet and Prokof'ev numerically computed the spectral function associated with the kinetic-energy modulation by means of quantum Monte-Carlo simulations [6]. Their result implies that the resonance of the Higgs mode becomes rather broad due to quantum and thermal fluctuations even when the system is supposed to be uniform.

It is worth noting that in Ref. [14] the damping rate of the Higgs mode with zero momentum has been calculated analytically and numerically by using the finite-temperature field theoretical method at large filling and shows that the Higgs mode in three dimensions is sufficiently stable against thermal fluctuations at typical temperatures of experiments. The finite-temperature susceptibility shown in Fig. 4.6 extends this large filling result to more realistic cases as the setup of Ref. [2].

4.4.2 Effects of a Trapping Potential

Here we incorporate the non-uniform trapping-potential effects within the local density approximation (LDA). As a specific shape of the trapping potential, we assume a parabolic and isotropic potential, which is given by

$$V_{\rm trap}(r) = \frac{m\omega_0^2}{2} r^2, \tag{4.48}$$

where m is the atomic mass and ω_0 is the frequency of the potential. We note that the center of the trap at $r = 0$ corresponds to a largest occupation over the whole system. According to the conventional LDA [20], the effect of the inhomogeneity is approximately treated by the general formula

$$\chi_{\rm lda}(\omega) = 4\pi \int_0^R dr r^2 \bar{n}'[\mu(r)] \chi_{\rm unif}[\omega, \mu(r)]. \tag{4.49}$$

Here, $\chi_{\rm unif}(\omega, \mu)$ is the bulk susceptibility, which is either Eqs. (4.3) or (4.5) divided by the factor N and computed at a fixed chemical potential. Within LDA, the potential leads to a spatially-dependent chemical-potential shift as $\mu(r) = \mu_{n_0} - V_{\rm trap}(r)$. The weight function for this averaging is given by $\bar{n}'[\mu]$, which is normalized such that

$$\bar{n}'[\mu(r)] = \frac{\bar{n}[\mu(r)]}{4\pi \int_0^R dr r^2 \bar{n}[\mu(r)]}, \tag{4.50}$$

where the integration upper bound, R, indicates the radius of the spherical region, in which atoms are perturbed by the temporal modulation of J or U. $\bar{n}[\mu(r)]$ is the local density of atoms at radial distance r. When the modulation is applied to the whole system, R should be equal to the Thomas–Fermi (TF) radius $R_{\rm TF}$, at which the density vanishes. In what follows, we assume that at the trap center the density is tuned to unity, i.e., $\bar{n}[\mu_{n_0}] = n_0 = 1$.

4.4.3 Response Functions at $R = R_{\rm TF}$

We analyze the response function to the global J or U modulation of the whole system. In this case, the radial integral in Eq. (4.49) is done from $R = 0$ to $R = R_{\rm TF}$.

Figure 4.7a shows the ω dependence of Im $[\chi_{\rm lda}(\omega)]$ at $T = 0$ and $u = 1$. In the same plot, we also display the spectral function in the absence of the potential (4.48). One can observe that the resonance peak, which would be rather sharp without the trapping potential, is significantly broadened due to the inhomogeneity effect so that the peak width is as large as the Higgs gap $\Delta_{\rm H}$. In this sense, one can no longer regard the response as a well-defined resonance peak. Figure 4.7b is a magnified scale plot of the same LDA susceptibility.

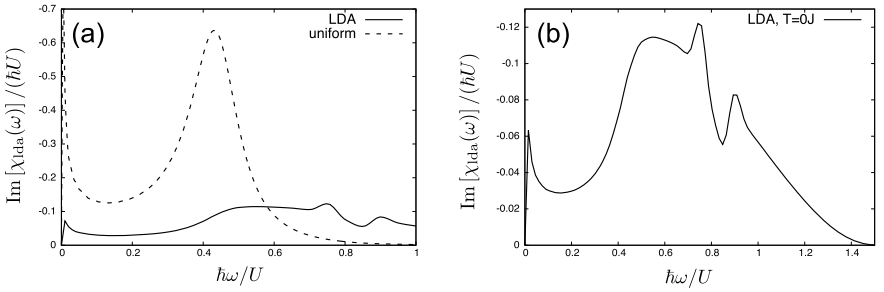

Fig. 4.7 **a** Comparison of susceptibilities computed for trapped (solid line) and homogeneous (dashed line) systems at $T = 0$ and $u = 1$. At the trap center, the atomic density is tuned to unity, i.e., $n_0 = 1$. **b** Magnifying the dynamical susceptibility of the trapped system at $T = 0$. In order to obtain a smooth line from a finite number of LDA data, we have used the spline interpolation method. (This figure is reproduced from Ref. [25]. Copyright © 2018 American Physical Society. All rights reserved)

The broadening of the resonance peak can be attributed to that when we apply the modulation globally to the whole system, all the subsystems corresponding to $\bar{n} \in [0, 1]$ contribute to the resulting response. Specifically, the gap at $\bar{n} < 1$ is larger than that at $\bar{n} = 1$ and the high-energy contributions far from the trapping center obscure the well-defined Higgs resonance.

In Fig. 4.7b, we also find a fine structure of the response in the region of $0.7U < \omega < 1.0U$. This structure means that the response of the bulk gapful mode at a certain value of μ, which gives $\Delta_{\mathrm{H}} \simeq 0.75U$ $(0.85U)$, is locally strong (weak). It is interesting to examine in future experiments whether or not the emergence of the fine structure is an artifact of LDA.

While the resonance peak in the response is completely smeared out by the non-uniform trap, a characteristic feature of the Higgs mode in the bulk is still visible in the averaged susceptibility of the trapped system. Specifically, the onset frequency of the response is almost equal to the bulk Higgs gap at $\bar{n} = 1$. This property has been found also in the 2D quantum Monte-Carlo simulation [6] and indeed utilized to measure the Higgs gap in the quantum-gas microscope experiment [2].

4.4.4 Responses Around the Trapping Center

In this subsection, we investigate responses of the system to a partial modulation, which excites atoms only inside the spherical region characterized by the condition $R < R_{\mathrm{TF}}$. This type of modulation technique allows one to eliminate undesired contributions from the low-density area that broaden the resonance of the Higgs mode. A similar analysis in two dimensions has been done in Ref. [4]. In what follows, we set $u = 1$ corresponding to the stable Higgs mode in the uniform case.

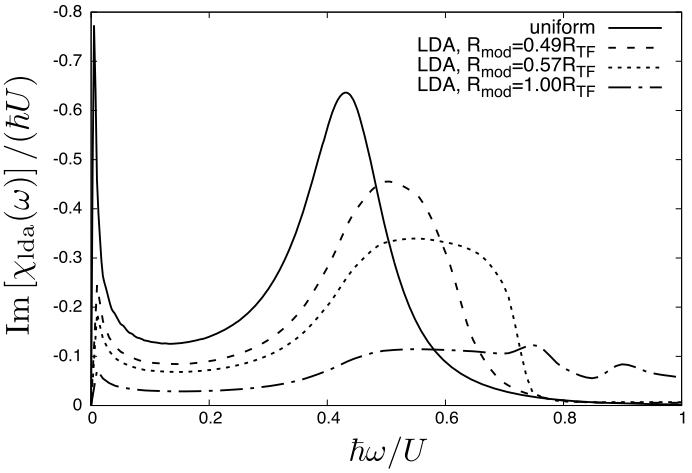

Fig. 4.8 Dynamical susceptibility for the trapped system, where the atoms are partially modulated with $R_{\rm mod}/R_{\rm TF} = 0.49$ (dashed line), 0.57 (dotted line), and 1.00 (dashed-dotted line), respectively. The susceptibility approaches the uniform result (solid line) when we take the limit of $R_{\rm mod} \to 0$. Here, we set $u = 1$ ($zJ/U = 0.25$) and $T/J = 0$. The filling factor at the trap center is tuned to unity ($n_0 = 1$). (This figure is reproduced from Ref. [25]. Copyright © 2018 American Physical Society. All rights reserved)

We define the radius for the partial modulation as $R_{\rm mod}$. In the units of $R_{\rm TF}$, the modulation radius $R_{\rm mod}$ reads

$$\frac{R_{\rm mod}}{R_{\rm TF}} = \sqrt{\frac{\mu_{n_0} - \mu_{\rm mod}}{\mu_{n_0} - \mu_{\rm TF}}}, \tag{4.51}$$

where $\mu_{\rm mod} = \mu(R_{\rm mod})$ and $\mu_{\rm TF} = \mu(R_{\rm TF})$. In particular, one can easily verify that $\mu_{\rm TF} = -0.75U$ for $u = 1$. The LDA calculation is nothing else but putting $R = R_{\rm mod}$ in Eq. (4.49).

Figure 4.8 shows Im $[\chi_{\rm lda}(\omega)]$ as a function of ω at zero temperature for different values of $R_{\rm mod}$. When $R_{\rm mod}/R_{\rm TF} = 0.49$, the modulation is added to a subregion of $\bar{n} \geq 0.90$. In this case, the shape of the resonance peak in the resulting response function is well approximated as a Lorentzian function and the peak width is clearly smaller than the peak position. In other words, for this modulation radius, the response is still a sharp resonance peak. We also find that the peak position is slightly shifted to the high-energy side due to the contribution from the low-density region.

When $R_{\rm mod}/R_{\rm TF}$ is increased, the response becomes broader to approach the result at $R_{\rm mod} = R_{\rm TF}$ (See the dash-dotted line in Fig. 4.8). When $R_{\rm mod}/R_{\rm TF} = 0.57$, at which a subregion of $\bar{n}(r) \geq 0.85$ is modulated, the response is significantly broader than that of $R_{\rm mod}/R_{\rm TF} = 0.49$ and the shape of the response function noticeably deviates from a Lorentzian function. Thus, our results indicate that the condition that $R_{\rm mod} < 0.5R_{\rm TF}$ is required for a sharp resonance peak to be observed.

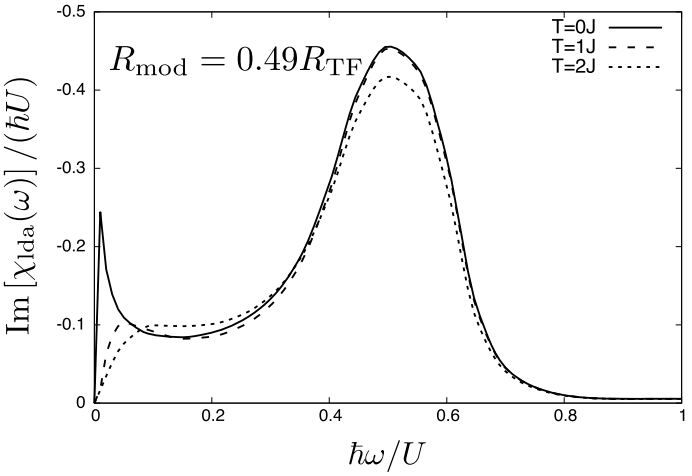

Fig. 4.9 Finite-temperature effects on the dynamical susceptibility of the trapped system at $u = 1$ and $R_{\mathrm{mod}}/R_{\mathrm{TF}} = 0.49$. The distinct lines correspond to $T/J = 0$ (solid line), $T/J = 1$ (dashed line), and $T/J = 2$ (dotted line), respectively. At the trap center, the atomic density is tuned to unity ($n_0 = 1$). (This figure is reproduced from Ref. [25]. Copyright © 2018 American Physical Society. All rights reserved)

For the case of $R_{\mathrm{mod}}/R_{\mathrm{TF}} = 0.49$, let us consider finite-temperature effects on the LDA susceptibility of the partial modulation. Each line plotted in Fig. 4.9 is the result at a temperature until $T = 2J$. Our results reveal that even in the presence of the trap potential, the resonance peak is robust against thermal fluctuations at typical temperatures of order J. This kind of robustness to thermal fluctuations is not related with the specific choice of R_{mod} because the similar feature can be observed in the uniform cases. According to this result, it is expected that one can detect and identify the well-defined resonance of the Higgs mode in a 3D Bose gas system trapped by a parabolic potential. The detection procedure requires a partial modulation of J or U over a radius $R_{\mathrm{mod}} \leq R_{\mathrm{TF}}$, and it is, in principle, possible in real experiments. Here we emphasize that the tendency of the temperature dependence in 3D systems is distinct from that in 2D systems [4]. In 2D systems, it has been numerically verified that the response function of a partial modulation significantly depends on the temperature. It means that the Higgs-mode peak in two dimensions is obscured due to thermal fluctuations when $T > J$ even for partial modulations.

4.5 Summary of This Chapter

In conclusion of this chapter, we performed a field theoretical analysis of the linear response functions for the 3D Bose–Hubbard model and investigated the combined effects of quantum and thermal fluctuations, and inhomogeneous parabolic trapping

potential on the detectability of a sharp Higgs-mode resonance in actual experiments. The uniform susceptibility, which has been numerically evaluated at unit filling, showed that the Higgs-mode resonance can survive as a sharp peak in the dynamical susceptibility even at typical temperatures of experiments until $T = 2J$. The parabolic-potential effect on the response function has been treated within LDA. The LDA result indicated that the resonance peak is significantly broadened due to the trapping potential when the global modulations are applied to the system. In order to remove the undesired continuum hiding the Higgs mode resonance, we performed a partial modulation around the trap center and looked at the resulting response. The results subject to $R_{\mathrm{mod}} < 0.5R_{\mathrm{TF}}$ exhibited that the Higgs mode can exist as a well-defined resonance at typical temperatures.

References

1. T. Stöferle, H. Moritz, C. Schori, M. Köhl, T. Esslinger, Phys. Rev. Lett. **92**, 130403 (2004)
2. M. Endres, T. Fukuhara, D. Pekker, M. Cheneau, P. Schauβ, C. Gross, E. Demler, S. Kuhrm, I. Bloch, Nature **487**, 454 (2012)
3. M. Endres, *Probing correlated quantum many-body systems at the single-particle level*, Ph. D. thesis, Ludwig-Maximilians-Universität München (2013)
4. L. Liu, K. Chen, Y. Deng, M. Endres, L. Pollet, N. Prokof'ev, Phys. Rev. B **92**, 174521 (2015)
5. D. Pekker, C.M. Varma, Ann. Rev. Condens. Matter Phys. **6**, 269 (2015)
6. L. Pollet, N. Prokof'ev, Phys. Rev. Lett. **109**, 010401 (2012)
7. P.O. Fedichev, Y. Kagan, G.V. Shlyapnikov, J.T.M. Walraven, Phys. Rev. Lett. **77**, 2913 (1996)
8. M. Theis, G. Thalhammer, K. Winkler, M. Hellwig, G. Ruff, R. Grimm, J.H. Denschlag, Phys. Rev. Lett. **93**, 123001 (2004)
9. R. Yamazaki, S. Taie, S. Sugawa, Y. Takahashi, Phys. Rev. Lett. **105**, 050405 (2010)
10. D.M. Bauer, M. Lettner, C. Vo, G. Rempe, S. Dürr, Nat. Phys. **5**, 339 (2009)
11. L.W. Clark, L.-C. Ha, C.-Y. Xu, C. Chin, Phys. Rev. Lett. **115**, 155301 (2015)
12. S.D. Huber, E. Altman, H.P. Büchler, G. Blatter, Phys. Rev. B **75**, 085106 (2007)
13. A.L. Chernyshev, M.E. Zhitomirsky, Phys. Rev. B **79**, 144416 (2009)
14. K. Nagao, I. Danshita, Prog. Theor. Exp. Phys. **2016**, 063I01 (2016)
15. A. Griffin, Phys. Rev. B **53**, 9341 (1996)
16. T. Kita, J. Phys. Soc. Jpn. **75**, 044603 (2006)
17. V.I. Yukalov, H. Kleinert, Phys. Rev. A **73**, 063612 (2006)
18. C.J. Pethick, H. Smith, *Bose-Einstein Condensation in Dilute Gases* (Cambridge University Press, Cambridge, 2008)
19. N. Shohno, Prog. Theor. Phys. **31**, 553 (1964)
20. L. Pitaevskii, S. Stringari, *Bose-Einstein Condensation* (Oxford University Press, NewYork, 2003)
21. A.A. Abrikosov, L.P. Gorkov, I.E. Dzyaloshinski, *Methods of Quantum Field Theory in Statistical Physics* (Dover Publications, New York, 1975)
22. E.M. Lifshitz, L. Pitaevskii, *Statistical Physics, Part 2* (Pergamon, Oxford, 1980)
23. A. Altland, B.D. Simons, *Condensed Matter Field Theory*, 2nd edn. (Cambridge University Press, Cambridge, 2010)
24. E. Altman, A. Auerbach, Phys. Rev. Lett. **89**, 250404 (2002)
25. K. Nagao, Y. Takahashi, I. Danshita, Phys. Rev. A **97**, 043628 (2018)
26. N. Dupuis, Phys. Rev. E **83**, 031120 (2011)
27. I. Affleck, G.F. Wellman, Phys. Rev. B **46**, 8934 (1992)

Chapter 5
Semiclassical Quench Dynamics of Bose Gases in Optical Lattices

Abstract This chapter is devoted to presenting applications of the truncated Wigner approximation to far-from-equilibrium many-body dynamics explored in the quantum simulator. We analyze redistribution dynamics of the kinetic and local interaction energies after a sudden quantum quench in the three-dimensional Bose–Hubbard model starting with a strongly-correlated Mott insulator state. Applying the semiclassical method, we also investigate quantum quench dynamics of spatial correlation functions for interacting lattice bosons in two dimensions. We focus especially on the initial state dependence of such dynamics observed in early-time processes of correlation functions.

5.1 Far-from-Equilibrium Dynamics of the Bose–Hubbard Model

In the previous chapter, we investigated dynamical properties of the optical lattice system described by the Bose–Hubbard model near thermal equilibrium states. This chapter is dedicated to studying more complex dynamics, namely, far-from-equilibrium many-body dynamics of the Bose–Hubbard model in two and three dimensions.

The system that we are focusing on is supposed to be completely isolated from any external baths, so that the dynamics of its quantum state, which is represented by the density operator $\hat{\rho}$, are the unitary time evolution described by the von-Neumann equation for the Bose–Hubbard Hamiltonian

$$i\hbar\frac{\partial}{\partial t}\hat{\rho}(t) = [\hat{H}, \hat{\rho}(t)], \quad \hat{H} = -J\sum_{\langle j,k\rangle}(\hat{a}_j^\dagger\hat{a}_k + \text{H.c.}) + \frac{U}{2}\sum_j \hat{a}_j^\dagger\hat{a}_j^\dagger\hat{a}_j\hat{a}_j. \quad (5.1)$$

Notice that when the initial state at $t = 0$ is prepared in a pure state, this equation reduces to the Schrödinger equation, which governs the unitary time evolution of the many-body wave function. For a conserved atomic number N_{tot} and total lattice number M, the number of the possible Fock states belonging to the relevant Hilbert space $\mathcal{H}_{N_{\text{tot}},M}$ is counted [1] as

K. Nagao, *Fluctuations and Non-Equilibrium Phenomena in Strongly-Correlated Ultracold Atoms*, Springer Theses, https://doi.org/10.1007/978-981-15-7171-8_5

$$\dim \mathcal{H}_{N_{\rm tot},M} = \frac{(N_{\rm tot}+M-1)!}{(M-1)!N_{\rm tot}!}. \tag{5.2}$$

It indicates that components of the state vector that must be stored in the memory of computers grow exponentially as $N_{\rm tot}$ and M increase. This type of computational complexity makes it difficult to treat many-body dynamics of macroscopic interacting models as realized in ultracold-atomic quantum simulators. To simulate the time evolution governed by the quantum-mechanical linear equations with classical computers, one has to bring an approximate treatment to reduce such exponentially many degrees of freedom to algebraically many ones.

To reduce such a complexity in two and three dimensions, in this Thesis, we adopt the semiclassical truncated Wigner approximation (TWA), which has been already reviewed in Chap. 3. Within TWA, one solves Hamilton's equation with M numbers of complex field, instead of directly treating the density operator or wave function represented in $\mathcal{H}_{N_{\rm tot},M}$. The quantum average of an operator $\hat{\Omega}$ at time t is given by a weighed integration of the corresponding c-number function Ω_W over the phase space:

$$\langle \hat{\Omega}(t) \rangle \approx \int d\boldsymbol{\alpha}_0 d\boldsymbol{\alpha}_0^* W_0(\boldsymbol{\alpha}_0, \boldsymbol{\alpha}_0^*) \Omega_W[\boldsymbol{\alpha}_{\rm cl}(t), \boldsymbol{\alpha}_{\rm cl}^*(t)]. \tag{5.3}$$

For the Bose–Hubbard model, the classical trajectory $\boldsymbol{\alpha}_{\rm cl}(t)$ is a solution of the following Hamilton equation, obeying an initial condition $\boldsymbol{\alpha}_{\rm cl}(t=0) = \boldsymbol{\alpha}_0$ weighted with the Wigner function W_0:

$$\begin{aligned} i\hbar \frac{\partial \alpha_{{\rm cl},j}}{\partial t} &= \frac{\partial H_W(\boldsymbol{\alpha}_{\rm cl}, \boldsymbol{\alpha}_{\rm cl}^*)}{\partial \alpha_{{\rm cl},j}^*}, \\ &= -J \sum_{\langle k \rangle_j} \alpha_k + U|\alpha_j|^2 \alpha_j - U\alpha_j, \end{aligned} \tag{5.4}$$

$$H_W = -J \sum_{\langle j,k \rangle} (\alpha_j^* \alpha_k + \text{c.c.}) + \frac{U}{2} \sum_j \left(|\alpha_j|^4 - 2|\alpha_j|^2 + \frac{1}{2} \right). \tag{5.5}$$

where $\langle k \rangle_j$ means all nearest-neighbor sites connected to the site j. One can say that this is a discrete-type Gross–Pitaevskii equation. The total conserved number $N_{\rm tot}$ enters into a parameter controlling the semiclassical expansion. In the current case, it is nothing else but the inverse of the atomic density per site $\bar{n} = N_{\rm tot}/M$.

The Bose–Hubbard model has a weakly fluctuating regime, where its interaction parameter $\lambda \equiv U\bar{n}/J$ is far from the quantum phase transition point λ_c, i.e., $\lambda \ll \lambda_c$. There, the TWA quantitatively captures quantum dynamics of the system until the time t approaches a characteristic timescale t_c [2–4]. When λ is close to the critical value λ_c, the semiclassical treatment breaks down at short time due to the strong fluctuations. Since $\lambda_c \propto \bar{n}^2$, larger $\bar{n}$ and/or smaller U/J implies larger t_c [3, 4]. We note that the semiclassical approximation becomes exact especially at $U/J = 0$ or $\bar{n} = \infty$.

In typical experiments including the three-dimensional (3D) experiment [5], which we discuss in Sect. 5.3, $\bar{n}$ is tuned to unity and λ is $O(1)$. If one computes time evolution of the one-dimensional (1D) Bose–Hubbard model with $\bar{n} = 1$ and $\lambda \sim 1$ within the TWA, it fails in much shorter time than $O(\hbar/J)$ because of rather small $\lambda_c (= 3.367)$ [6]. In contrast, for the 3D case with the same parameters, it is expected that the TWA is able to simulate the dynamics up to $t \sim \hbar/J$, because λ of $O(1)$ is sufficiently far from $\lambda_c = 29.34$ [7]. As we will see in Sect. 5.3, the TWA can reproduce characteristic early-time dynamics observed in the experiment [5] until $t \sim \hbar/J$.

5.2 Experimental Details

In this section, we summarize the experimental setup of quench dynamics implemented by Ref. [5]. In the laboratory, as a first step, one prepares a Bose–Einstein condensate of ultracold ^{174}Yb atoms in a cubic optical lattice with lattice spacing $d_{\mathrm{lat}} = 266$ nm. The setup has the recoil energy $E_{\mathrm{R}}/\hbar = 2\pi \times 4021.18$ Hz, which gives a characteristic energy scale of this system. In the experiment, measuring non-equilibrium dynamics of the system has been done according to the following steps:

1. **Preparing the initial state:** Starting from the prepared Bose–Einstein condensate, the optical lattice depth V_0 is adiabatically ramped up to $V_0 = 15E_{\mathrm{R}}$ ($U/J = 99.4$), at which atoms can form a Mott-insulator state. The filling factor of atoms per site is tuned to almost unity over the whole system. The total number of atoms is typically of the order of 10^4 [5].
2. **Decreasing the lattice depth:** To prepare a far-from-equilibrium state of atoms, one abruptly ramps down the lattice depth from $V_0 = 15E_{\mathrm{R}}$ to $V_0 = 5E_{\mathrm{R}}$. The time during the ramp-down process is $t_{\mathrm{f}} = 0.1$ ms. The final lattice depth implies $U/J = 3.41$. For this interaction strength, the ground state is in the deep superfluid regime, where the system is sufficiently far from the quantum critical point [7].
3. **Measuring time evolutions:** The non-equilibrium state after the ramp-down process can evolve towards an equilibrium state in time. One measures the time evolution after the quench through the kinetic and onsite-interaction energies, respectively. These are macroscopic quantities denoted by

$$\hat{K} = -J \sum_{\langle j,k \rangle} (\hat{a}_j^\dagger \hat{a}_k + \mathrm{H.c.}), \quad \hat{O} = \frac{U}{2} \sum_j \hat{a}_j^\dagger \hat{a}_j^\dagger \hat{a}_j \hat{a}_j. \tag{5.6}$$

   The expectation values of these quantities are extracted from the time-of-flight imaging and the high-resolution atom-number-projection spectroscopy, respectively.

In the real setup, there is a parabolic potential to trap the atomic gas. In our analysis presented later, we ignore the effects due to such a non-uniform trap. The reason is

as follows: At the initial Mott-insulator state, the atomic density is almost uniform in space so that the initial quantum state is well approximated as a direct-product wave function, which is spatially uniform and composed of a local Fock state. Moreover, the trapping potential gives no noticeable effect on the quench dynamics within the time window $t \lesssim \hbar/J$, in which the experiment was performed. This is because the trap frequency is much smaller than $J/\hbar$. For details, see Ref. [5].

5.3 Numerical Simulation of the Redistribution Dynamics

In this section, we explain details of our numerical simulation for the redistribution dynamics. Using the results shown in Chap. 3 and above, we obtain approximate expectation values of $\hat{K}$ and $\hat{O}$ at time t, given by

$$\langle \hat{K}(t) \rangle \approx \int d\boldsymbol{\alpha}_0 d\boldsymbol{\alpha}_0^* W(\boldsymbol{\alpha}_0, \boldsymbol{\alpha}_0^*) K_W \left[\boldsymbol{\alpha}_{\rm cl}(t), \boldsymbol{\alpha}_{\rm cl}^*(t) \right], \tag{5.7}$$

$$\langle \hat{O}(t) \rangle \approx \int d\boldsymbol{\alpha}_0 d\boldsymbol{\alpha}_0^* W(\boldsymbol{\alpha}_0, \boldsymbol{\alpha}_0^*) O_W \left[\boldsymbol{\alpha}_{\rm cl}(t), \boldsymbol{\alpha}_{\rm cl}^*(t) \right]. \tag{5.8}$$

Here,

$$K_W(\boldsymbol{\alpha}, \boldsymbol{\alpha}^*) = -J \sum_{\langle j,k \rangle} \left[\alpha_j^* \alpha_k + \text{c.c.} \right], \tag{5.9}$$

$$O_W(\boldsymbol{\alpha}, \boldsymbol{\alpha}^*) = \frac{U}{2} \sum_j \left[|\alpha_j|^4 - 2|\alpha_j|^2 + \frac{1}{2} \right]. \tag{5.10}$$

are the Weyl symbols of $\hat{K}$ and $\hat{O}$, respectively.

Here we note the derivation of $K_W(\boldsymbol{\alpha}, \boldsymbol{\alpha}^*)$ and $O_W(\boldsymbol{\alpha}, \boldsymbol{\alpha}^*)$ for an exercise. The shortest way could be employing the Bopp-operator representation of the Bose operators $\hat{a}_j$ and $\hat{a}_j^\dagger$, which have been introduced in Chap. 3. In fact, with use of the Bopp operators, $\hat{a}_j^\dagger \hat{a}_k$ and $\hat{a}_j^\dagger \hat{a}_j^\dagger \hat{a}_j \hat{a}_j$ are mapped to a classical function such that

$$\begin{aligned} \hat{a}_j^\dagger \hat{a}_k &\to \left(\alpha_j^* - \frac{1}{2} \frac{\partial}{\partial \alpha_j} \right) \alpha_k \\ &= \alpha_j^* \alpha_k - \frac{1}{2} \delta_{j,k}, \end{aligned} \tag{5.11}$$

$$\begin{aligned} \hat{a}_j^\dagger \hat{a}_j^\dagger \hat{a}_j \hat{a}_j &\to \left(\alpha_j^* - \frac{1}{2} \frac{\partial}{\partial \alpha_j} \right) \left(\alpha_j^* - \frac{1}{2} \frac{\partial}{\partial \alpha_j} \right) \alpha_j^2 \\ &= |\alpha_j|^4 - 2|\alpha_j|^2 + \frac{1}{2}. \end{aligned} \tag{5.12}$$

The resulting functions are noting else but Eqs. (5.9) and (5.10). Adding these ones, we also obtain H_W in Eq. (5.5).

As seen in Sect. 5.1, the initial state before the quench is represented by a product-state wave function $|\Psi_{\rm ini}\rangle = \prod_j |\bar{n}\rangle_j$. Here $|\bar{n}\rangle_j$ is the number-definite Fock vector characterized by $\hat{n}_j|\bar{n}\rangle_j = \bar{n}|\bar{n}\rangle_j$. The corresponding Wigner function $W_{\rm M}(\boldsymbol{\alpha}, \boldsymbol{\alpha}^*)$ is given by a direct product of the local Wigner function of the Fock-state vector $|\bar{n}\rangle_j$ at each site, which was presented in Chap. 3. Thus, the Wigner function of the initial state reads [4, 8–10]

$$W_{\rm M}(\boldsymbol{\alpha}, \boldsymbol{\alpha}^*) = \prod_j 2e^{-2|\alpha_j|^2}(-1)^{\bar{n}} L_{\bar{n}}(4|\alpha_j|^2), \tag{5.13}$$

where $L_n(x) = \sum_{r=0}^{n}(-1)^r \frac{n!}{(n-r)!(r!)^2}x^r$ is the Laguerre polynomial of order n. The classical field is parametrized as $\alpha_j = |\alpha_j|e^{i\varphi_j}$. This Wigner function is obviously not positive along the amplitude direction $|\alpha_j|$, except for a trivial case $\bar{n} = 0$. The phase of the classical field φ_j distributes uniformly in $[0, 2\pi]$. The Wigner function has an explicit U(1) symmetry reflecting the restored symmetry inside the Mott-insulator state. In fact, an arbitrary phase rotation for the phase-space variables, $\alpha_j \to \alpha_j e^{i\tilde{\varphi}_j}$, does not affect the Wigner function.

To calculate the expectation values in Eqs. (5.7) and (5.8), one has to evaluate the phase-space integration weighted with $W_{\rm M}(\boldsymbol{\alpha}, \boldsymbol{\alpha}^*)$. Typically, that is performed based on a Monte-Carlo simulation using random numbers. The negativity of Eq. (5.13) implies that the numerical Monte-Carlo integration requires many samples to reach a converged result because the positive and negative parts can cancel each contribution during the numerical sampling. To reduce such a difficulty, we adopt a Gaussian Wigner function for the Fock state [8, 9]. Repeating the discussions in the previous works [8, 9], the function for the Fock vector $|\bar{n}\rangle$ has a general form as

$$W_{\rm g}(n) = \frac{1}{\sqrt{2\pi\sigma^2}} e^{-\frac{1}{2\sigma^2}(n-n_0)^2}, \tag{5.14}$$

where $n = |\alpha|^2$. The mean n_0 and covariance σ are free parameters determined from the condition that the Gaussian function should exactly recover the first and second order local moments of the density, i.e., $\langle \hat{n}_j \rangle$ and $\langle \hat{n}_j^2 \rangle$. Direct calculations lead to the following optimal choice:

$$n_0 = \bar{n} + \frac{1}{2}, \quad \sigma = \frac{1}{2}. \tag{5.15}$$

It is worth noting that the (rescaled) higher-order moments $\bar{n}^{-m}\langle \hat{n}_j^m \rangle$ for $m > 2$ computed by the Gaussian function agree with the exact ones up to $O(\bar{n}^{-2})$ [9]. While the normalized Gaussian function gives rise to an unphysical negative density, however, it does not affect the phase-space average itself because the probability, which corresponds to the Gaussian tail, is sufficiently small even at $\bar{n} = 1$. Similar treat-

ments based on such a Gaussian ansatz are often used in TWA simulations starting from several initial states [4, 8, 9, 11–14]. These studies manifest the validity of the Gaussian approximation in describing short-time semiclassical dynamics within the accuracy of TWA. Recently, an efficient numerical sampling scheme based on the discrete-Wigner representation by Wootters [15] has been proposed beyond the Gaussian approximation [16]. This method is basically applicable to systems with a finite-dimensional Hilbert space such as spin-1/2 systems or two level systems. However, we do not use this approach in this Thesis.

Now we summarize what should be done by using TWA in order to simulate the experimental dynamics: We solve time evolutions of a time-dependent Bose–Hubbard model $\hat{H}[\lambda(t)]$ by using the TWA. At $t = 0$, the Hamiltonian has $\lambda = \lambda_{\rm i} = 99.4$ corresponding to $V_0 = 15E_{\rm R}$. In the ramp-down process, $\lambda(t)$ decreases with $V_0(t)$, which declines linearly. Recall that the duration of the ramp-down process is $t_{\rm f} = 0.1$ ms in the experiment. At $t = t_{\rm f}$, the lattice depth reaches $V_0 = 5E_{\rm R}$, which implies $\lambda = \lambda_{\rm f} = 3.41$. At $t > t_{\rm f}$, the system evolves in time under the time-independent Hamiltonian $\hat{H}[\lambda_{\rm f}]$. The phase-space averaging with the Wigner function is evaluated by using the Monte-Carlo integration, where each initial configuration of the classical fields, $\boldsymbol{\alpha}_{\rm cl}(0)$, is randomly chosen from the Gaussian-Wigner function (5.14).

5.3.1 Sudden Ramp-Down Limit

Before proceeding to a numerical simulation corresponding to the experimental setup, we discuss a simpler problem, i.e., an infinitesimal-time limit of the ramp-down process ($t_{\rm f} = 0$). In this case, the Hamiltonian is always independent of time at $t > 0$. Accordingly, the semiclassical dynamics are governed by the post-quenched classical Hamiltonian starting from a certain initial state.

Figure 5.1 depicts a numerical simulation of the kinetic and interaction energies within TWA for $t_{\rm f} = 0$, where we set $N_{\rm tot} = M = 12^3 = 1728$ and assume an open boundary condition. To integrate the Gross–Pitaevskii equation, we adopted the fourth-order explicit Runge–Kutta method with a sufficiently small time step. We clearly see that the semiclassical approach captures fast redistribution of the kinetic and interaction energies even at the level of the sudden quench limit. The timescale of the redistribution is on the order of 0.1 ms and comparable to the experimental result. In addition, the sum of the energies, i.e., $E_{\rm tot} = \langle \hat{K}(t) \rangle + \langle \hat{O}(t) \rangle$ completely maintains its initial value because the Hamiltonian of the system is independent of time.

We note that the numerical curves in Fig. 5.1 have an estimation error due to the Monte-Carlo sampling. In this simulation, we sampled $n_{\rm mc} = 100\,000$ random classical fields according to Eq. (5.14). Because the standard error of the sampling scales with $1/\sqrt{n_{\rm mc}}$, we do not display numerical error bars, which are sufficiently small.

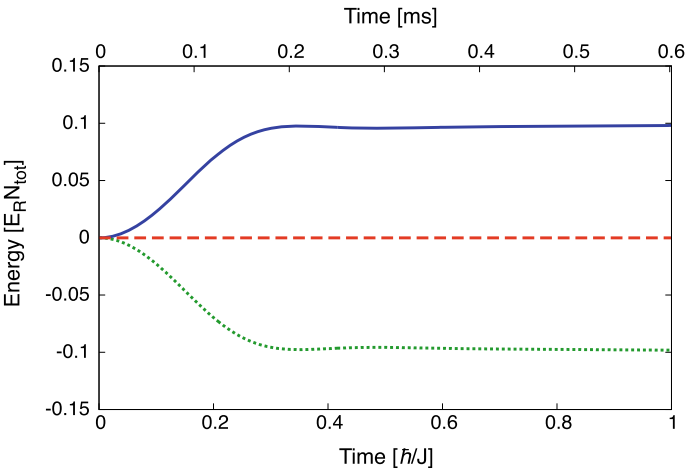

Fig. 5.1 TWA dynamics of the kinetic and onsite-interaction energies (green-dotted and blue-solid lines) after the sudden quench from the singly-occupied Mott-insulator state. The red-dashed line represents the total sum of these energies. The finite-time ramp down process is not included in this simulation ($t_\mathrm{f} = 0$). We set $N_\mathrm{tot} = M = 12^3$ and $\lambda_\mathrm{f} = 3.41$. and note 0.6 ms $\approx \hbar/J$, where J is the hopping amplitude after the quench. (This figure is reproduced from Ref. [17]. Copyright)

We emphasize that the redistribution dynamics such as Fig. 5.1 cannot be recreated by means of naive mean-field theories without fluctuations. Those include the mean-field Gross–Pitaevskii theory, in which the dynamics are described as a single realization of trajectory in the coherent-state phase space, and the Gutzwiller variational method, in which the many-body wave function is approximately represented as a direct product state over the whole lattice. Intuitively, the initial noise perturbing the classical field plays a role of initial seed to push the system into the superfluid side.

5.3.2 *Finite-Time Ramp-Down Process*

To simulate the actual setup, we take into account the finite-time ramp-down process in $V_0(t)$. The hopping strength J and the onsite-interaction strength U vary with $V_0(t)$ as depicted in Fig. 5.2. We note again that $V_0(t)$ linearly decreases in time from $V_0(0) = 15E_\mathrm{R}$ to $V_0(t_\mathrm{f}) = 5E_\mathrm{R}$ where $t_\mathrm{f} = 0.1$ ms. In this process, the system passes through the Mott-insulating and the quantum critical regimes where the quantitative validity of TWA is justified only in rather short time $t \ll O(\hbar/J)$. Nevertheless, our approach is expected to be able to explain the redistribution dynamics after the quench because the system actually leaves away from these regimes in the short time.

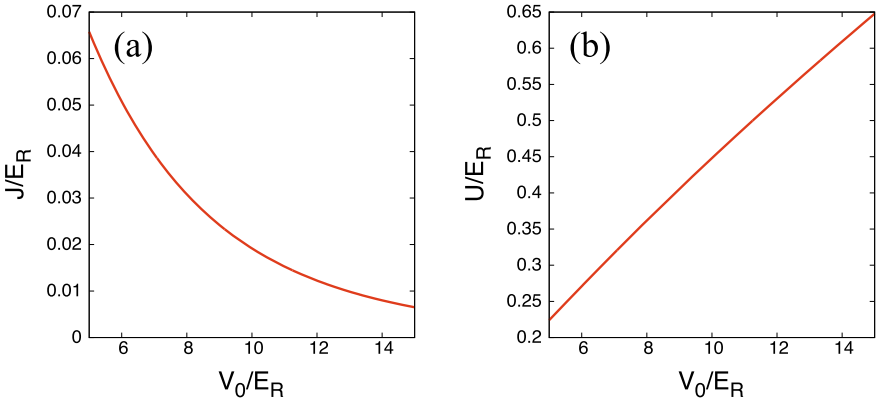

Fig. 5.2 Lattice-depth dependence of (a) the hopping strength J and (b) the onsite-interaction strength U, respectively. The horizontal axis, V_0, means the lattice depth. To measure the energies, we used the units of the recoil energy E_R. (This figure is reproduced from Ref. [17]. Copyright © 2019 American Physical Society. All rights reserved.)

In Fig. 5.3, we show TWA results of $\langle \hat{K}(t) \rangle$ and $\langle \hat{O}(t) \rangle$ including the ramp-down process. The numerical simulation is performed with an open boundary condition and at $M = N_{\rm tot} = 30^3 = 27\,000$, which is comparable to the size of the actual system. To obtain a converged result, we sampled $n_{\rm mc} = 10\,000$ initial conditions according to Eq. (5.14). Compared with the sudden-limit calculation, the ramp-down process significantly modifies the value of each energy at $t = t_{\rm f}$. The total energy $E_{\rm tot}$ decreases from zero. In addition, the timescale for the saturation toward each quasi-steady value is slightly diminished. Due to such modifications, the semiclassical result including the ramp-down process agrees very well with the experimental one, which is presented by points with error bars in Fig. 5.3, without any additional fitting parameters. The original experimental data are extracted from Ref. [5]. The detailed experimental setup will be provided in Ref. [5].

We conclude this section by making comments on the limitation of our semiclassical approach to the experimental system at intermediate final interactions and at unit filling. Although the experiment is able to access a long-time regime $t \gg \hbar/J$, our approach is limited to simulate only short time dynamics up to $t \sim \hbar/J$. For the long time dynamics, the approximate representation, i.e., many realizations of the deterministic Gross–Pitaevskii trajectories that are not affected by quantum jumps, is no longer valid because higher-order corrections to the TWA become more important. Developing a quantitative and reliable tool allowing to reach quantum thermalization after long time evolutions remains to be a challenging issue.

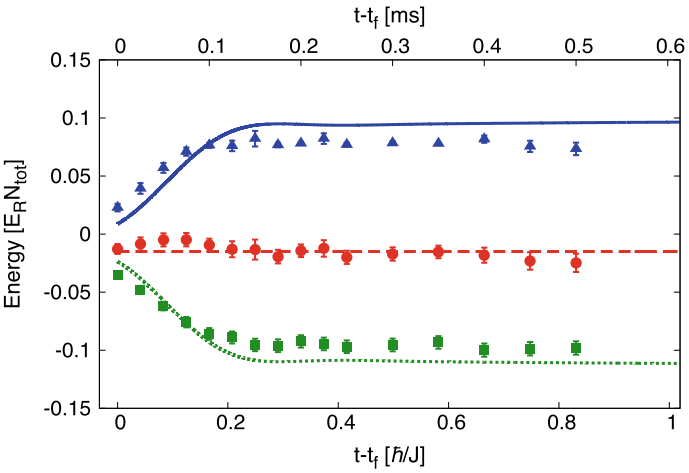

Fig. 5.3 TWA dynamics of the kinetic and onsite-interaction energies (green-dotted and blue-solid lines) including the finite-time ramp-down process of the lattice depth. The red-dashed line represents the total sum of these energies. The initial state is the singly-occupied insulator state. We set $N_{\mathrm{tot}} = M = 30^3$ and $\lambda_{\mathrm{f}} = 3.41$ for this simulation. The horizontal axis starts from $t = t_{\mathrm{f}}$. The green-square, blue-triangular, and red-circle points represent the corresponding experimental data of the ensemble-averaged kinetic, onsite-interaction, and total energies. The vertical bar for each point indicates an experimental error. (This figure is reproduced from Ref. [17]. Copyright © 2019 American Physical Society. All rights reserved.)

5.4 Correlation Propagation Over a Two-Dimensional Lattice

The direct comparison performed in Sect. 5.3 corroborated the quantitative validity of the TWA method for the sudden quench dynamics of the weakly-interacting ($\lambda \ll \lambda_c$) 3D system with the Mott-insulator initial state. In this section, we apply our approach to investigate different quench dynamics, i.e., time evolutions of equal-time correlation functions after sudden quenches in the 2D Bose–Hubbard model. In particular, we focus on two different initial states, i.e., a coherent state, which corresponds to the ground state at $\lambda = 0$, and a Mott-insulator state. We study their difference seen in the quench dynamics inside a weakly interacting regime.

We specifically deal with a density-density correlation function at equal time, which is defined by

$$C_d(t) = \frac{1}{M\bar{n}^2} \sum_j \langle \hat{n}_j(t)\hat{n}_{j+d}(t)\rangle_c, \tag{5.16}$$

where $d = (d_x, d_y)$ is a relative vector between two different sites. The bracket $\langle \cdots \rangle_c$ indicates a connected correlation function, i.e., $\langle \hat{n}_j(t)\hat{n}_{j+d}(t)\rangle_c = \langle \hat{n}_j(t)\hat{n}_{j+d}(t)\rangle - \langle \hat{n}_j(t)\rangle\langle \hat{n}_{j+d}(t)\rangle$. Within TWA, the connected correlator is approximated to

$$\langle \hat{n}_j(t)\hat{n}_{j+d}(t)\rangle_c \approx \overline{n_W^{(j)}(t)n_W^{(j+d)}(t)} - \overline{n_W^{(j)}(t)} \cdot \overline{n_W^{(j+d)}(t)}, \tag{5.17}$$

where the overline in the right-hand side means the phase-space average by means of the Wigner function of either coherent state or insulator state. The averaged c-number quantity $n_W^{(j)}$ represents the Wigner–Weyl transform of the local density $\hat{n}_j$, i.e., $n_W^{(j)} = |\alpha_j|^2 - \frac{1}{2}$. In cold-atomic experiments, non-equilibrium dynamics of the non-local density-density correlation are measurable by utilizing the quantum-gas microscope technique [18] or measuring spatial-noise correlations in a time-of-flight interference pattern of expanding gases [19, 20].

5.4.1 Quench from a Coherent State

Let us start from analyzing correlation spreading assuming that the system is initially in a direct-product state composed of the local coherent states $|\bar{\alpha}\rangle_j = e^{\bar{\alpha}\hat{a}_j^\dagger - \bar{\alpha}^*\hat{a}_j}|0\rangle$:

$$|\Psi_{\rm ini}\rangle = \prod_j |\bar{\alpha}\rangle_j. \tag{5.18}$$

Here, $\bar{\alpha} = \sqrt{\bar{n}}e^{i\bar{\varphi}}$ parametrizes each coherent-state vector. According to the results in Chap. 3, the corresponding Wigner function is given by

$$W_{\rm coh}(\boldsymbol{\alpha}, \boldsymbol{\alpha}^*) = \prod_j \left\{ 2e^{-2|\alpha_j - \bar{\alpha}|^2} \right\}. \tag{5.19}$$

This distribution is always positive reflecting the *classicality* of the coherent state. Therefore, for this initial state, there is no difficulty in the Monte-Carlo sampling of the random initial states. In what follows, we set $\bar{\varphi} = 0$ for simplicity.

We note here some details of our numerical setup. As the filling factor of the whole system, we specifically choose $\bar{n} = 10$. This means that the semiclassical dynamics is accurate for a relatively long time scale with units of $\hbar/J = 1$. The lattice geometry is square with $M = 20^2$ sites and its boundary is periodic. The quench is supposed to be abruptly done, so that the Hamiltonian is independent of time.

Before proceeding to our main results, we calculate the energy deviation per site defined by

$$\frac{1}{M}\Delta E = \frac{1}{M}\left[\langle \Psi_{\rm ini}|\hat{H}_{\rm f}|\Psi_{\rm ini}\rangle - \langle \hat{H}_{\rm f}\rangle_{\rm g} \right], \tag{5.20}$$

where $\hat{H}_{\rm f}$ is the post-quench Hamiltonian at $\lambda = \lambda_{\rm f}$ and $\langle \hat{H}_{\rm f}\rangle_{\rm g}$ means the ground-state energy of $\hat{H}_{\rm f}$. This is nothing but the excitation energy density measured from the ground state in the post-quenched Hamiltonian side. One can evaluate $\langle \hat{H}_{\rm f}\rangle_{\rm g}$ within

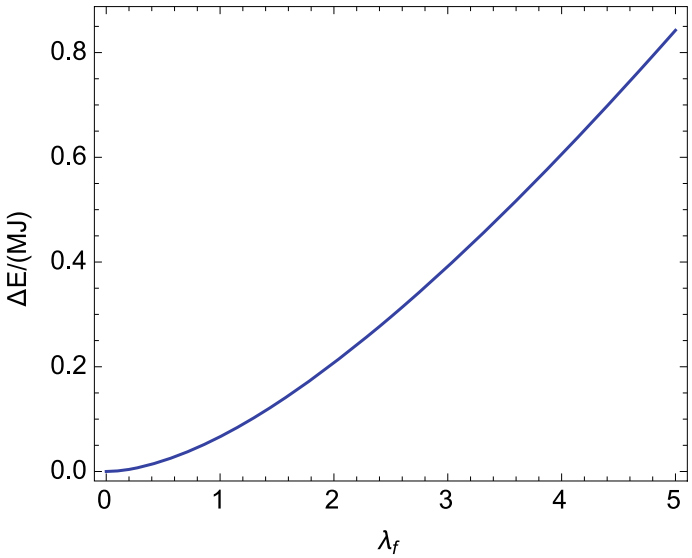

Fig. 5.4 Energy deviation per site between the coherent state and the ground state of the post-quench Hamiltonian within the Bogoliubov approximation. $\Delta E/(MJ)$ is given as a function of $\lambda_{\rm f}$, where $\bar{n} = 10$. (This figure is reproduced from Ref. [17]. Copyright © 2019 American Physical Society. All rights reserved.)

the standard Bogoliubov approximation for the Bose–Hubbard model and the results is given as follows:

$$\langle \hat{H}_{\rm f} \rangle_{\rm g} \approx M \left[\mathcal{E}_0 + \frac{1}{2M} \sum_{\mathbf{p} \neq 0} (E_{\mathbf{p}} - \hbar\omega_{\mathbf{p}}) \right], \tag{5.21}$$

where $\mathbf{p} = (p_x, p_y)$ is a momentum in the first Brillouin zone, $\mathcal{E}_0 = -4J\bar{n} + U\bar{n}^2/2$, and $\hbar\omega_{\mathbf{p}} = U\bar{n} + 4J \sum_{j=x,y} \sin^2[p_j d_{\rm lat}/(2\hbar)]$. In addition, $E_{\mathbf{p}} = \sqrt{(\hbar\omega_{\mathbf{p}})^2 - (\bar{n}U)^2}$ is the energy of the elementary excitations (for more details, see Ref. [21]). Figure 5.4 shows $\Delta E/(MJ)$ of the coherent state as a function of $\lambda_{\rm f}$. Because $\Delta E/M$ is lesser than the typical energy scale J over a wide range of $\lambda_{\rm f}$, the dynamics after the quench from the coherent state is dominated by the low-energy elementary excitations kicked from the ground state. These are referred to as the Bogoliubov quasiparticle in non-relativistic broken-symmetry phases.

Figure 5.5 monitors how density-density correlations propagate over the square lattice. In the numerical simulation, we set $\lambda_{\rm f} = 2$. To characterize the correlation spreading, we introduce the standard Euclidean distance defined by $d_{\rm E} \equiv (d_x^2 + d_y^2)^{1/2}$ as a metric of the geometry, rather than the Manhattan distance. The time evolution indicates that a characteristic signal of correlation, i.e., a wave packet enveloping maximum (blue circle) and minimum (green square) peaks of a fine oscil-

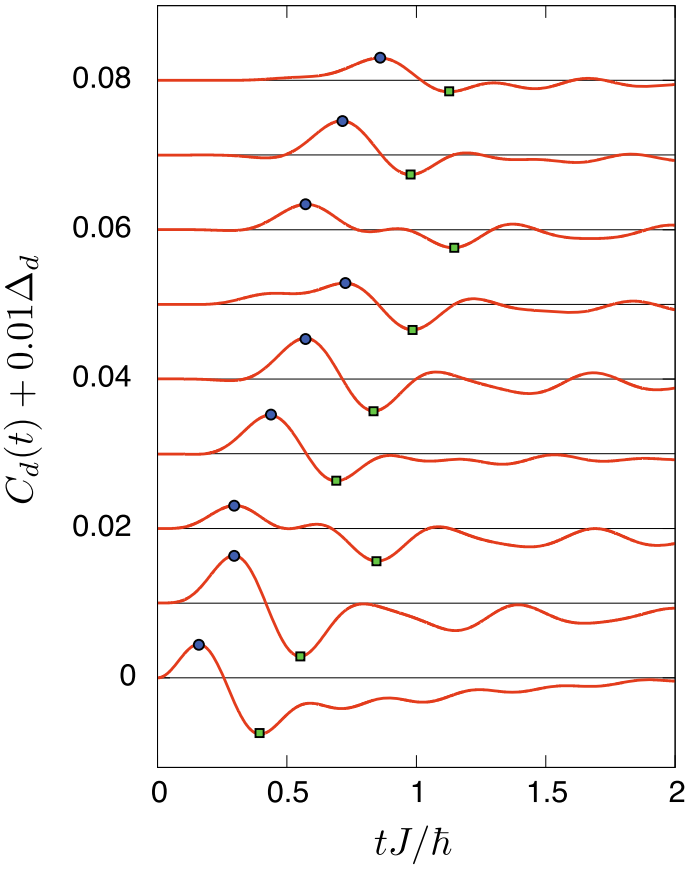

Fig. 5.5 TWA simulation of the density-density correlation function after the quench from the coherent state at $\lambda_f = 2$. The blue circle and green square indicate the maximum and minimum values of the correlation function within $tJ/\hbar \leq 3$. The relative vector $d = (d_x, d_y)$, Euclidean distance d_E, and offset of correlation Δ_d take values of $(d_x, d_y; d_E; \Delta_d) = (0, 1; 1.00; 0)$, $(1, 1; 1.41; 1)$, $(0, 2; 2.00; 2)$, $(1, 2; 2.24; 3)$, $(2, 2; 2.83; 4)$, $(0, 3; 3.00; 5)$, $(1, 3; 3.16; 6)$, $(2, 3; 3.617)$, $(0, 4; 4.00; 8)$ from the bottom to top, respectively. In this simulation, we sampled $n_{mc} = 40\,000$ initial conditions according to Eq. (5.19). (This figure is reproduced from Ref. [17]. Copyright © 2019 American Physical Society. All rights reserved.)

lation propagates over the 2D lattice in time. Such a fine oscillation can be interpreted as a quasi-coherent oscillation reflecting that a few elementary excitations are created by the quench.

To quantify and characterize the correlation spreading in the square lattice, we define a propagation velocity of the wave packet as follows: Let us focus on peak times of the maximum and minimum values of the correlation. We express them as t_+ and t_-, which are the blue circles and the green squares in Fig. 5.5. For a given

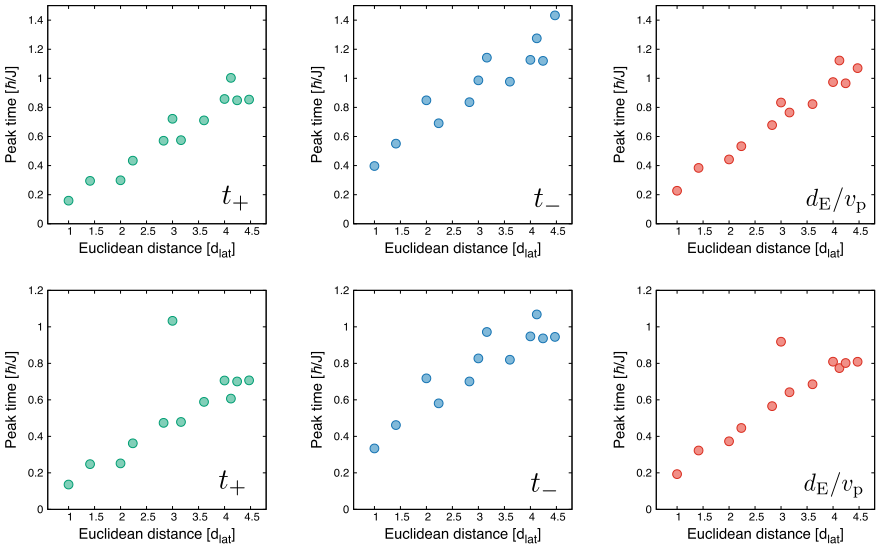

Fig. 5.6 Maximum (left column), minimum (center column) and averaged (right column) peak times extracted from the numerical simulations. The vertical and horizontal axes express the peak time and Euclidean distance. The upper and lower rows correspond to $\lambda_{\rm f} = 2$ and $\lambda_{\rm f} = 4$, respectively. (This figure is reproduced from Ref. [17]. Copyright © 2019 American Physical Society. All rights reserved.)

Euclidean distance $d_{\rm E}$, a reasonable (instantaneous) propagation velocity $v_{\rm p}$ would be a harmonic average of these peak times such that

$$v_{\rm p} \equiv \frac{d_{\rm E}}{2}\left(\frac{1}{t_+} + \frac{1}{t_-}\right), \tag{5.22}$$

where $d_{\rm E}/v_{\rm p}$ is regarded as an averaged peak time. Figure 5.6 displays t_+, t_-, and $d_{\rm E}/v_{\rm p}$ for different distances at $\lambda_{\rm f} = 2$ and $\lambda_{\rm f} = 4$, respectively. We find the tendency that the averaged peak time almost linearly increases with $d_{\rm E}$. Performing a linear fitting of the averaged peak times, one can obtain a mean propagation velocity, denoted by $\bar{v}_{\rm p}$, of the wave packet. For computing $\bar{v}_{\rm p}$, we have taken into account early twelve peaks within $t \sim \hbar/J$, which correspond to $C_d(t)$ with $d_{\rm E} < 5d_{\rm lat}$.

In Fig. 5.7, we show the mean propagation velocity $\bar{v}_{\rm p}$ as a function of the final interaction $\lambda_{\rm f}$ as well as twice the maximum and sound velocities of the Bogoliubov excitations, $2v_{\rm m}$ and $2v_{\rm s}$, which are defined by

$$v_{\rm m} = \max_{\mathbf{p}}\left\{\sqrt{\left(\frac{\partial E_{\mathbf{p}}}{\partial p_x}\right)^2 + \left(\frac{\partial E_{\mathbf{p}}}{\partial p_y}\right)^2}\right\}, \quad v_{\rm s} = \lim_{\mathbf{p}\to\mathbf{0}}\left\{\sqrt{\left(\frac{\partial E_{\mathbf{p}}}{\partial p_x}\right)^2 + \left(\frac{\partial E_{\mathbf{p}}}{\partial p_y}\right)^2}\right\}.$$

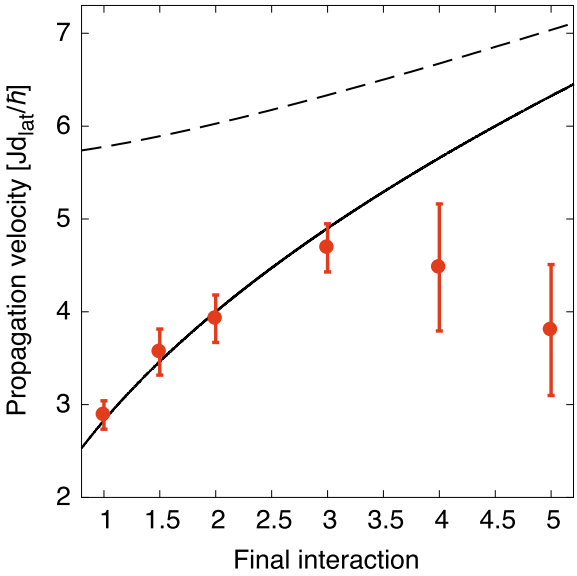

Fig. 5.7 Final interaction (λ_f) dependence of the mean propagation velocity $\bar{v}_p$ (circle). The solid and dashed lines represent twice the sound ($2v_s$) and maximum ($2v_m$) velocities of the Bogoliubov excitation, respectively. The vertical bar indicates the normal estimation error of the mean propagation velocity in the linear fitting (see also Fig. 5.6). (This figure is reproduced from Ref. [17]. Copyright © 2019 American Physical Society. All rights reserved.)

We note that v_m coincides with v_s in the deep quench limit, i.e., $\lambda_f \gg 1$. It is clearly seen in Fig. 5.7 that the mean velocity $\bar{v}_p$ is bounded by twice the maximum velocity $2v_m$ over a range of $\lambda_f \in [1, 5]$. This result is consistent with the general statement of the Lieb–Robinson bound for interacting lattice models [22]. Furthermore, in the relatively shallow quench regime $1 \leq \lambda_f \leq 3$, the propagation velocity increases with λ_f in such a way that the points come close to $2v_s$. This feature can be attributed to the fact that the sudden quench actually generates some elementary excitations at $E_{\mathbf{p}} \ll J$, where the Bogoliubov excitations behave as phonons, because the excitation energy density is relatively small (see Fig. 5.4).

In contrast, in the range of $3 < \lambda_f \leq 5$, the mean propagation velocity significantly deviates from the lower side blanch $2v_s$. There, Bogoliubov excitations with $E_{\mathbf{p}} \sim J$ can be generated because the energy deviation per particle is comparable to J as seen in Fig. 5.4. In addition, one can see that the computed propagation velocity has a large estimation error of the linear fitting. Such a large error is actually due to the presence of some exceptional points in, e.g., $C_d(t)$ at $d_E = 3$ and $\lambda_f = 4$ (see Fig. 5.6) that the maximum peak happens after the growth of the minimum one. We note that similar points also appear at $\lambda_f = 5$.

We conclude this part with comments on a previous study by Carleo and his coworkers [23]. They investigated similar quench dynamics of the density-density correlation function in the 2D Bose–Hubbard model by using a time-dependent variational Monte-Carlo approach. The numerical time evolution happens in a weakly-interacting regime starting from a unit-filling superfluid ground state, which was prepared within a variational wave function ansatz [23]. Figure 2(b) of Ref. [23] implies an unphysical result that the propagation velocity is much greater than twice the maximum one of the elementary excitation in the regime. While it seems to

contradict the Lieb–Robinson bound, the crucial reason of such a fast propagation has not been mentioned in their paper. To characterize the wavefront motion of the correlation on the square lattice, in Ref. [23], the propagation velocity was defined with units of the Manhattan distance $d_{\mathrm{M}} \equiv |d_x| + |d_y|$ [23, 24], which is a characteristic distance scale in a higher-dimensional lattice than one dimension. It is worth emphasizing that if we redefine $\bar{v}_{\mathrm{p}}$ by using the Manhattan distance instead of the Euclidean one in our TWA results, it leads to a similar fast propagation as in Ref. [23]. Hence, we argue that the fast propagation beyond twice the maximum velocity seen in Ref. [23] is actually due to the unsuitable choice of the propagation distance in the 2D geometry.

5.4.2 *Quench from a Mott Insulator State*

Thus far we have focused on the quench dynamics with the coherent state initial condition. Below we study a sudden quench from a Mott-insulator state with $\bar{n} = 10$ across the ground state phase transition point and keep track of the resulting dynamics of the density-density correlation function. As well as the previous case, we assume that the dynamics evolves inside a weakly interacting regime after the quench. We note that the initial quantum state corresponds to the ground state of the system at $\lambda = \infty$.

Figure 5.8 shows the semiclassical dynamics of the density-density correlation after the quench from the Mott-insulator state at $\lambda_{\mathrm{f}} = 2$. To do the Monte-Carlo sampling efficiently, we have utilized the approximate Gaussian Wigner function (5.14) instead of using the exact one. In contrast to the coherent state case, it is observed that a wave packet propagates over the 2D lattice as a single-peak signal with no fine oscillation. For such a wave packet, one can define its velocity by extracting the activation time of the minimum peak from the correlation function. In Fig. 5.9, we display the peak times obtained from the correlation signals at $\lambda_{\mathrm{f}} = 2$ and $\lambda_{\mathrm{f}} = 4$, respectively. Figure 5.10 shows the propagation velocity $\bar{v}_{\mathrm{p}}$ extracted from Fig. 5.9 as a function of λ_{f}. There, we also compare this velocity with the one for the coherent state. This result reveals that $\bar{v}_{\mathrm{p}}$ is approximately independent of λ_{f} in contrast to the coherent-state case, where the corresponding velocity clearly depends on λ_{f}.

The physical reason why two cases exhibit such a qualitative difference can be explained as follows: As seen in Fig. 5.11, the Mott insulator initial state corresponds to much larger excitation energy density than that of the coherent state. This means that the Bogoliubov excitations, which are elementary excitations of the system in the presence of condensates, are no longer relevant to such high-energy dynamics. The sudden quench considered here creates many single-particle excitations with various momenta relative to the initial density configuration in the insulator state. Therefore, the absence of the fine oscillation can be regarded as reflecting an incoherent motion joined by many single-particle excitations. This kind of single-particle picture is also helpful in explaining the nearly constant velocity of the correlation spreading. As we

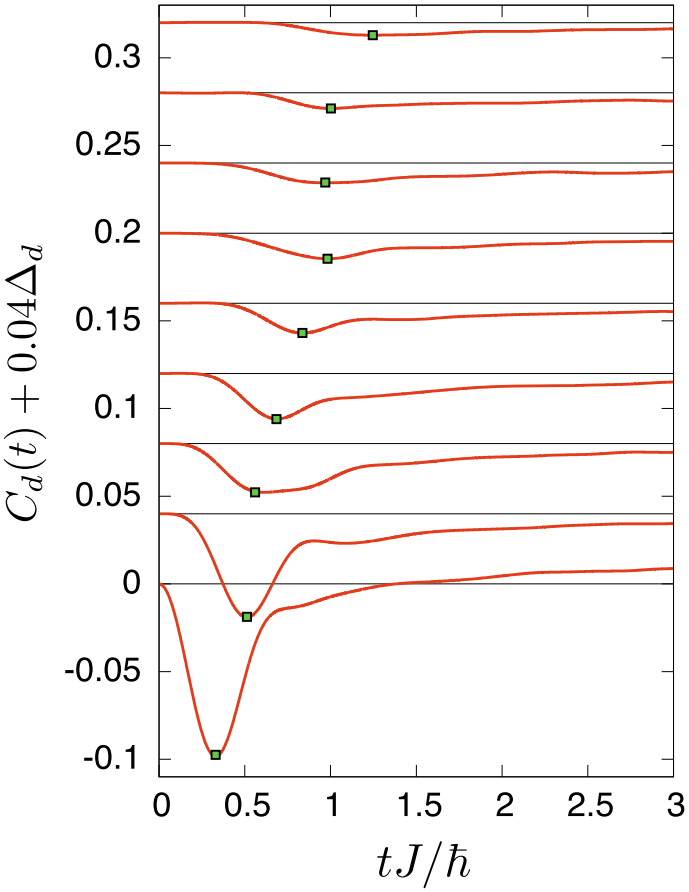

Fig. 5.8 TWA simulation of the density-density correlation function after the quench from the Mott-insulator state at $\lambda_\mathrm{f} = 2$. The green square indicates the minimum peak of the correlation signal. The relative vector $d = (d_x, d_y)$, Euclidean distance d_E, and offset of correlation Δ_d take values of $(d_x, d_y; d_\mathrm{E}; \Delta_d) = (0, 1; 1.00; 0)$, $(1, 1; 1.41; 1)$, $(0, 2; 2.00; 2)$, $(1, 2; 2.24; 3)$, $(2, 2; 2.83; 4)$, $(0, 3; 3.00; 5)$, $(1, 3; 3.16; 6)$, $(2, 3; 3.617)$, $(0, 4; 4.00; 8)$ from the bottom to top, respectively. In this simulation, we sampled $n_\mathrm{mc} = 10\,000$ initial conditions according to Eq. (5.14). (This figure is reproduced from Ref. [17].)

will see below, the Hartree–Fock approximation (HFA) for the lattice bosons leads to a constant group velocity of the elementary excitation because the interaction effect is incorporated as a constant shift to the non-interacting energy band [25].

In order to verify the property of the spreading velocity in practice, we apply the HFA to the Bose–Hubbard model. Let us consider one- and two-particle Green's functions for the lattice boson,

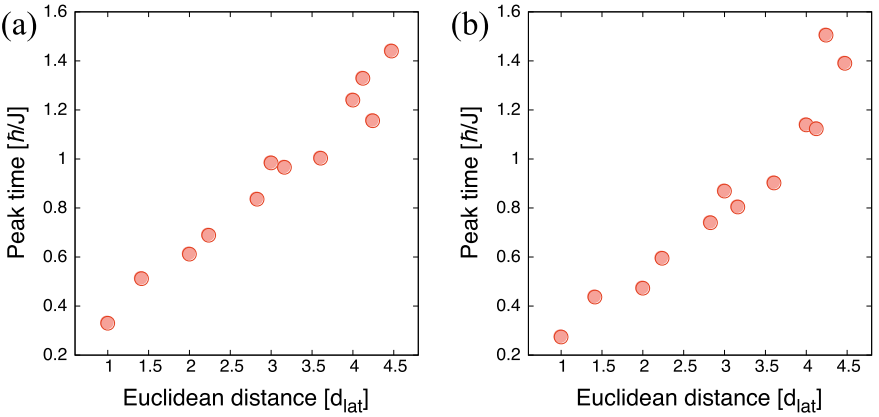

Fig. 5.9 Extracted peak times from the correlation signals at (a) $\lambda_f = 2$ and (b) $\lambda_f = 4$ quenched from the insulator state. The vertical and horizontal axes indicate the peak time and Euclidean distance, respectively. (This figure is reproduced from Ref. [17]. Copyright © 2019 American Physical Society. All rights reserved.)

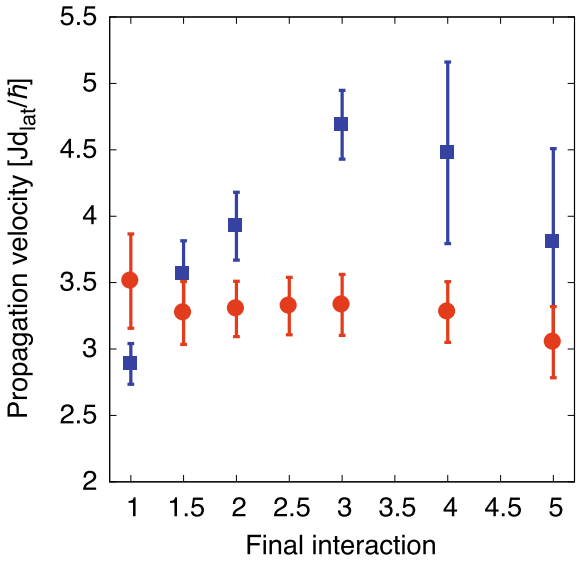

Fig. 5.10 λ_f dependence of the mean propagation velocity $\bar{v}_p$ (red circle). The blue square represents the result of the case of the coherent state shown in Fig. 5.6. The vertical bar indicates the normal estimation error of the linear fitting of the peak times. (This figure is reproduced from Ref. [17]. Copyright © 2019 American Physical Society. All rights reserved.)

$$G_{j,j'}(t,t') = \frac{1}{i}\left\langle T\left\{\hat{a}_j(t)\hat{a}^\dagger_{j'}(t')\right\}\right\rangle,$$

$$G^{(2)}_{j_1,j_2,j'_1,j'_2}(t_1,t_2,t'_1,t'_2) = \frac{1}{i^2}\left\langle T\left\{\hat{a}_{j_1}(t_1)\hat{a}_{j_2}(t_2)\hat{a}^\dagger_{j'_2}(t'_2)\hat{a}^\dagger_{j'_1}(t'_1)\right\}\right\rangle,$$

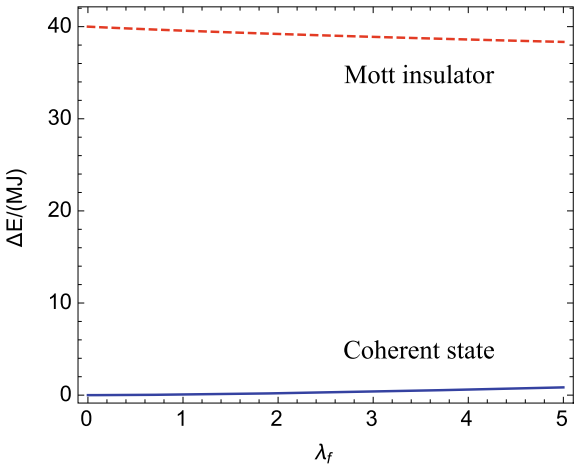

Fig. 5.11 Excitation energy density $\Delta E/(MJ)$ for the insulator initial state, measured from the ground state of the post-quench Hamiltonian (red-dashed line). The blue-solid line (same as the one in Fig. 5.4) represents the energy deviation when the initial state is prepared in the coherent state. This comparison indicates that the insulator state corresponds to a high-energy state relative to the ground state of the quenched system (This figure is reproduced from Ref. [17]. Copyright © 2019 American Physical Society. All rights reserved.)

where $T\{\cdots\}$ indicates a chronological-time ordering for operator products inside the bracket. In what follows, we deal with the 1D case for simplicity. From the Heisenberg equation for $\hat{a}_j(t)$, $G_{j,j'}(t,t')$ obeys the following equation of motion:

$$i\hbar\frac{\partial}{\partial t}G_{j,j'}(t,t') + JG_{j+1,j'}(t,t') + JG_{j-1,j'}(t,t') - iU\ G^{(2)}_{j,j,j',j}(t,t_1,t',t_1+\delta)\Big|_{t_1=t} = \hbar\delta(t-t')\delta_{j,j'}, \tag{5.23}$$

where δ is a positive and infinitesimal shift. In the HFA treatment, $G^{(2)}_{j,j,j',j}(t,t_1,t',t_1+\delta)$ is factorized into two parts as follows [26]:

$$G^{(2)}_{j,j,j',j}(t,t_1,t',t_1+\delta) = G_{j,j'}(t,t')G_{j,j}(t_1,t_1+\delta) + G_{j,j}(t,t_1+\delta)G_{j,j'}(t_1,t'). \tag{5.24}$$

This simplification can be regarded as a mean-field approximation, where any correlations between two indistinguishable bosons are neglected [26]. At $t_1 = t$, we find that

$$G_{j,j}(t,t_1+\delta) = G_{j,j}(t_1,t_1+\delta) = -i\langle\hat{n}_j(t)\rangle = -i\bar{n}. \tag{5.25}$$

Thus, Eq. (5.23) results in a closed equation with respect to $G_{j,j'}(t,t')$:

$$\left\{ i\hbar\frac{\partial}{\partial t} - 2U\bar{n} \right\} G_{j,j'}(t,t') + JG_{j+1,j'}(t,t') + JG_{j-1,j'}(t,t') = \hbar\delta(t-t')\delta_{j,j'}. \tag{5.26}$$

Equation (5.26) means a constant shift of the pole of the one-particle Green function as

$$\epsilon_{\text{free}}(p) \to \epsilon_{\text{free}}(p) + 2U\bar{n}, \tag{5.27}$$

where $\epsilon_{\text{free}}(p) = -2J\cos(pd_{\text{lat}}/\hbar)$ is the single-particle dispersion at the non-interacting case $U = 0$. This result says that the interaction does not change the group velocity of the single-particle excitation within the HFA. Notice that this result is also valid for the 2D case because the dimensionality enters only into the free dispersion.

5.5 Summary of This Chapter

In conclusion of this chapter, we studied far-from-equilibrium dynamics of the 2D and 3D Bose–Hubbard models after a sudden quantum quench to a weakly interacting regime. We applied the semiclassical TWA method to analyze the experimentally-measured redistribution dynamics of the 3D system after a quench from the singly-occupied Mott insulator state. It was demonstrated that our semiclassical simulation agrees very well with the experimental result without any free parameter.

We also studied the density-density correlation spreading in the square lattice after a sudden quench at a large filling factor. We numerically demonstrated that when the system is initially prepared in the coherent product state, the mean propagation velocity of the wave packet in the correlation function clearly depends on the final interaction strength of the quench. Physically, this dependence can be understood as reflecting the properties of the low-energy elementary excitation in the weakly interacting regime. In contrast, it was found that when the initial state is the Mott insulator state, the mean propagation velocity is almost independent of the final interaction because of the property of the high-energy single-particle excitations, which are effectively described by the HFA for lattice bosons.

References

1. M. Lewenstein, A. Sanpera, V. Ahufinger, *Ultracold Atoms in Optical Lattices: Simulating Quantum Many-Body Systems* (Oxford University Press, Oxford, 2012)
2. A. Polkovnikov, Ann. Phys. **325**, 1790 (2010)
3. A. Polkovnikov, S. Sachdev, S.M. Girvin, Phys. Rev. A **66**, 053607 (2002)
4. A. Polkovnikov, Phys. Rev. A **68**, 033609 (2003)

5. Y. Takasu, T. Yagami, H. Asaka, Y. Fukushima, K. Nagao, S. Goto, I. Danshita, and Y. Takahashi, arXiv:2002.12025 [cond-mat.quant-gas]
6. T.D. Kühner, S.R. White, H. Monien, Phys. Rev. B **61**, 12474 (2000)
7. B. Capogrosso-Sansone, N.V. Prokof'ev, B.V. Svistunov, Phys. Rev. B **75**, 134302 (2007)
8. C.W. Gardiner, J.R. Anglin, T.I.A. Fudge, J. Phys. B: At. Mol. Opt. Phys. **35**, 1555 (2002)
9. M.K. Olsen, A.S. Bradley, S.B. Cavalcanti, Phys. Rev. A **70**, 033611 (2004)
10. P.B. Blakie, A.S. Bradley, M.J. Davis, R.J. Ballagh, C.W. Gardiner, Adv. Phys. **57**, 363 (2008)
11. S.M. Davidson, D. Sels, A. Polkovnikov, Ann. Phys. **384**, 128 (2017)
12. J. Wurtz, A. Polkovnikov, D. Sels, Ann. Phys. **395**, 341 (2018)
13. I.S. Landea, N. Nessi, Phys. Rev. A **91**, 063601 (2015)
14. S.M. Davidson, A. Polkovnikov, Phys. Rev. Lett. **114**, 045701 (2015)
15. W.K. Wootters, Ann. Phys. **176**, 1 (1987)
16. J. Schachenmayer, A. Pikovski, A.M. Rey, Phys. Rev. X **5**, 011022 (2015)
17. K. Nagao, M. Kunimi, Y. Takasu, Y. Takahashi, I. Danshita, Phys. Rev. A **99**, 023622 (2019)
18. M. Cheneau, P. Barmettler, D. Poletti, M. Endres, P. Schauß, T. Fukuhara, C. Gross, I. Bloch, C. Kollath, S. Kuhr, Nature **481**, 484 (2012)
19. E. Altman, E. Demler, M.D. Lukin, Phys. Rev. A **70**, 013603 (2004)
20. S. Fölling, F. Gerbier, A. Widera, O. Mandel, T. Gericke, I. Bloch, Nature **434**, 481 (2005)
21. I. Danshita, P. Naidon, Phys. Rev. A **79**, 043601 (2009)
22. E.H. Lieb, D.W. Robinson, Commun. Math. Phys. **28**, 251 (1972)
23. G. Carleo, F. Becca, L. Sanchez-Palencia, S. Sorella, M. Fabrizio, Phys. Rev. A **89**, 031602(R) (2014)
24. E.F. Krause, *Taxicab Geometry* (Courier Dover Publications, New York, 1986)
25. C.J. Pethick, H. Smith, *Bose-Einstein Condensation in Dilute Gases* (Cambridge University Press, Cambridge, UK, 2008)
26. L.P. Kadanoff, G. Baym, *Quantum Statistical Mechanics* (Benjamin, New York, 1962)

Chapter 6
Conclusions and Outlooks

Abstract In this chapter, we summarize the main results of this Thesis presented in Chaps. 4 and 5 and conclude this Thesis. We also show outlooks for future works.

In this Thesis, we have focused on near- and far-from-equilibrium dynamics of ultracold Bose atoms in optical lattices. We have worked especially on theoretical analyses of several non-equilibrium quantum many-body problems motivated by experimental works using approaches in which effects of fluctuations are taken into account beyond the naive mean-field treatments. Hence, this Thesis offers an important step towards deeper understanding of quantum many-body phenomena realized in real experiments of ultracold atoms.

In Chap. 4, we studied the Higgs mode of strongly-interacting superfluid Bose gases in the three-dimensional (3D) cubic optical lattice, especially, its stability and detectability in the experimental systems. To excite the Higgs mode in the optical lattice, we have discussed two experimentally feasible protocols, i.e., the kinetic energy and onsite interaction modulations and formulated the corresponding response functions using the linear-response theory. We used the effective-model representation of the strongly-interacting Bose–Hubbard model and calculated the response functions combining it with the finite-temperature Green's function theory. Our perturbative calculations provided quantum and thermal fluctuation corrections to the spectral properties of the Higgs mode. We showed that if the system is uniform, the Higgs mode is then sufficiently robust and can exist as a well-defined resonance peak even at typical temperatures of experiments. This should be contrasted with the two-dimensional case, in which the corresponding resonance becomes rather broad due to the fluctuations. Furthermore, we have analyzed the non-uniform trap effect on the uniform response functions at unit filling on the basis of the local-density approximation. We demonstrated that the resonance peak is significantly broadened due to the trapping potential when the modulations are applied globally to the entire system. In order to extract a sharp resonance peak from the smeared response, we discussed partial modulations around the trap center. The results with a modulation radius $R_{\mathrm{mod}} < 0.5 R_{\mathrm{TF}}$ showed that a well-defined resonance peak of the Higgs mode can survive at typical temperatures.

K. Nagao, *Fluctuations and Non-Equilibrium Phenomena in Strongly-Correlated Ultracold Atoms*, Springer Theses, https://doi.org/10.1007/978-981-15-7171-8_6

One of the promising directions associated with the stability of the Higgs mode is to analyze the same response functions for the 3D Bose–Hubbard model by performing quantum Monte-Carlo (QMC) simulations. Recently, a spectral function characterizing the response of the Higgs mode has been calculated using a QMC technique for a 3D quantum antiferromagnet [1], which has a quantum critical point described by the relativistic O(3) scalar model. The results of Ref. [1] have exhibited that there appears a sufficiently sharp resonance peak of the Higgs mode in the spectral function. It seems to be an intriguing problem that one applies the same numerical technique to the 3D Bose–Hubbard model with a non-uniform potential, and validates our qualitative results through comparing them with more quantitative ones obtained from QMC simulations. Furthermore, it is also interesting to employ the functional (or non-perturbative) renormalization group approach for computing the response functions for the 3D Bose–Hubbard model [2–5].

In Chap. 5, we have investigated far-from-equilibrium dynamics after a sudden quantum quench in Bose gases trapped by optical lattices. First, applying the truncated-Wigner approximation (TWA), we analyzed the redistribution dynamics of the kinetic and interaction energies of the 3D Bose–Hubbard model after a quantum quench from a singly-occupied Mott-insulator state. Through a direct comparison with the experimental data, it was reported that our semiclassical results capture the characteristic behavior of redistribution and remarkably agree with the data with no fitting parameter. Furthermore, we also studied the spreading of the density-density correlation over space in the two-dimensional (2D) Bose–Hubbard model at a large filling factor. We focused especially on the initial state dependence of the spreading dynamics. We numerically showed that when the system is initially prepared in the coherent state, then the propagation velocity of the correlation wave packet strongly depends on the final interaction strength. We discussed that this feature can be understood from the properties of the low-energy elementary excitation in the weakly-interacting regime. In contrast, we demonstrated that when the initial quantum state is the Mott insulator state, then the propagation velocity of correlations is almost independent of the final interaction. We also provided a physical interpretation to such a result in terms of the property of the high-energy single-particle excitations, whose spectrum was explicitly obtained from the Hartree–Fock approximation.

The experiment of the quantum optics group at Kyoto University has also studied correlation-spreading dynamics in a 2D strongly-interacting Bose-gas system [6]. However, our semiclassical scheme presented in this Thesis would not capture such dynamics accurately because the *quantum-to-classical correspondence* of dynamics by means of the Gross–Pitaevskii equation and coherent state phase space is no longer valid in the strongly-correlated parameter regime. Recently, a promising approach to strongly-interacting dynamics has been proposed by Davidson and Polkovnikov, and it has been referred to as the SU(3) truncated-Wigner approximation [7]. This technique, which is applicable to quantum spin-1 or three-level systems with local interactions, increases phase-space variables of the classical limit in order to linearize the local interaction in the phase-space variables. Applying the SU(3)TWA, we can

simulate the wave-packet motion observed in the measured correlation function more accurately [8]. A similar increased-phase-space technique can also be developed for more complicated cases of interacting fermions, and it successfully improves far-from-equilibrium dynamics in the strongly-correlated regime [9]. These results will be presented by publications sometime in the future (not included in this Thesis).

References

1. Y.Q. Qin, B. Normand, A.W. Sandvik, Z.Y. Meng, Phys. Rev. Lett. **118**, 147207 (2017)
2. A. Rançon, N. Dupuis, Phys. Rev. B **83**, 172501 (2011)
3. A. Rançon, N. Dupuis, Phys. Rev. B **84**, 174513 (2011)
4. A. Rançon, N. Dupuis, Phys. Rev. B **89**, 180501(R) (2014)
5. F. Rose, F. Léonard, N. Dupuis, Phys. Rev. B **91**, 224501 (2015)
6. Y. Takasu, T. Yagami, H. Asaka, Y. Fukushima, K. Nagao, S. Goto, I. Danshita, Y. Takahashi, arXiv:2002.12025 [cond-mat.quant-gas]
7. S.M. Davidson, A. Polkovnikov, Phys. Rev. Lett. **114**, 045701 (2015)
8. K. Nagao, Y. Takasu, Y. Takahashi, I. Danshita, unpublished
9. K. Nagao, A. Polkovnikov, unpublished

Appendix A
Energy Absorption Due to the Onsite-Interaction Strength Modulations

In this appendix, we derive the relation between the response function (4.4) and energy absorbed by the system for a finite-time period of the onsite-interaction strength modulation. The similar discussion has been performed for the case of hopping modulations. For more details, see, e.g., Endres's doctoral thesis cited in Chap. 4

As seen in Sect. 4.1.2, the time-dependent perturbed Hamiltonian $\mathcal{H}_{\rm BH}(t) = \mathcal{H}_{\rm BH} + \Delta_U(t)O$ describes the system that is initially in a thermal equilibrium state and is driven by the small and periodic modulation $U \to [1 + \Delta_U(t)]U = [1 + \delta_U \cos(\omega t)]U$ at a fixed ω. If we assume that $\rho(t)$ is the total density operator at t, which approaches the equilibrium one $\rho_{\rm eq}$ as $t \to -\infty$, then the total energy of the system at t is given by $E(t) = \langle \mathcal{H}_{\rm BH}(t)\rangle(t) = {\rm Tr}[\rho(t)\mathcal{H}_{\rm BH}(t)]$. We can verify easily that its instantaneous change rate $dE(t)/dt$ is proportional to only the instantaneous average of O with an oscillation factor:

$$\begin{aligned}\frac{dE}{dt} &= \dot{\Delta}_U(t)\langle O\rangle(t) \\ &= -\omega\delta_U \sin(\omega t)\langle O\rangle(t). \end{aligned} \tag{A.1}$$

Following the linear response theory, the response of O to the U modulation, which is defined by $\Delta\langle O\rangle(t) \equiv \langle O\rangle(t) - \langle O\rangle_{\rm eq}$, is related to $\Delta_U(t)$ such that

$$\Delta\langle O\rangle(t) = \int_{-\infty}^{t} D^{\rm R}_{OO}(t - t')\Delta_U(t'), \tag{A.2}$$

where $D^{\rm R}_{OO}(t - t')$ is the response function given by Eq. (4.4). Substituting $\Delta_U(t) = \delta_U \cos(\omega t)$ into this Eq. (A.2), we have

$$\begin{aligned}\Delta\langle O\rangle(t) &= \delta_U {\rm Re}\left\{e^{{\rm i}\omega t}\chi^{*}_{OO}(\omega)\right\} \\ &= \delta_U \left\{\cos(\omega t){\rm Re}\chi_{OO}(\omega) + \sin(\omega t){\rm Im}\chi_{OO}(\omega)\right\}. \end{aligned} \tag{A.3}$$

K. Nagao, *Fluctuations and Non-Equilibrium Phenomena in Strongly-Correlated Ultracold Atoms*, Springer Theses, https://doi.org/10.1007/978-981-15-7171-8

Averaging Eq. (A.1) over one period $t_{\mathrm{mod}} = 2\pi/\omega$ and using Eq. (A.3), we finally obtain the mean energy absorbed by the system for a period of t_{mod}

$$\Delta E(\omega) = \frac{1}{t_{\mathrm{mod}}} \int_0^{t_{\mathrm{mod}}} dt \frac{dE}{dt} = \frac{(\delta_O)^2}{2} \omega S_{OO}(\omega), \tag{A.4}$$

where $S_{OO}(\omega) = -\mathrm{Im}\chi_{OO}(\omega)$ is the spectral function. One can measure $\Delta E(\omega)$ accurately by using the quantum-gas microscope technique. The relation (A.4) reveals that for the modulations of U, the experimental observable $\Delta E(\omega)$ is characterized only by the O-to-O response function $D^{\mathrm{R}}_{OO}(t - t')$.

Appendix B
Coefficients in the Effective Model

Here we present the coefficients characterizing each part of the spin-wave Hamiltonian, i.e., $\mathcal{H}_{\rm eff}^{(l)}$ for $l = 0, 1, 2, 3, 4$. To simplify our discussion, let us define a bi-linear representation of the pseudospin operators as follows:

$$\begin{aligned} S_i^+ = t_i^\dagger T_1 t_i, \quad S_i^- = t_i^\dagger T_2 t_i, \quad S_i^z = t_i^\dagger T_3 t_i, \\ (S_i^z)^2 = t_i^\dagger T_4 t_i, \quad S_i^z S_i^+ = t_i^\dagger T_5 t_i, \quad S_i^- S_i^z = t_i^\dagger T_6 t_i, \end{aligned} \tag{B.1}$$

where $t_i = (t_{1,i}, t_{0,i}, t_{-1,i})^{\rm T}$. We have introduced matrices $T_1, T_2, \ldots, T_6$ defined by

$$\begin{aligned} T_1 &= \begin{pmatrix} 0 & \sqrt{2} & 0 \\ 0 & 0 & \sqrt{2} \\ 0 & 0 & 0 \end{pmatrix}, \quad T_2 = \begin{pmatrix} 0 & 0 & 0 \\ \sqrt{2} & 0 & 0 \\ 0 & \sqrt{2} & 0 \end{pmatrix}, \quad T_3 = \begin{pmatrix} 1 & 0 & 0 \\ 0 & 0 & 0 \\ 0 & 0 & -1 \end{pmatrix}, \\ T_4 &= \begin{pmatrix} 1 & 0 & 0 \\ 0 & 0 & 0 \\ 0 & 0 & 1 \end{pmatrix}, \quad T_5 = \begin{pmatrix} 0 & \sqrt{2} & 0 \\ 0 & 0 & 0 \\ 0 & 0 & 0 \end{pmatrix}, \quad T_6 = \begin{pmatrix} 0 & 0 & 0 \\ \sqrt{2} & 0 & 0 \\ 0 & 0 & 0 \end{pmatrix}. \end{aligned} \tag{B.2}$$

This representation is related to the fact that arbitrary local operators acting on a locally three-level Hilbert space can be expressed as a linear combination of 3×3 basic matrices of the SU(3) Lie algebra, such as the Gell-Mann matrices.

The canonical transformation (2.55) can be regarded as the linear transformation from the old basis t_i to the new one $b_i = (b_{1,i}, b_{0,i}, b_{2,i})^{\rm T}$. After the transformation, the elements of the matrices in the new basis are given by

$$\tilde{T}_1 = \begin{pmatrix} -\sqrt{2}s_1c_1(s_2+c_2) & \sqrt{2}({s_1}^2c_2 - {c_1}^2s_2) & -\sqrt{2}s_1s_2 \\ \sqrt{2}({s_1}^2s_2 - {c_1}^2c_2) & \sqrt{2}s_1c_1(s_2+c_2) & -\sqrt{2}c_1s_2 \\ \sqrt{2}s_1c_2 & \sqrt{2}c_1c_2 & 0 \end{pmatrix}, \tag{B.3}$$

K. Nagao, *Fluctuations and Non-Equilibrium Phenomena in Strongly-Correlated Ultracold Atoms*, Springer Theses, https://doi.org/10.1007/978-981-15-7171-8

$$\tilde{T}_2 = \begin{pmatrix} -\sqrt{2}s_1c_1(s_2+c_2) & \sqrt{2}({s_1}^2s_2 - {c_1}^2c_2) & \sqrt{2}s_1c_2 \\ \sqrt{2}({s_1}^2c_2 - {c_1}^2s_2) & \sqrt{2}s_1c_1(s_2+c_2) & \sqrt{2}c_1c_2 \\ -\sqrt{2}s_1s_2 & -\sqrt{2}c_1s_2 & 0 \end{pmatrix}, \tag{B.4}$$

$$\tilde{T}_3 = \begin{pmatrix} {c_1}^2({s_2}^2 - {c_2}^2) & s_1c_1({c_2}^2 - {s_2}^2) & -2c_1s_2c_2 \\ s_1c_1({c_2}^2 - {s_2}^2) & {s_1}^2({s_2}^2 - {c_2}^2) & 2s_1s_2c_2 \\ -2c_1s_2c_2 & 2s_1s_2c_2 & {c_2}^2 - {s_2}^2 \end{pmatrix}, \tag{B.5}$$

$$\tilde{T}_4 = \begin{pmatrix} {c_1}^2 & -s_1c_1 & 0 \\ -s_1c_1 & {s_1}^2 & 0 \\ 0 & 0 & 1 \end{pmatrix}, \tag{B.6}$$

$$\tilde{T}_5 = \begin{pmatrix} -\sqrt{2}s_1c_1s_2 & -\sqrt{2}{c_1}^2s_2 & 0 \\ \sqrt{2}{s_1}^2s_2 & \sqrt{2}s_1c_1s_2 & 0 \\ \sqrt{2}s_1c_2 & \sqrt{2}c_1c_2 & 0 \end{pmatrix}, \tag{B.7}$$

$$\tilde{T}_6 = \begin{pmatrix} -\sqrt{2}s_1c_1s_2 & \sqrt{2}{s_1}^2s_2 & \sqrt{2}s_1c_2 \\ -\sqrt{2}{c_1}^2s_2 & \sqrt{2}s_1c_1s_2 & \sqrt{2}c_1c_2 \\ 0 & 0 & 0 \end{pmatrix}. \tag{B.8}$$

In the following equations, we express the matrix elements of each matrix by

$$\tilde{T}_\mu = \begin{pmatrix} (\tilde{T}_\mu)_{11} & (\tilde{T}_\mu)_{10} & (\tilde{T}_\mu)_{12} \\ (\tilde{T}_\mu)_{01} & (\tilde{T}_\mu)_{00} & (\tilde{T}_\mu)_{02} \\ (\tilde{T}_\mu)_{21} & (\tilde{T}_\mu)_{20} & (\tilde{T}_\mu)_{22} \end{pmatrix}. \tag{B.9}$$

Here the index μ runs from $\mu = 1$ to $\mu = 6$.

In terms of the matrix elements, the coefficients in $\mathcal{H}_{\text{eff}}^{(0)}$ are given by

$$A_0 = -\frac{Jn_0z}{2}\{(\tilde{T}_1)_{00} + \delta\nu(\tilde{T}_5)_{00}\}^2, \tag{B.10}$$

$$\tilde{A}_0 = \frac{U}{2}(\tilde{T}_4)_{00} - B(\tilde{T}_3)_{00}. \tag{B.11}$$

The coefficients in $\mathcal{H}_{\text{eff}}^{(1)}$ are given by

$$A_1 = -\frac{Jn_0z}{2}\{(\tilde{T}_1)_{00} + \delta\nu(\tilde{T}_5)_{00}\}\Big[(\tilde{T}_1)_{01} + (\tilde{T}_1)_{10} + \delta\nu(\tilde{T}_5)_{01} + \delta\nu(\tilde{T}_5)_{10}\Big], \tag{B.12}$$

$$B_1 = -\frac{Jn_0z}{2}\{(\tilde{T}_1)_{00} + \delta\nu(\tilde{T}_5)_{00}\}\Big[(\tilde{T}_1)_{02} + (\tilde{T}_1)_{20} + \delta\nu(\tilde{T}_5)_{20}\Big], \tag{B.13}$$

$$\tilde{A}_1 = \frac{U}{2}(\tilde{T}_4)_{10} - B(\tilde{T}_3)_{10}, \tag{B.14}$$

$$\tilde{B}_1 = -B(\tilde{T}_3)_{20}. \tag{B.15}$$

The coefficients in $\mathcal{H}_{\text{eff}}^{(2)}$ are given by

$$A_2 = -Jn_0z\{(\tilde{T}_1)_{00} + \delta\nu(\tilde{T}_5)_{00}\}\{(\tilde{T}_1)_{11} + \delta\nu(\tilde{T}_5)_{11}\}, \tag{B.16}$$

$$B_2 = -\frac{Jn_0z}{2}\Big[\{(\tilde{T}_1)_{00} + \delta\nu(\tilde{T}_5)_{00}\}\{(\tilde{T}_1)_{21} + \delta\nu(\tilde{T}_5)_{21}\} + (\tilde{T}_1)_{12}\{(\tilde{T}_1)_{00} + \delta\nu(\tilde{T}_5)_{00}\}\Big], \tag{B.17}$$

$$D_2 = -\frac{Jn_0z}{2}\{(\tilde{T}_1)_{10} + \delta\nu(\tilde{T}_5)_{10}\}\{(\tilde{T}_1)_{01} + \delta\nu(\tilde{T}_5)_{01}\}, \tag{B.18}$$

$$E_2 = -\frac{Jn_0z}{2}\Big[\{(\tilde{T}_1)_{10} + \delta\nu(\tilde{T}_5)_{10}\}^2 + \{(\tilde{T}_1)_{01} + \delta\nu(\tilde{T}_5)_{01}\}^2\Big], \tag{B.19}$$

$$F_2 = -\frac{Jn_0z}{2}\Big[\{(\tilde{T}_1)_{20} + \delta\nu(\tilde{T}_5)_{20}\}\{(\tilde{T}_1)_{10} + \delta\nu(\tilde{T}_5)_{10}\} + (\tilde{T}_1)_{02}\{(\tilde{T}_1)_{01} + \delta\nu(\tilde{T}_5)_{01}\}\Big], \tag{B.20}$$

$$G_2 = -\frac{Jn_0z}{2}\Big[\{(\tilde{T}_1)_{20} + \delta\nu(\tilde{T}_5)_{20}\}\{(\tilde{T}_1)_{01} + \delta\nu(\tilde{T}_5)_{01}\} + (\tilde{T}_1)_{02}\{(\tilde{T}_1)_{10} + \delta\nu(\tilde{T}_5)_{10}\}\Big], \tag{B.21}$$

$$H_2 = -\frac{Jn_0z}{2}(\tilde{T}_1)_{02}\{(\tilde{T}_1)_{20} + \delta\nu(\tilde{T}_5)_{20}\}, \tag{B.22}$$

$$I_2 = -\frac{Jn_0z}{2}\Big[\{(\tilde{T}_1)_{20} + \delta\nu(\tilde{T}_5)_{20}\}^2 + (\tilde{T}_1)_{02}^2\Big], \tag{B.23}$$

$$\tilde{A}_2 = \frac{U}{2}(\tilde{T}_4)_{11} - B(\tilde{T}_3)_{11}, \tag{B.24}$$

$$\tilde{B}_2 = -B(\tilde{T}_3)_{12}, \tag{B.25}$$

$$\tilde{C}_2 = \frac{U}{2}(\tilde{T}_4)_{22} - B(\tilde{T}_3)_{22}. \tag{B.26}$$

The coefficients in $\mathcal{H}_{\text{eff}}^{(3)}$ are given by

$$A_3 = -\frac{Jn_0z}{2}\{(\tilde{T}_1)_{11} + \delta\nu(\tilde{T}_5)_{11}\}\{(\tilde{T}_1)_{10} + (\tilde{T}_1)_{01} + \delta\nu(\tilde{T}_5)_{10} + \delta\nu(\tilde{T}_5)_{01}\}, \tag{B.27}$$

$$B_3 = -\frac{Jn_0z}{2}\{(\tilde{T}_1)_{11} + \delta\nu(\tilde{T}_5)_{11}\}\{(\tilde{T}_1)_{20} + (\tilde{T}_1)_{02} + \delta\nu(\tilde{T}_5)_{20}\}, \tag{B.28}$$

$$C_3 = -\frac{Jn_0z}{2}\Big[\{(\tilde{T}_1)_{10} + \delta\nu(\tilde{T}_5)_{10})(\tilde{T}_1)_{12} + \{(\tilde{T}_1)_{21} + \delta\nu(\tilde{T}_5)_{21}\}\{(\tilde{T}_1)_{01} + \delta\nu(\tilde{T}_5)_{01}\}\Big], \tag{B.29}$$

$$D_3 = -\frac{Jn_0z}{2}\Big[\{(\tilde{T}_1)_{10} + \delta\nu(\tilde{T}_5)_{10}\}\{(\tilde{T}_1)_{21} + \delta\nu(\tilde{T}_5)_{21}\} + \{\tilde{T}_1)_{12}((\tilde{T}_1)_{01} + \delta\nu(\tilde{T}_5)_{01}\}\Big], \tag{B.30}$$

$$E_3 = -\frac{Jn_0z}{2}\Big[\{(\tilde{T}_1)_{21} + \delta\nu(\tilde{T}_5)_{21}\}\{(\tilde{T}_1)_{20} + \delta\nu(\tilde{T}_5)_{20}\} + (\tilde{T}_1)_{02}(\tilde{T}_1)_{12}\Big], \quad \text{(B.31)}$$

$$F_3 = -\frac{Jn_0z}{2}\Big[(\tilde{T}_1)_{02}\{(\tilde{T}_1)_{21} + \delta\nu(\tilde{T}_5)_{21}\} + (\tilde{T}_1)_{12}\{(\tilde{T}_1)_{20} + \delta\nu(\tilde{T}_5)_{20}\}\Big], \quad \text{(B.32)}$$

Finally, the coefficients in $\mathcal{H}_{\text{eff}}^{(4)}$ are given by

$$A_4 = -\frac{Jn_0z}{2}\{(\tilde{T}_1)_{11} + \delta\nu(\tilde{T}_5)_{11}\}^2, \quad \text{(B.33)}$$

$$B_4 = -\frac{Jn_0z}{2}(\tilde{T}_1)_{12}\{(\tilde{T}_1)_{21} + \delta\nu(\tilde{T}_5)_{21}\}, \quad \text{(B.34)}$$

$$C_4 = -\frac{Jn_0z}{2}\{(\tilde{T}_1)_{11} + \delta\nu(\tilde{T}_5)_{11}\}\Big[(\tilde{T}_1)_{12} + (\tilde{T}_1)_{21} + \delta\nu(\tilde{T}_5)_{21}\Big], \quad \text{(B.35)}$$

$$D_4 = -\frac{Jn_0z}{2}\Big[\{(\tilde{T}_1)_{21} + \delta\nu(\tilde{T}_5)_{21}\}^2 + (\tilde{T}_1)_{12}^2\Big]. \quad \text{(B.36)}$$